Modelling of nano nMOSFETs with alternative channel materials in the fully and quasi ballistic regimes

Quentin Rafhay

▶ To cite this version:

Quentin Rafhay. Modelling of nano nMOSFETs with alternative channel materials in the fully and quasi ballistic regimes. Micro et nanotechnologies/Microélectronique. Institut National Polytechnique de Grenoble - INPG, 2008. Français. NNT : . tel-00398674

HAL Id: tel-00398674
https://theses.hal.science/tel-00398674

Submitted on 24 Jun 2009

HAL is a multi-disciplinary open access archive for the deposit and dissemination of scientific research documents, whether they are published or not. The documents may come from teaching and research institutions in France or abroad, or from public or private research centers.

L'archive ouverte pluridisciplinaire **HAL**, est destinée au dépôt et à la diffusion de documents scientifiques de niveau recherche, publiés ou non, émanant des établissements d'enseignement et de recherche français ou étrangers, des laboratoires publics ou privés.

INSTITUT POLYTECHNIQUE DE GRENOBLE

N° attribué par la bibliothèque
|__|__|__|__|__|__|__|__|__|__|

THESE EN COTUTELLE INTERNATIONALE

pour obtenir le grade de

DOCTEUR DE L'Institut polytechnique de Grenoble
et
de l'Università degli Studi di Udine

Spécialité : *Micro et Nano Electronique*

préparée à l'Institut de Microélectronique, Electromagnétisme et Photonique – Laboratoire d'Hyperfréquence et de Caractérisation

dans le cadre de **l'Ecole Doctorale Electronique, Electrotechnique Automatique Télécommunications et signal (EEATS)**

et au laboratoire Dipartimento di Ingegneria Elettrica, Gestionale e Meccanica

présentée et soutenue publiquement

par

Quentin Rafhay

le 7 novembre 2008

Modelling of nano nMOSFETs with alternative channel materials in the fully and quasi ballistic regimes

Directeurs de these
Gérard Ghibaudo
Luca Selmi

JURY

M. Jean Pierre COLINGE , Président
M. Jean Luc AUTRAN , Rapporteur
M. Philippe DOLLFUS , Rapporteur
M. Gérard GHIBAUDO , Directeur de thèse
M. Luca SELMI , Directeur de thèse
M. Raphaël CLERC , Co-encadrant
M. Pierpaolo PALESTRI , Co-encadrant
M. Frédéric BŒUF , invité
Mme Maud VINET , invité

« En revanche, quand les progrès de la science universelle ont suffisamment préparé les esprits à la recevoir, la théorie naît d'une manière presque forcée et, bien souvent, des physiciens qui ne se connaissent pas, qui poursuivent leurs médiations bien loin les unes des autres, l'enfantent presque en même temps: on dirait que l'idée flotte dans l'air, portée d'un pays à l'autre par le vent qui souffle, prête à féconder tout génie qui se trouve en état de l'accueillir et de la développer, semblable au pollen qui engendre un fruit partout où il rencontre un calice mûr. »

Pierre Duhem, *La Théorie Physique*

Acknowledgements

I would like to thank, at first, Francis Ballestra, former director of IMEP, now IMEP-LAHC, for having welcoming me in the lab. I also would like to thank him for his great work in the different European Network of excellence (Sinano, and now Nanosil), which often helped me in the organisation and travels of my PhD.

I would like to send my acknowledgment to the members of my jury, to thank them for their work and presence at my defence, which has been a highly memorable moment of my life. My regards go to Jean Luc Autran and Philippe Dollfus for having reviewed my thesis and for having giving me a relevant feedback on my work. I would like to thank Jean Pierre Colinge for being the president of my jury, which was organized with his respected professionalism and famous sense of humour. Frederic Boeuf and Maud Vinet have also played a significant role during my defence, but their have also played a significant role during my PhD, by giving me the opportunity to regularly present the results of my studies respectively at ST Microelectronics and at the CEA-LETI. Those kinds of constant cooperation between the different labs and groups in the Grenoble's microelectronic activity has always been, to me, the best way to improve my work, by confronting our different point of view on my topic.

Obviously, this work would not have been possible without the constant help and support of my (numerous but all fantastic) boss, both on the French and Italian side.

I would like to thank at first Gérard Ghibaudo, who has always been there to help me, both for theoretical issues and for the organization of my PhD. I wish will keep the same enthusiasm for science as him for the next upcoming decades and that one day, maybe, after years of hard work, I might be such a good expert of my field as Gérard is. I would also like to thank him for his genuine and so respectful management of the lab, which have been a place where I have loved to work.

Having such a great boss has been a chance. Having two like this has been a dream. The second great boss I had during my PhD has been Luca Selmi, and I would like to thank him at first for giving me the opportunity to work in his group. His group is an impressive industry of science and knowledge. Being part of this has been a fantastic experience to me.

Gérard Ghibaudo and Luca Selmi are true professional models to me, both as scientists and as managers.

Not only I had great "big boss", but I also directly worked in close contact with two impressive scientists : Raphaël Clerc and Pierpaolo Palestri.

I think the word "thank" might be a little bit too weak to really thank Raphaël. Without him, since many years right now, even before this PhD, nothing would have been possible. I would like to thank him for constantly trusting in me. Raphaël knows better than anybody, and better than me, what I am able to do, and he has always pushed me to give my best. He succeeded in this. The quality of the work carried out during these three years is a consequence of his constant willingness of excellence in science, and in life. He is in addition

a great teacher. And he taught me more than knowledge. With Raphaël, I learnt a method : the scientific method. I will do my best to apply it has well as he applies it.

I had the chance to have two great "big boss" and I had the chance to have two great "teachers". My Italian teacher is Pierpaolo Palestri and I would like to thank him for the work, energy and time he spent with me during my stays in Udine. Although I surely I did not get all the explanation he gave me about carrier transport and the Monte Carlo method, I did learn much with him, and my stay in Udine clearly helped me to understand my subject and my field. I have also learnt much about Rock and Roll and Italian idioms with him.

I have been working with great boss, but I have also been working in great labs. I would like to thank many people of these two labs for their help and support. In IMEP-LAHC, my regards go to George Pananakakis who is still working to possibly transfer my work in MaSTar and to Marc Bescond, who stayed with us for two years and initiate with Marco Pala the device simulation activity of the lab. I also would like to thank the researcher of the CMNE group : Jalal Jomaah, Edwige Bano, Laurent Montes, Marco Pala, Mireille Mouis (thanks for accepting my expensive mission in Japan) and especially Sorin Cristoloveanu for his constant support and trust over these three years. Many people also contribute to the good spirit in IMEP-LAHC. My thanks for these good moments we have shared go to Lionel Bastard for his humour, Elise Ghibaudo for her kindness Jean Emmanuel Broquin for his engagement in his work and his forever useful advices, Lionel Duvilaret for his passion for science, Delphine Constantin (from CIME) for her enthusiasm and Gregory Grosa for his authenticity.

In addition to my research activities, I also carried out many teaching activities. I would like to thank the people who gave me the opportunity to enjoy the hard but fantastic task of teaching: Youla Morfouli, Jean Emmanuel Broquin, Laurent Montes, Elise Ghibaudo and Phillipe Benech. I also enjoyed a lot the many discussions I had with other teachers : Irina Ionica, Nathalie Mathieu, Yannis Le Gennec, Emmanuel Pistono and Davide Bucci. I hope that their supports and advices will help me to become an as good teacher as they are.

I also get a lot a support from the Italian side. I would like to thank David Esseni for the much interesting discussion we had about my work and for his comprehensive knowledge of carrier transport. My thanks also to Francesco Driussi for his support and his passion of Friul.

I also would like to thank Pierre Gentil, former head of the EEATS PhD department and head of the micro and nano electronics specialty, for having encouraging me in my work and for giving me the opportunity to be part to the organization of Minatec Crossroads.

Hence, my PhD has been influenced by many experienced people: different boss different "teachers" and different permanent people of my labs. But I have not been influenced and helped by these great people only. Therefore, I would like to thank the many young researchers I have met during my PhD and in these labs.

In IMEP-LAHC, I would like to thank the whole A313 office. We all know how much we helped and support each other. Without them, these three years would not have been so exiting and funny. Going to work being happy because you know you are going to see great guys is a chance.

So, I would like to thank Christophe “Tof” Hoarau, for his engagement in work, for his sensitivity in life, for his steady way of being that has always calmed me. Thank you for all the moment we have spend climbing, or at the pub, or in lives. True punks always get along well.

I also thank Maxime “Max” Bernier, for the unique and warm atmosphere he gave to the office. He contributes a lot to our scientific emulation by filling the gaps between our fields. After all, we are only dealing with waves (or vibes). Thank you for being so genuine.

And finally, I thank Bruno “Nob” Martin for our endless discussion about science, teaching, music, life etc. Thanks for “The Cinematic Orchestra” and for our endless parties. Thank you also for your trust.

I would also like to thank the many PhD students I have met in IMEP-LAHC. The old ones: Marlène, Wipa, Leily, Thomas G., Raphaël S., Jerome. The ones still there : Bogdan B., Guillaume B.M., Tuan and Louis P. The young ones : Loan, William, Louis G., Simon, Thomas L, Bertrand, Lydie, Armin, Alina and especially my Italian buddy in IMEP, Claudio B and to the new comer Stephan. May your roads be full of good scientific moments and full of happiness.

Once again, I duplicate my thanks to these young researchers toward the Italian side.

I would send a special thank to my Udinese buddy, Nicolas Serra. I would like to thank him for his friendship, for showing me the good place in Udine, for bringing me in parties and in nice Friulan places. I owe you a lot. I also thank his friend (Francesco and Simone) and family for having welcoming me so nicely.

My thanks also goes to the young researcher in SelmiLab : Marco (hope you had fun in Grenoble), Elisa, Francesco C, Paolo T., Antonio A., Davide, and a special thank to a non PhD student, Marinella.

I have also been encouraged by many people outside of my lab, and in particular in ST Microelectronics and in CEA LETI. I would like all the Ge Team member : Mélanie, Estelle, Frederic Boeuf (once again), Stephane Monfrey. In the advance device group : Nicolas Loubet and Gregory Bidal for the good moment spent in Japan. I would like to thank Thomas Skotnicki for giving me the opportunity to present my results in the framework of the Ge Team, an informal working group which has been highly motivating for me. In the TCAD/Compact modelling group I would like to thank Denis Rideau for his support and encouragement, Maxime and Alban. In CEA-LETI, I would like to thank the many people that followed my work after my training period in 2004 : Maud Vinet (once again), Thierry Poiroux, Bernard Guillaumot, Thomas Ernst, Julie Widiez and Olivier Weber. I would like to give a special thank to Yves Morand for his constant support and for his priceless friendship. Many PhD student of CEA-LETI have also encouraged me each time they have seen my work: Cecilia, Florent, Vincent B., Benjamin V., Mickael C. and Louis H.

Of course, managing a PhD is not only a matter of great professional context. During my PhD, my friends have also support me a lot, with their attention, friendship and most importantly, patience.

My first thanks go to Raph, for always being there when I need somebody, and most of time when I don't even ask for it. Without you my buddy, I wouldn't be what I am right now.

I would like to thank Perrine, for the same reasons, and also for always organizing in such a great way the important moment of my life – birthdays and defence meals. I would like to thank her for our endless discussion about everything, but only about what only and really matter… Those few lines won't be enough, but *you know what I mean by*. May this world understand you and may you be happy in life as much as you deserve it.

Many thanks to the Poyets crew. Old buddies are forever present, even if time goes by and weaken some link. To Géraud, Fab, Matt, Titi, Yann, Vinz, Ced and Guillaume, I wish you the best, that I know you will get it soon or later.

Thanks to Maxime "sapeur" Ailloud for always reminding me where I come from and for is incredible sense of humour.

Thanks to my panther, Aurélia, for being my explosive source of energy. Thanks to Marie and Lolo, for your love that I don't deserve. Thanks to Zoé, for your sensitivity that gives me hope. Thanks to Mélanie for what we have shared. All these fantastic women know how much I need them to carry out what I have chosen to be my way. I wish all of you to be loved the way you deserve it and to be recognized in this world for what you truly are.

Thanks to Karim, for his sensitivity and his friendship. I wish you all the best my buddy.

Thanks to Carine and Diego for being the incarnation of happiness even in difficult times. And thanks to the Gully family for the good things we have lived, which made who I am right now.

Many thanks to Romain (and Sophie) and Antoine, for the good moments we have shared (in France and Japan) and for the one we will share again (in France and maybe in Japan).

I would like to thank Jean for trusting me so much and for being one of the nicest guys ever.

Finally and most importantly, I want thank my family. Without them obviously, nothing would have been possible. To my mum, for being my constant model. To Fred, for all that I learnt and that I still learn form you. To his parents, Erika and Claude. To my sister Axelle, for being so surprising in life. To my grandparents, and especially my grandfather. This work is dedicated to him, the first scientist of my family who did not have the chance to carry out my fascinating studies.

Content

Abstracts 13
Abstract 14
Résumé 16
Riassunto 19
Chapter 1 : Introduction 21
1.1 Context : why alternative channel materials ? 22
1.1.1 Birth, growth and challenges of the semiconductor industry 22
1.1.1.1 Birth of the semiconductor industry 22
1.1.1.2 The silicon MOSFET, technical key of a success 23
1.1.1.3 End of the "Happy scaling" era 25
1.1.2 Forthcoming challenges for the semiconductor industry 25
1.2 State of the art in the alternative channel material CMOS performance modeling 28
1.2.1 Literature review 28
1.2.2 Aim of the thesis 31
Chapter 2 : Ballistic On current of nano nMOSFETs featuring arbitrarily oriented alternative channel material 33
2.1 Introduction 34
2.2 Modelling of the ballistic on state current of arbitrary oriented alternative channel DGFETs 35
2.2.1 Carrier transport in the full ballistic regime 35
2.2.2 The Natori model of full ballistic transport 36
2.2.3 Generalized Natori model 43
2.3 Impact of channel material and channel orientation on the on state performance of ultra-scaled DGFETs 51
2.3.1 Impact of channel direction in (100) and (111) substrates 51
2.3.2 Impact of channel direction in (110) substrates 53
2.3.2.1 Semiconductors optimum channel orientations on the (110) surface 53
2.3.2.2 Impact of confinement on Anisotropy 55
2.3.2.3 Transport in (110) substrate compared to (100) and (111) 58
2.3.3 Impact of the bandstructure modification in presence of strong quantization: a literature review 59
2.4 Conclusion 61
Chapter 3 : Source-drain leakages in alternative channel material 63
3.1 Introduction 64
3.2 Modelling of subthreshold source-drain leakage mechanisms 65
3.2.1 Impact of source-drain leakage mechanisms on the device performance 65
3.2.2 Short Channel Effect and Drain Induced Barrier Lowering (SCE and DIBL) 66
3.2.3 Source to Drain Tunnelling (SDT) 70
3.2.3.1 Starting equations 70
3.2.3.2 Transparency calculation 71
3.2.3.3 Multi-subband channel orientation dependent source-to-drain tunnelling current model 73
3.2.3.4 Single subband, channel orientation independent source-to-drain tunnelling current model 76
3.2.4 Band to Band Tunnelling (BBT) 77
3.3 Impact of source-drain leakages on the performances of alternative channel material nano-MOSFETs 80

3.3.1 Comparing channel material ... 80
3.3.1.1 Device orientation optimisation ... 80
3.3.1.2 Alternative channel material MOSFET performance comparison ... 81
3.3.1.3 Conclusions ... 86
3.3.2 Role of effective masses and band gaps on the performances of nano nMOSFETs ... 87
3.3.2.1 Models and methodology ... 87
3.3.2.2 Results and discussions ... 89
3.3.2.3 Conclusions ... 94
3.4 Conclusion ... 95
Chapter 4 : Scattering and Quasi-Ballistic (QB) transport in alternative channel material nano-nMOSFETs ... 97
4.1 Introduction ... 98
4.2 The Boltzmann Transport Equation and the Monte Carlo approach ... 99
4.2.1 The Boltzmann Transport Equation (BTE) ... 99
4.2.2 Monte Carlo (MC) solution of the BTE ... 101
4.2.2.1 Principle of Monte Carlo simulations ... 102
4.2.2.2 Main inputs of a MC simulator ... 102
4.3 Specificities of the Multi Subbands Monte Carlo ... 108
4.4 Germanium and gallium-arsenide bulk mobility ... 111
4.4.1.1 Bulk crystal mobility solver ... 111
4.4.1.2 Mobility calculation using a Multi Subbands Monte Carlo code ... 113
4.5 Germanium inversion layer mobility ... 115
4.5.1 The nMOS mobility issue ... 115
4.5.2 Monte Carlo simulation study ... 116
4.5.3 Inversion layer mobility in Germanium On Insulator (GeOI) nMOSFET ... 121
4.6 Quasi Ballistic transport in Ge DGFETs ... 123
4.6.1 The Lundstrom model of quasi-ballistic transport ... 123
4.6.2 Monte Carlo simulations of backscattering in Ge DGFETs ... 125
4.6.3 Results and discussion ... 126
4.7 Conclusions ... 129
Chapter 5 : Conclusion ... 131
5.1 Conclusions ... 132
5.2 Outlook ... 135
Publication of the author ... 137
Bibliography ... 141
Appendix 1 ... 153
Brief history of the microelectronic industry ... 154
Birth of the microelectronic industry ... 154
Growth of the microelectronic industry ... 156
Increasing the ICs complexity ... 156
Appendix 2 ... 159
Literature review of the modelling of expected performance of alternative channel material ... 160

Abstracts

Abstract

The continuous scaling of the MOSFET devices carried out in the semiconductor industry during the past forty year is presently facing technical issues. In addition, the deca-nanometric size of these devices induces a transition of the transport mechanisms involved in their operations. The close to equilibrium transport occurring in long channel devices is expected to progressively evolve toward a far from equilibrium process for ultra-short channel.

As this transition in transport regimes is expected to slow down the increase of performances induced by conventional device scaling, additional technological booster are currently investigated at the research level. In this context, the replacement of silicon as channel material by alternative (high mobility) channel has been identified as a possible source of major performance enhancement.

Experimental realizations with alternative material have already demonstrated significant transport improvement for long channel devices. However, these advance devices will not be introduce before the 22 nm node of the ITRS, which specify gate length below 15nm for high performance technologies. The performance of such ultra-scaled technology is thus an issue, as the promising results of long channel device are not certain to be maintained at short scale.

The aim of this work has therefore been to theoretically investigate the performance enhancement of alternative channel material devices featuring ultra scaled channel length.

The detailed motivation of this work, illustrated by the state of the art studies in alternative channel material simulation, is given in chapter 1. The modelling of alternative channel material devices in the fully ballistic limit is then addressed in chapter 2 and 3.

The on state current and the impact of the channel orientation on the performances of these devices are investigated in Chapter 2. A generalized Natori model of the fully ballistic current is derived for any channel material and any channel orientation and used in this chapter to study the ballistic drain current as a function of the channel surface and in-plane orientation. It has been demonstrated with this model that the ballistic current of devices on a (100) and (111) surface was isotropic. On the contrary to the (100) and (111) surfaces, devices on a (110) surfaces has been found to feature anisotropic ballistic drain current. The best current direction on this surface has then been found to be dependent of the valley relative population: if the Δ valley is significantly filled like in the case of Si, GaP and AlAs, then the best current direction is the [100] direction, whereas the best direction is in the [110] direction of the Λ valleys are more occupied, as in the case of Ge, GaAs, InAs and InSb. Finally, it has been found in addition that the (110) is the best surface orientation of Ge, GaAs, InAs and InSb devices provided that their channel are aligned in the [110] direction.

The following chapter has then been dedicated to the comparison of alternative channel material. This task has required the modelling of the most impacting leakage mechanisms on the performances of such devices. These mechanisms have been identified in the literature as the Short Channel Effects, the Source-to-Drain Tunnelling and the Band-to-Band Tunnelling. Semi-analytical models of these effects have therefore been derived, benchmarked and to determine the most promising channel material. The results obtained with these models have indicated that significant tunnelling leakage strongly reduces the performance of alternative channel material devices whose gate lengths is smaller than 15nm. In addition, it has been

shown that silicon and strained silicon are less sensitive to this tunnelling leakage current thanks to larger effective masses.

This last point has been more deeply investigated in the end of chapter 3, using a simplified analytical model of the Ion-Ioff trade-off in the fully ballistic limit. Contrary to the previous approach which consists in comparing various semiconductors, this model has enabled to evaluate the performance of an ultra-scaled device by considering the channel effective mass and energy bandgap as variable and not only as simple material parameters. The results obtained using this original approach has shown that a maximum of on current as could be obtained for an optimum mass. This trade-off results from the competition of two opposed mechanisms enhanced by the effective mass reduction, i.e. the beneficial increase of injection velocity and the detrimental increase of source-to-drain tunnelling. Band-to-Band Tunnelling has however been found to only impact devices with indirect channel material whose energy bandgap and effective mass are small (bandgap below 1eV and effective mass below $0.1m_0$). These results have therefore suggested that the impact of Source-to-Drain Tunnelling is stronger than the impact of Band-to-Band Tunnelling for channel length below 15nm.

The role of carrier scattering in alternative channel material has finally been studied in chapter 4. The rigorous treatment of carrier scattering have implied to use more comprehensive modelling tool like Monte Carlo simulators. In this work, a Multi Subband Monte Carlo code, which account for the impact of quantum confinement and degeneracy on transport properties, has been at first extended and then used to investigate the performances of germanium channel devices. In an attempt to explain the poor performances observed experimentally in germanium nMOSFET, it has been shown in this chapter that the inversion layer electron mobility of germanium is significantly degraded by the filling of the penalizing Δ valleys. This effect has then been found to be amplified in Germanium On Insulator structure, due to the thin thickness of the semiconductor layer. Finally, the carrier mean free path in germanium has been demonstrated to be almost linearly dependent of the low field mobility in inversion layer. This important results, already obtained for silicon, links an high field and short scale transport figure of merit with a low field and long scale one and suggest that an high quasi-ballistic current can not been attained in germanium unless high mobility are obtained in long channel devices.

This work has therefore given a more complex picture of the performance of alternative channel material devices, whose scalability toward the sub 20nm dimension is questionable.

Résumé

Le processus de réduction des dimensions des transistors MOS qui a débuté il y a 40 ans fait face actuellement à de nombreuses difficultés technologiques. En parallèle, le transport des porteurs dans les canaux déca-nanométriques évolue progressivement d'un régime proche de l'équilibre à un régime hors équilibre.

Cette transition de régime de transport s'accompagne d'une augmentation moins importante que prévue des performances des transistors MOS lors de la réduction de leur dimension. Dans ce contexte, il est donc nécessaire d'introduire de nouvelles options technologiques améliorant le transport. Le remplacement du silicium par des matériaux de canaux alternatifs est ainsi un des exemples des techniques envisagées pour continuer d'augmenter les performances de transistor MOS à effet de champs.

Des transistors (à canal long) fabriqués à partir de germanium ou de GaAs ont déjà démontré des gains de performances encourageants. Cependant, de tels dispositifs innovants n'entreront pas en production avant le nœud 22nm de l'ITRS, qui spécifie des longueurs de canaux inférieur à 15nm. Les performances de ces transistors ultra-courts restent donc une question ouverte, car il n'est pas garanti que les gains en performance obtenus à grande échelle soient conservés pour ces dimensions.

L'objectif de ce travail est donc d'évaluer théoriquement les gains en performance de transistors ultra-courts à matériaux de canal alternatif.

Le premier chapitre de cette thèse introduit les objectifs de cette étude, ainsi que l'état de l'art de la modélisation des dispositifs à matériau de canal alternatif. La modélisation de ces transistors dans la limite totalement balistique est ensuite traitée dans les chapitres 2 et 3.

Le chapitre 2 présente plus particulièrement l'étude de l'influence de l'orientation du canal de conduction (autant en ce qui concerne la surface cristalline du substrat que l'orientation du transistor dans le plan cristallin considéré). Un modèle de courant balistique de type Natori, valable pour tous les matériaux semi-conducteurs et pour une orientation de canal quelconque, est établi au début de ce chapitre. Ce modèle est ensuite utilisé pour démontrer analytiquement l'isotropie du courant de drain pour les transistors réalisés sur des substrats de types (100) et (111). Dans le cas de la surface (110), le courant balistique est au contraire anisotrope. Sur cette surface, la meilleure direction d'injection dépend de la population relative des vallées. Dans le cas où les vallées Δ sont majoritairement peuplées (comme dans le cas du Si, GaP ou AlAs), la meilleure orientation du canal sur la surface (110) est dans la direction cristalline [100]. Dans le cas où les vallées Λ sont les plus peuplées, (comme dans le cas du germanium, GaAs, InAs ou InSb), la meilleure orientation du canal sur la surface (110) est dans la direction cristalline [110]. De plus, dans le cas du germanium, GaAs, InAs ou InSb, le courant maximum, toutes directions de canal confondues, est obtenu pour la surface [110] et pour une orientation cristalline [110].

Le chapitre suivant est dédié à la comparaison des performance des matériaux alternatifs. Pour cela, il est nécessaire de prendre en compte les mécanismes de fuites tunnel entre source et drain à l'état «off» qui détériorent fortement les performances de ces dispositifs. En accord avec la littérature, les mécanismes prépondérants sont les effets de canaux courts, le courant tunnel source drain direct et le courant tunnel bande à bande. Les modèles semi-analytiques

de ces courants de fuites sont établis au début du chapitre 3, puis comparés à des méthodes plus précises (simulation numérique ou résultats présentés dans la littérature) et enfin utilisés pour estimer les performances de différents dispositifs à matériaux de canal alternatifs. Les résultats obtenus montrent que les courants de fuites tunnel réduisent fortement les performances de transistors à canaux en germanium et en GaAs pour des longueurs de grilles inférieures à 15nm. Les canaux en silicium ou en silicium contraint semblent être par ailleurs moins affectés par ces courants de fuites.

Un modèle analytique simplifié du courant à l'état « on » et à l'état « off » est proposé à la fin du chapitre 3 pour étudier cette dégradation plus en détail. Il permet d'aborder cette problématique d'une manière différente : contrairement à l'étude précédente qui comparait des matériaux semi-conducteurs entre eux, celle nouvelle approche évalue l'impact des paramètres clefs des matériaux sur les performances de dispositifs ultra-courts. Ainsi, les courants à l'état « on » ont été estimés pour un courant à l'état « off » constant en considérant les masses effectives et les bandes d'énergies interdites comme de simples variables. Les résultats obtenus montrent qu'il existe un maximum de courant à l'état « on » en fonction des masses effectives, et donc qu'il existe un compromis entre grandes et petites masses effectives. Ce compromis résulte de l'effet bénéfique des masses effectives faibles qui augmentent la vitesse d'injection des porteurs impliqués dans le courant balistique, et de l'effet pénalisant de ces mêmes masses sur l'augmentation du courant tunnel source-drain direct. En ce qui concerne le courant tunnel bande à bande, les résultats montrent qu'il serait négligeable par rapport au courant tunnel source-drain direct, sauf pour les matériaux à faible gap indirect et à faible masse effective (gap inférieur à 1.0 eV et masse effective inférieure à 1.0 m_0). Ceci suggère donc que le courant tunnel source-drain direct soit le principal facteur limitant les performances des transistors à matériaux de canaux alternatifs (pour des dispositifs dont les longueurs de grilles sont inférieures à 15 nm).

Le quatrième et dernier chapitre de cette thèse présente l'étude de l'impact des collisions sur les performances des transistors à matériau de canal alternatifs. Le traitement rigoureux de ces mécanismes de collision implique l'utilisation d'outils plus complexe que les modèles analytiques exposés dans les chapitres précédents. Dans le cadre de cette étude, un code de simulation Monte Carlo Multi Sousbande est utilisé pour prendre en compte les effets du confinement et de la dégénérescence des porteurs sur le transport dans les canaux de germanium. Cette approche est d'abord détaillée au début de ce chapitre. Elle ensuite utilisé pour étudier les faibles mobilités observées expérimentalement dans le cas des transistors nMOS à canaux en germanium. Les résultats obtenus montrent qu'une forte dégradation de la mobilité est obtenue par simulation, mais insuffisante pour réellement expliquer les mesures. Cette dégradation théorique est expliquée par le remplissage des vallées Δ du germanium, qui possèdent de très faibles mobilités en comparaison des vallées Λ. Cet effet est amplifié dans les structures « Germanium sur isolant », en raison de la faible épaisseur du film de semi-conducteur qui augmente l'impact des effets quantiques. Enfin, ces simulations ont permis de mettre en évidence la relation de dépendance quasi-linéaire entre le libre parcours moyen des porteurs dans les canaux de germanium et la mobilité en champs faible. Ce résultat important relie deux quantités conceptuellement très différentes, puisque la première correspond à un transport à courte échelle et en champs forts et la deuxième à un transport sur longue distance en champs faibles. Ceci implique que de forts courants quasi-balistiques ne seront atteints dans les transistors nMOS à canaux en germanium que si de fortes mobilités sont obtenues pour les dispositifs à canaux longs.

En conclusion, ce travail a démontré que les bonnes performances obtenues pour des transistors à canaux longs étaient fortement dégradées pour des canaux ultra-courts (inférieurs à 15nm). Il serait donc peut-être intéressant de proposer une nouvelle feuille de route pour les dispositifs à matériaux canal alternatifs. En effet, sur des dimensions supérieures à 15nm, leurs performances pourraient dépasser celles des dispositifs à canaux en silicium.

Riassunto

Il continuo *scaling* dei dispositivi MOSFET intrapreso dall'industria dei semiconduttori negli ultimi quarant'anni sta attualmente affrontando difficoltà tecniche. Oltretutto, la dimensione decananometrica di questi dispositivi induce una progressiva transizione dei meccanismi di trasporto coinvolti nel modo di funzionamento. Si attende che il trasporto in condizioni vicine all'equilibro evolva progressivamente verso un processo lontano dall'equilibrio nel caso di canale ultra corto.

Dato che si attende che tale transizione nei regimi di trasporto rallenti progressivamente l'aumento delle prestazioni indotto dallo *scaling* convenzionale, a livello di ricerca si sta investigando su soluzioni tecnologiche atte a migliorare le performance. In questo contesto, la sostituzione del silicio come materiale di canale con un canale alternativo (ad alta mobilità) é stata identificata come una possibile origine di miglioramento delle prestazioni.

Realizzazioni sperimentali con materiali alternativi hanno già dimostrato un miglioramento significativo del trasporto per dispositivi a canale lungo. Tuttavia, tali dispositivi avanzati non saranno introdotti prima del nodo tecnologico di 22 nm dell'ITRS, che specifica una lunghezza di gate inferiore ai 15 nm per tecnologie ad alte prestazioni. Le performance di questa tecnologia a tale livello di miniaturizzazione rappresenta quindi ancora un dibattito aperto, in quanto non si é certi che i risultati promettenti dei dispositivi a canale lungo siano mantenuti a piccole dimensioni.

L'obiettivo di questo lavoro é quindi stato di investigare teoricamente il miglioramento delle prestazioni di dispositivi ultra corti a canale prodotto con materiali alternativi.

La motivazione dettagliata di questo lavoro, illustrata dallo *state of the art* degli studi di simulazione di canali con materiali alternativi, é presentato nel capitolo 1. La modellizazione di dispositivi a canale prodotto con materiali alternativi nel limite completamente ballistico é illustrato nei capitoli 2 e 3.

La corrente nello stato "on" e l'impatto dell'orientamento del canale sulle prestazioni di questi dispositivi é investigato nel capitolo 2. Un modello generalizzato di Natori della corrente completamente ballistica é stato derivato per ogni materiale e per ogni orientamento di canale ed é stato utilizzato in questo capitolo per investigare la corrente ballistica di drain in funzione della superficie di canale e dell'orientamento nel piano. E' stato dimostrato con tale modello che la corrente ballistica su dispositivi su una superficie con orientamento (100) e (111) é isotropica. Al contrario delle direzioni (100) e (111), dispositivi su una superficie con orientamento (110) presentano un'anisotropia della corrente ballistica di drain. Si é trovato che la migliore direzione della corrente su questa superficie é dipendente dalla popolazione relativa delle valli: se la valle Δ é riempita significativamente come nel caso del Si, GaP e del InAs, allora la migliore direzione per la corrente é la (100), mentre la migliore direzione risulta essere la (110) se le valli Λ sono più occupate, come nel caso del Ge, GaAs, InAs e InSb. In aggiunta a ciò, si é trovato che la (110) é il migliore orientamento per il Ge, GaAs, InAs e InSb se il canale del dispositivo é allineato alla direzione (110).

Il capitolo seguente é stato quindi dedicato alla comparazione tra differenti materiali alternativi per il canale. Questo compito ha richiesto la modellizzazione dei meccanismi di perdita più importanti su tali dispositivi. Questi meccanismi sono stati identificati in

letteratura come gli effetti di canale corto (SCEs), il Source-to-Drain Tunneling ed il Band-to-Band Tunneling. Modelli semi analitici di tali effetti sono stati quindi derivati e validati per poi determinare il materiale di canale più promettente. I risultati ottenuti con questi modelli hanno indicato che una significante perdita dovuta al tunneling riduce fortemente le prestazioni di dispositivi con canale composto da materiali alternativi nel caso in cui la lunghezza di gate sia inferiore ai 15 nm. In aggiunta a ciò, si é mostrato che il silicio ed il silicio *strained* sono meno sensibili a questa perdita dovuta al tunneling per il valore più elevato delle masse effettive.

Questo ultimo punto é stato investigato più attentamente alla fine del capitolo 3, usando un modello analitico semplificato del compromesso Ion-Ioff nel limite completamente ballistico. Contrariamente all'approccio precedente in cui si confrontavano diversi semiconduttori, questo modello ha permesso di analizzare le prestazioni di un dispositivo ultra corto considerando le masse effettive di canale ed il *bandgap* di energia come delle variabili e non solo come dei semplici parametri del materiale. I risultati ottenuti usando questo metodo originale hanno mostrato che é possibile ottenere una corrente massima per una massa effettiva ottimale. Questo compromesso sorge dalla competizione di due meccanismi opposti aumentati dalla riduzione della massa effettiva, i.e. l'aumento positivo della velocità di iniezione e l'aumento dannoso del source-to-drain tunneling. Si é scoperto che il band-to-band tunneling ha un impatto significativo solo in dispositivi il cui materiale é a bandgap indiretto e piccolo e le cui masse effettive sono piccole (bandgap inferiore a 1 eV e masse effettive inferiori a $0.1m_0$). Tali risultati suggeriscono che l'impatto del source-to-drain tunneling é più forte di quello del band-to-band tunneling per lunghezze di canale inferiori a 15 nm.

Il ruolo dello scattering dei portatori in canali a materiale alternativo é stato quindi studiato nel capitolo 4. Il trattamento rigoroso dello scattering dei portatori ha implicato l'uso di strumenti più rigorosi come i simulatori Monte Carlo. In questo lavoro, un codice Monte Carlo Multi Subband (MSMC) – che considera l'impatto del confinamento quantistico e della degenerazione sulle proprietà di trasporto – é stato inizialmente esteso e quindi utilizzato per investigare le prestazioni di dispositivi a canale di germanio. In un tentativo di spiegare le scarse prestazioni osservate sperimentalmente negli nMOSFET a germanio, é stato mostrato in questo capitolo come la mobilità degli elettroni nello strato di inversione del germanio sia significativamente degradata dal riempimento delle valli Δ (penalizzanti per il trasporto). Si é poi trovato che tale effetto é amplificato in strutture Germanio su Isolante (GOI), a causa del ridotto spessore dello strato di semiconduttore. In aggiunta a ciò, si é dimostrato che il libero percorso medio nel germanio dipende in maniera quasi lineare dalla mobilità *low field* nello strato di inversione. Questo risultato importante, già ottenuto per il silicio, relaziona un indice di prestazione del trasporto ad alto campo ed a piccola scala con una a debole campo ed a larga scala e suggerisce che una forte corrente quasi ballistica non può essere raggiunta nel germanio a meno di ottenere elevate mobilità in dispositivi a canale lungo.

Questo lavoro ha quindi offetro un'immagine più complessa delle prestazioni dei dispositivi con canali basati su materiali alternativi, la cui miniaturizzazione al di sotto dei 20 nm resta discutibile.

Chapter 1 : Introduction

Chapter 1 : Introduction 21
1.1 Context : why alternative channel materials ? 22
1.1.1 Birth, growth and challenges of the semiconductor industry 22
1.1.2 Forthcoming challenges for the semiconductor industry 25
1.2 State of the art in the alternative channel material CMOS performance modeling 28
1.2.1 Literature review 28
1.2.2 Aim of the thesis 31

1.1 Context : why alternative channel materials ?

Alternative channel material in MOSFET devices has recently attracted much interest in the semiconductor device research community. This subsection aims to review the historical and scientific motivation of the replacement of silicon as a channel material.

1.1.1 Birth, growth and challenges of the semiconductor industry

1.1.1.1 Birth of the semiconductor industry

A careful look at the history of the birth of the semiconductor industry (see Appendix 1) shows that nearly 10 years of intense research on solid-state physics at the Bell Telephone Laboratory have been necessary for John Bardeen, Walter Brattain and William Shockley to fabricate the first transistor in December 1947. This transistor, shown in
Figure 1.1, was a point contact one. It was based on the current modulation of a germanium diode by the injection of holes from a third contact. Quickly following this invention, germanium point contact transistors have been industrially produced and commercialized. Soon after, the point contact architecture has been replaced by the bipolar one, still using germanium as semiconductor material.

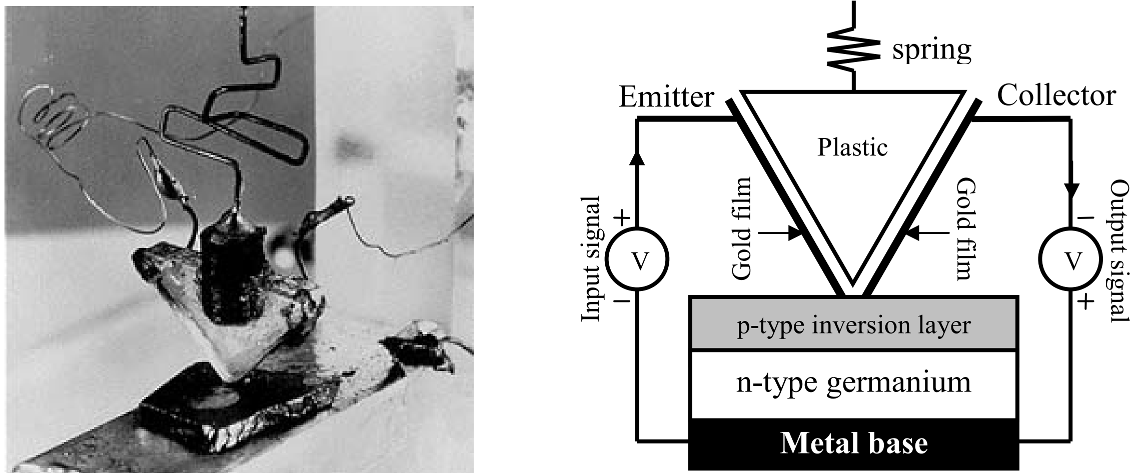

Figure 1.1 : a) Picture of the first point contact transistor fabricated at Bell Labs by Walter Brattain. b) Scheme of a point contact transistor

Despite its high carrier mobilities, the use of germanium has however always been an issue, principally due to its small energy bandgap (0.66eV at room temperature), which makes these devices thermally instable: Ge becomes intrinsic at not so high temperature (because of the transistor self heating, but most generally because of the environment), which eliminates the distinction between the p and n-doped region thus causing failure of device operation. The germanium based transistors were therefore replaced within few years by bipolar silicon transistors, which presented higher thermal stability thanks to the larger silicon energy bandgap. The comparison between the intrinsic temperature as a function of the impurity concentration is given in Figure 1.2.

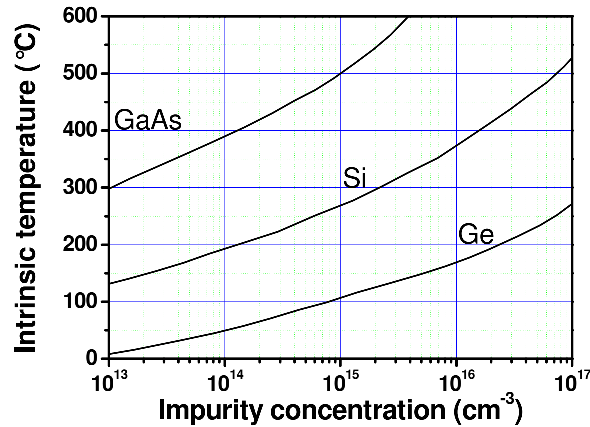

Figure 1.2 : Intrinsic temperature as a function of the impurity concentration (taken from [SzePhySC])

Later, in the beginning of the 60s, further developments at the Bell Labs in crystal growth, silicon oxidation and doping techniques lead to the fabrication of the first Metal Oxide Semiconductor Field Effect Transistor (MOSFET). At the same period, the first integrated circuit was invented and fabricated by Texas Instrument and Fairchild Semiconductor.

The combination of these two winning strategies, i.e. the use of integrated circuit with silicon MOSFETs, gave birth to one of the most significant industrial revolutions of the XXth century.

1.1.1.2 The silicon MOSFET, technical key of a success

One of the main technical origins of the success of the semiconductor industry is undeniably the use of silicon Metal Oxide Semiconductor Field Effects Transistors as core device.

For digital application, which is the main produced and commercialized technology, silicon MOSFET is clearly superior to other transistors thanks to:

- Its cost effectiveness, resulting from the planar process involved in its fabrication and the abundance of silicon (roughly 25% of earth's crust) ;
- Its stable oxide layer, not obtainable from other semiconductors, enabling a low power shift from off to on state ;
- The possibility to obtain nearly ideal complementary MOS switches thanks to n- and p-type devices with quite well balanced characteristics
- Its increase of performance when properly scaled.

The last point is particularly relevant since the performance enhancement and the increase of devices density enabled by MOSFET scaling has been – and is still – the key challenge for the semiconductor industry: increasing the device density allowed the design of more and more complex functions and reduced drastically the cost of a single transistor[1]. In parallel, the ICs global performances have been increased (higher frequency) and the total power

[1] See the Moore's law and the ITRS report in Appendix 1

consumption can be reduced (same performance at lower voltage). This ability of the MOSFET to present higher performances while scaled down allowed a fast and steady growth of the semiconductor industry for almost 40 years.

The MOSFET performance gain with scaling can be roughly estimated using simple qualitative expression of the intrinsic transistor switching time of a long channel MOSFET (time required to remove the charge from the channel of the transistor, neglecting the effect of parasitic capacitances):

$$\tau \approx \frac{CV}{I_{on}} \approx \frac{C_{g_{eff}} W \, L \, V_{DD}}{\frac{W}{L} C_{g_{eff}} \, \mu \frac{V_{DD}^{2}}{2}} = \frac{2L^{2}}{\mu V_{DD}} \tag{1.1}$$

With C_{geff} the effective gate capacitance, V_{DD} the supply voltage (assumed higher than the threshold voltage), μ the low field mobility, W the transistor width and L the gate length as schematized on Figure 1.3.

Equation (1.1) therefore shows that when the gate length is reduced by a factor *k* (with $k > 1$) at a constant supply voltage V_{DD}, the intrinsic switching time τ is decreased by a factor k^2 . In practice, a set of more complex scaling rules are use to define the MOSFETs dimensions and bias conditions for the future generation of devices [BaccTED82] [SkotTED08], as a function of their application (low power or high performance devices). For example, reliability issues force to also reduce the supply voltage with the device scaling.

It has to be mentioned however that the intrinsic switching time defined as in (1.1) is mostly meaning full for high performance devices. Indeed, when the parasitic capacitances of the MOSFET and of the circuit interconnections dominate the overall capacitances, the on current I_{on} should also be optimized as well as τ.

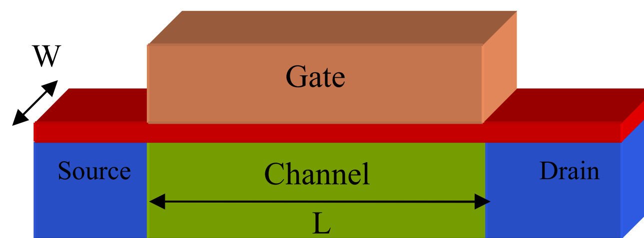

Figure 1.3 : Scheme of a long channel MOSFET

The dielectric layer also makes the MOSFETs more attractive compared to other transistors. Compared to bipolar transistor in which the commutation is governed by a current, the MOS capacitor enable a low power switch from the off to the on state.

The use of silicon in MOSFETs has thus been almost compulsory in this context, since no stable semiconductor oxide have been obtained from Ge, or other III-V compounds. In comparison, the very stable one obtained from dry oxidation of a Si substrate was an almost perfect and simple technological solution.

1.1.1.3 End of the "Happy scaling" era

The scaling rules have been successfully applied during the 70s and the 80s, called the "Happy scaling" era, enabling a constant growth of the semiconductor industry. However, many physical limitations were foreseen to stop it. In the 80s, the submicronic scale was expected to lead to too high Short Channel Effect (electrostatic parasitic effects occurring when source and drain are too close - see 3.3.2.), and strong channel hot electron injection degrading the device stable operation in the long term. In the 90s, when the gate lengths were reaching half a micron, high access resistances were likely to lead to significant performance degradation. Finally, when the gate lengths reached 250nm, tunneling current through the oxide was foreseen as possible breakdown sources.

However technological solutions have been found in each case to avoid these limitations. Short Channel Effects are reduced thanks to engineered source, drain and channel doping profiles (lightly doped drain [OgurTED80] and pocket implants [WannTED96]), salicide source drain [IwaiMicEng02] are used to reduce parasitic access resistances and gate tunneling leakage is avoided thanks to the recent industrial introduction of higk-κ dielectrics [GuseMicEng01].

Nevertheless, new limitations are arising since the transistor gate length is expected to be scaled down to 7nm in 2018 [ITRS2007], partly due to the intrinsic physical limitation of silicon as a channel material. In addition, the former parasitic effects are also strengthened as devices continue to scale down. Therefore, new solutions are required to face these new technological challenges.

1.1.2 Forthcoming challenges for the semiconductor industry

Aside from many new technological issues (red brick wall of the ITRS [ITRS2007]), one of the major forthcoming challenges for the semiconductor industry deals with carrier transport limitations in silicon channels. Indeed, as the channel length now reached the decananometer scale, the impact of carrier scattering is becoming weaker [PaleTED05], whereas they were predominant at larger scale. Carrier transport thus enters a transition from close-to-equilibrium transport to strong non-equilibrium transport regime. All former transport model assuming close-to-equilibrium conditions, like Drift Diffusion transport models, are therefore not valid anymore and in addition, the concepts of mobility and velocity saturation become also questionable.

This far from equilibrium transport regime expected to occur in ultra short devices has been widely studied since the mid-90s. In particular, detailed studies of carrier transport in decananometer channels thanks to Monte Carlo simulation [PaleTED05] showed that, due to the weaker influence of scattering on carrier transport, a significant proportion of electrons can be emitted by the source to reach the drain without suffering any scattering. These electrons are thus ballistic.

When transport combines scattered and non-scattered (ballistic) carriers in comparable fractions, the transport regime is called quasi-ballistic, which is in essence a complex transition from long channel to ultra-short channel transport. It is also expected that fully

ballistic transport, i.e. governed by non scattered electrons only, will occur in ultra-scaled devices (i.e. for channel length around 10nm for silicon).

Another important difference between close to equilibrium and ballistic transport lies in the carrier velocity distribution along the channel. In the quasi or full ballistic regime, the feedback of a limited maximum velocity at the drain end of the channel on the current (through the self consistent potential) is no longer as strong as it used to be for longer devices. Theoretical studies [PaleTED05], [LundEDL97] showed on the contrary that ballistic transport is in fact rather limited by the carrier velocity on the source side, called the injection velocity.

In this context, equation (1.1) is no longer valid as it assumes a drift diffusion transport in a long channel MOSFET and needs to be rewritten in the framework of quasi or full ballistic transport. According to the Lundström model of quasi-ballistic transport [LundEDL97], equation (1.1) becomes:

$$\tau \approx \frac{CV}{I_{on}} \approx \frac{C_{g_{eff}} W\ L\ (V_{DD} - V_t)}{\left(\frac{1-r}{1+r}\right) W\ C_{g_{eff}} (V_{DD} - V_t) V_{inj}} = \frac{L}{\left(\frac{1-r}{1+r}\right) V_{inj}} \qquad (1.2)$$

With V_{inj} the injection velocity of the carriers (see section XXX) and r the backscattering coefficient (see section XXX), i.e the ratio of re-emitted electron toward the source by few scattering events. In the case of full-ballistic transport, r tends to 0, and equation (1.2) simply becomes:

$$\tau \approx \frac{CV}{I_{on}} \approx \frac{C_{g_{eff}} W\ L\ (V_{DD} - V_t)}{W\ C_{g_{eff}} V_{inj} (V_{DD} - V_t)} = \frac{L}{V_{inj}} \qquad (1.3)$$

Since in a properly scaled device, V_{inj} is independent of L, equation (1.2) and (1.3) show that, when quasi or full-ballistic regimes govern carrier transport, the dependence of the intrinsic switching time with the gate length at constant V_{DD} is not in L^2 anymore. Therefore, scaling will lead to a reduced performance improvement in the quasi or full ballistic transport regime than in the drift diffusion one.

In addition, the solutions actually employed to keep short channel effects under control severely degrades the mobility and the injection velocity, which adds showstoppers to the transport issue.

Consequently, and due to the loss of efficiency of conventional device scaling in nanometric dimensions, the injection velocity and the backscattering coefficient must be now optimized to continue the increase of performances. In the Natori (see section XXX and [NatoJAP94]) and the Lundström models, the injection velocity is described as strongly dependent of the subbands structure of the electron gas on the top of the source-drain barrier, called virtual source. Thus, an increase of the injection velocity is theoretically possible through subband engineering of the virtual source [TakaSSE05]. In addition, it has been shown that the backscattering coefficient is a function of the channel length, which then needs to be further reduced, and of the mobility [ClerTED06], [PaleIEDM06], which needs to be increased. This clearly expressed at low field by the flux theory which links the mobility, the mean free path in a ballistic transistor and the corresponding backscattering coefficient as :

$$r = \frac{L}{L + \lambda_0} \text{ with } \lambda_0 = \frac{2\mu_0 k_b T}{q v_{th}} \tag{1.4}$$

Non conventional channel material with improved electronic properties (especially increased mobility and reduced backscattering coefficient) and larger injection velocity are currently investigated as possible technological solutions.

Among these, the strain silicon technology is already industrially used to increase MOSFETs drive current. Although this solution has been developed mainly to improve mobility, it also provides better injection velocity compared to unstrained silicon in short channels [FerrierTNANO2007].

Another recently studied solution consists in the substitution of silicon for alterative channel material with larger mobilities (reduced backscattering) and larger injection velocities. This replacement has been enabled thanks to the recent progresses made in high-κ dielectric deposition making possible to realized devices without Si/SiO_2 stack. Example of MOSFETs with Ge, GaAs and InGaAs channels have already been fabricated. Table 1.1 gives an extensive list of references describing the fabrication of nMOSFET featuring these channel material.

Ge	GaAs	InGaAs
[RansTED91]	[KartEDL06]	[XuanEDL07]
[HuanIEDM03]	[YeEDL03]	[XuanEDL08]
[ShanEDL04]	[LeEDL04]	[ShahEDL08]
[WhanIEDM04]	[RajaEDL07]	[SunEDL07]
[YuEDL04]	[OkIEDM06]	
[YuEDL04_2]	[HillEDL07]	
[YuEDL05]		
[YeoEDL05]		
[BaiEDL06]		
[WuEDL06]		
[ZhanEDL06]		

Table 1.1 : List of reference describing the fabrication and the performances of nMOSFET with Ge, GaAs and InGaAs channel material.

The importance of alternative channel material has been underlined in the 2005 and 2007 edition of the International Technology Roadmap for Semiconductor reports (ITRS – see Appendix 1), clearly stating that *"to attain adequate drive current for the highly scaled MOSFETs* [below the 22nm technological node]*, quasi-ballistic operation with enhanced thermal velocity and injection at the source end appears to be needed. Eventually, nanowires, carbon nanotubes, or other high transport channel materials (e.g., germanium or III-V thin channels on silicon) may be needed"* [ITRSPID2007].

In conclusion, the technological effort must be supported by theoretical estimation of the possible performance gain brought by alternative channel material at nanometric small scales.

1.2 State of the art in the alternative channel material CMOS performance modeling

The previous section concluded on the importance of the theoretical performances evaluation of alternative channel materials. Many contributions have been published on this subject during the past years. Using a detailed literature review (see Appendix 2), this section presents the key points to be addressed for an accurate evaluation of the performance of ultra-scaled alternative channel material device. Finally, the approach chosen in this thesis is introduced.

1.2.1 Literature review

The *chronological* review of the literature regarding the performance evaluation of transistor with alternative channel material transistor performances detailed in Appendix 2 also underlines of the progress made in the modeling and simulation of these advance devices. M.V. Fischetti and S.E. Laux gave the first analysis of alternative channel material MOSFETs in the early 90s [FiscTED91_1,FiscTED91_2] thanks to full band Monte Carlo simulation approach. S.Takagi then proposed the first study of the impact of these material in the full ballistic regime [TakaVLSI03], introducing also the problematic of channel orientation optimization when a new channel material is used. In the same year, T. Low [LowIEDM03] gave a very detailed study of Si and Ge devices, accounting for most of the significant effect occurring in these devices. Numerous contributions comes from the Purdue group which insisted on the importance of rigorous treatment of the banstructure and on the impact of direct source-to-drain tunneling [RahIEDM03,RahIEDM04, RahIEDM05 ,LiuTED08 ,PalTED08]. The Stanford group however investigated the influence of band-to-band tunneling on alternative channel material performances [PethSISPAD04 ,PethIEDM05]. More recently, M.V. Fischetti and S.E. Laux revisited their work [FiscTED07 ,LauxTED07], updating their simulations in perspective of the work carried out by different groups (accounting for tunneling leakage for example), to provide a very detailed study of quasi-ballistic transport in alternative channel material. Finally the Udine's group [DeMiTED07] contributed in giving an analysis of the impact of the low density of states alternative channel materials. All these previous references have confirmed the interest for alternative channel material. However, in the 2007 edition of the IEDM, the Purdue group [CantIEDM07] showed that ultra-scaled alternative channel MOSFET suffer from severe performance degradation and that silicon channel device could outperform them because of increased source-to-drain tunneling induced by the small effective mass of high mobility channel materials.

Table 1.2 sums up the approaches, the main assumptions, and the results obtained by all the contributions mentioned.

	Architecture simulated	Channel material and orientation	Transport formalism	Bandstructure (e- gas dimension)	Leakages	Metric	Best channel material and best orientation (surface)/[transport]
M.V Fischetti and S.E. Laux [FiscTED91_1, FiscTED91_2]	Bulk MOSFETs	Si(100) Ge(100) GaAs(100) InGaAs(100) InP(100)	Monte Carlo	Full band (3D)	–	Intrinsic switching time	In based devices
S. Takagi [TakaVLSI03]	Bulk MOSFET UTB SOI FET	Si(100) Ge(100) Ge(111)	Single subband Natori model	Effective mass approximation (2D)	–	I_{on} at constant I_{off}	Ge(111)
A. Rahman et al [RahIEDM03]	DGFET	Si(100) Ge(100)	NEGF – NanoMOS	Effective mass approximation (2D)	SCE + SDT	I_{on} at constant I_{off}	Ge(100)
T. Low et a. [LowIEDM03]	DGFET	Si(100) Ge(100) Ge(110) Ge(111) with all in-plane orientation	NEGF – NanoMOS	Effective mass approximation (2D)	SCE + SDT + BBT	I_{on} at constant I_{off}	Ge(110)
A.Pethe et al [PetheSISPAD04]	DGFET	Si(100) Ge(100) Ge(110) Ge(111)	Natori model	Effective mass approximation (2D)	SCE	I_{on} at constant I_{off}	Ge(110)
S.E. Laux [LauxIEDM04]	DGFET	Ge, all possible orientations	NEGF – QDAME	Effective mass approximation (2D)	SCE + SDT	Intrinsic switching time	G(-4 4 21)/[110]
A. Rahman et al. [RahIEDM04]	DGFET	Ge(100)	Full band generalization of the Natori model	Full band (2D)	SCE + SDT	I_{on} at constant I_{off}	–
A. Rahman et al. [RahIEDM05]	DGFET	Si(100) Ge(100) GaAs(100) InAs(100)	Full band generalization of the Natori model	Full band (2D)	SCE + SDT	I_{on} at constant I_{off}	Ge(100) for thin EOT GaAs(100) for thick EOT
A. Pethe et al. [PetheIEDM05]	DGFET	Si(100) Ge(100) GaAs(100) InAs(100) InSb(100)	Natori model	Effective mass approximation (2D)	SCE + BBT	I_{on} at constant I_{off}	GaAs(100)
M. De Michiels et al [DeMiTED2007]	DGFET	Si(100) Si(110) Ge(110) GaAs(110)	Natori model	Effective mass approximation (2D)	–	I_{on} at constant I_{off}	Ge(110)
S.E. Laux [LauxTED2007]	UTB SOI FET	Si(100) Ge(100) GaAs(100) InGaAs(100) InP(100)	Monte Carlo approach + DESSIS	Full band (2D)	SCE + SDT + BBT	Intrinsic switching time	InGaAs
Cantley et al. [CanIEDM2007]	DGFET	Si(100) Ge(100) GaAs(100) InAs(100)	NEGF - NanoMOS	Eff. mass. extracted from tight binding calculation (2D)	SCE + SDT	I_{on} at constant I_{off}	Si(100)

Table 1.2 Sum up of the studies of the impact of alternative channel material on nano MOSFETs performances. It can be seen that no consensus has been obtained on the best channel material and its bet orientation yet

As a general remark, it is clear that no general consensus exists yet on the theoretical performance advantages of alternative channel materials for MOSFETs. More in details, this literature review has revealed the following key points in the issue of alternative channel material simulations and modeling:

- Regarding the device architecture :
  - Even if bulk devices have been sometimes considered [TakaVLSI03,FiscTED91_2], most papers are focused the deployment of alternative channel material in novel MOSFETs architectures like UTB SOI MOSFETs or Double Gate MOSFETs, following device architecture ITRS recommandations.
  - The introduction of alternative channel material is not likely to occur before the 32nm node of the High Performance (HP) roadmap, which feature a nominal gate length below 12nm. Therefore, the study of alternative channel material must be carried out in ultra scaled architecture.
- Regarding the On-state performance modelling :
  - As these devices will not be introduced before the 22 or the 16nm technological node of the ITRS, which feature gate length below 10nm, they will operate close to the ballistic limit, or more likely in the quasi-ballistic regime. Until now, however, full ballistic transport is usually assumed, as it gives a fairly good estimation of the upper limit of alternative channel material performances.
  - All satellite valleys (Δ, L or Γ) of the semiconductor must be taken into account. Indeed, it has been shown in [PethIEDM05] and [RahIEDM04] that the strong quantization occurring in the channel material featuring low quantization masses (like III-V compounds) can fill high energy states. As these satellite valleys generally have larger DOS than the first valleys, injection velocity degradation is expected [PethIEDM05], which could result in on current degradation.
  - Changing the channel material also implies to reinvestigate the optimum wafer surface and channel orientation. This issue has been first addressed partially in [TakaVSLI03]. In [LowIEDM03,LauxIEDM04,DeMiTED07], the authors have studied extensively the channel orientation of Si and Ge channels, showing that optimized channel orientation can lead to possible on state performance gain.
  - Due to strong quantum confinement in ultra thin films, the bandstructure (gaps and effective masses) of semiconductor is modified with respect to the bulk crystal one. In [RahIEDM04], A. Rahman et al. used tight binding simulation and proved that the bulk effective masses overestimated the ballistic drain current of Ge channel DGFETs. To avoid this overestimation, modified effective masses and energy bandgap fitted on full band calculation should be used, as carried out in [CantIEDM07].

  - It has been proved that the backscattering coefficient depends on the low field mobility [PaleIEDM06]. Therefore, the critical gate length at which devices will go from quasi to full ballistic current will depend on the channel material through its mobility. Channel material with high mobility will therefore surely feature full ballistic current for larger channel length. Thus, the channel backscattering coefficient should be taken into account in the simulation of alternative channel material devices to fairly compare them. This aspect has only been studied in [LauxTED07] so far.

- Regarding the off state

  - Short Channel Effects (SCEs) will differ between materials due to their various dielectric constants and energy bandgaps (impacting the intrinsic carrier concentration [LiuTED03]). These effect has been well studied in [PetheIEDM05]. However, SCEs are greatly reduced in thin films devices or DGFETs, provided that a high ratio between the gate length and the semiconductor film thickness is kept (ideally L/t_{si}=3 or higher).

  - Due to the small bandgap of some material, Band-to-Band Tunnelling (BBT) is expected to play a major role in the increase of subthreshold current. This leakage, intensively studied by the Standford group [PetheIEDM03, KrishTED2006, KimSISPAD7], is extremely complex to model accurately [LyuriSSE07]. Thus, the lack of consensus on the procedure to model BBT may be responsible of the contradictive conclusions of the literature on this topic.

  - Source-to-Drain Tunnelling (SDT) has been found to be also a major contribution of the total subthreshold leakage. In particular, small effective mass materials like Ge or III-V compounds are expected to lead to large SDT, thus reducing the performances of alternative channel material devices [CantIEDM07].

Most of the results in this topic have been obtained during the recent years. However, to our knowledge, no contribution gathers all critical points yet. To do so, the following issues must be taken into account:

1. The device orientation must be optimized
2. All relevant leakage mechanisms must be accounted for (Short Channel Effect enhancing the conventional thermionic current, SDT and BBT).
3. The impact of scattering must be investigated.

1.2.2 Aim of the thesis

The key points that have been underlined along the literature review will be addressed in this work, to give an estimation as complete as possible of the expected performances of new channel materials.

Chapter 2 will focus at first on the on state current model used in this work, giving the details of the generalization of the Natori model on which it is based. The results will then be presented.

Chapter 3 will be dedicated to the modeling of paramount subthreshold leakage mechanisms and their detrimental impact on the performances of device featuring alternative channel. The modeling of Short Channel Effects, Source-to-Drain Tunneling and Band-to-

Band Tunneling will be detailed, and benchmarked with other approaches used in the literature. The use of semi-analytical model will enable to account for all mechanisms at the same time, which is a harder task using other approaches like in the NEGF and the Monte Carlo formalisms. Indeed, NEGF includes SDT, but BBT is extremely complex to model in indirect gap materials. On the contrary, BBT can be partially taken into account in the Monte Carlo approach [FiscTED07], but not SDT (except in the case of the Wigner Transport Equation solver [QuerIEDM06]). The chosen approach will therefore allow the comparison of the respective off current contribution of the different leakage mechanisms.

Finally, in chapter 4, the Monte Carlo Multi Subband approach will be used to investigate quasi-ballistic transport in germanium channel DGFETs. The issue of Ge nMOSFETs mobility will be addressed at first. Then, the correlation of the backscattering coefficient (a high field short channel figure of merit) with effective mobility (a low field long channel one) will be studied.

In chapter 5, the conclusions of this thesis will be summerized, insisting on the original results obtained during the past three years.

Chapter 2 : Ballistic On current of nano nMOSFETs featuring arbitrarily oriented alternative channel material

Chapter 2 : Ballistic On current of arbitrary oriented alternative channel material nano nMOSFETs 33
2.1 Introduction 34
2.2 Modelling of the ballistic on state current of arbitrary oriented alternative channel DGFETs 35
2.2.1 Carrier transport in the full ballistic regime 35
2.2.2 The Natori model of full ballistic transport 36
2.2.3 Generalized Natori model 43
2.3 Impact of channel material and channel orientation on the on state performance of ultra-scaled DGFETs 51
2.3.1 Impact of channel direction in (100) and (111) substrates 51
2.3.2 Impact of channel direction in (110) substrates 53
2.3.3 Impact of the bandstructure modification in presence of strong quantization: a literature review 59
2.4 Conclusion 61

2.1 Introduction

It has been shown in the introduction of this thesis that, due to the extreme scaling of MOSFETs devices, carrier transport was no longer a close to equilibrium process, but rather a far from equilibrium one, in which ballistic carriers (i.e. non-scattered electrons or holes in the channel) are predominant. This transition in transport regime is expected to cause a reduction of the pace of the MOSFETs performance improvement. However, this slowing down can be compensated by the introduction of alternative channel material, which feature higher injection velocity and higher mobility, thus boosting the device global performance.

The purpose of the first section of this chapter is to briefly introduce the concept of ballistic transport in ultra-scaled MOSFETs and its key figures of merit. A more detailed description of ballistic transport, including a full comparison with close to the equilibrium one, is given in [FerrThesis]. Then, the original Natori model is presented and derived, summing up its strength and weaknesses in perspective of the work presented in this thesis and in the literature. Finally, the generalization of the Natori model to any channel material in any possible channel orientation is given at the end of the first section.

Using this generalized model of ballistic current, a first investigation of the impact of channel orientation on the on state current of alternative channel material Double Gate MOSFET (DGFET) is presented in the second section of this chapter. This section not only will give a better understanding of results already obtained in [LowIEDM03] and [LauxIEDM04] and but also expose a generalization of these results.

2.2 Modelling of the ballistic on state current of arbitrary oriented alternative channel DGFETs

2.2.1 Carrier transport in the full ballistic regime

Carrier transport in nanostructure can be conceptually considered as the exchange of carrier between two reservoirs separated by a controlled energy barrier.

Following this approach, Figure 2.1 schemes the fully ballistic transport in a n-type DGFET. The top figure represents the structure and the geometry of a DGFET and its associated coordinate system: the channel source-drain direction is aligned with the x axis; the width of the transistor is aligned with the y axis, and the gates stack is align with the z axis. This convention, usually referred as Device Coordinate System (DCS), will be used all along this thesis.

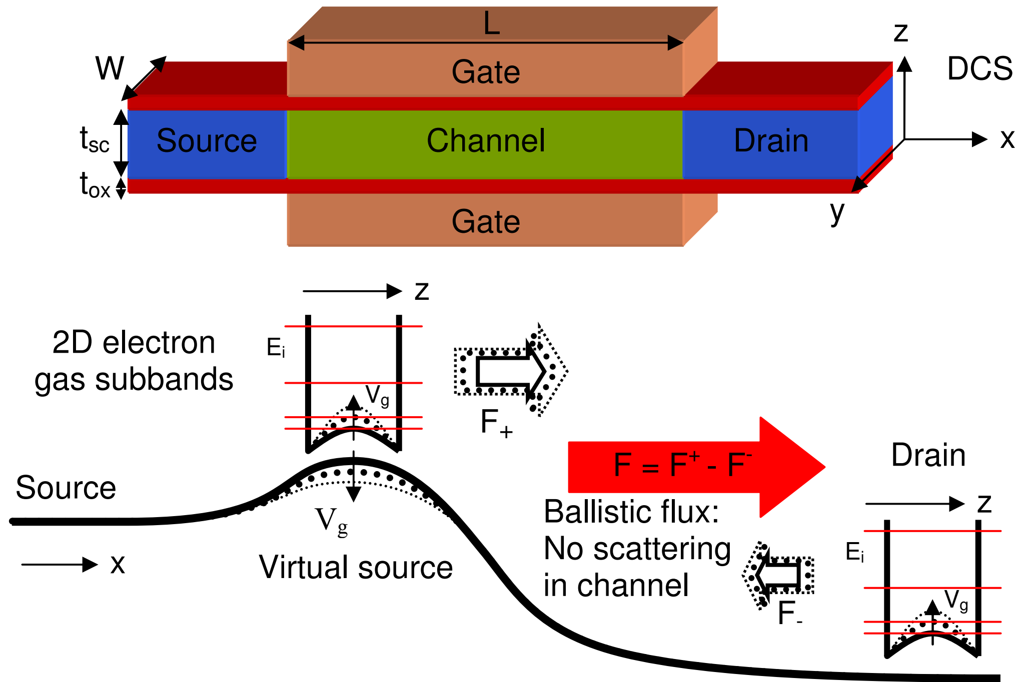

Figure 2.1 : Scheme of the full ballistic transport in a DGFET. Top figure represents the DGFET structure and its coordinate system (DCS). The bottom figure represents the source to drain potential barrier and the corresponding carrier flux emitted from the virtual source and from the drain.

The only devices studied in this thesis are N-type DGFETs, as they are known to have significantly lower Short Channel Effects at ultra-scaled dimension [FerrTNANO08], [ColiME07]. Source and drain act as electron reservoirs, which are separated by a source-drain energy barrier in the channel preventing carrier exchange, as represented in the bottom part of the figure. Using the electrostatic control of the gates, the energy barrier between source and drain can be modulated consistently with the charge in the channel. An increase of the charge in the channel lowers the barrier, which therefore allows carrier exchange between the two reservoirs.

As already mentioned, in the assumption of fully ballistic transport, and contrary to the close-to-equilibrium one, carrier scattering is totally ignored in the channel. Therefore, apart from the zone in the junction where the field opposes the movement, electrons can freely fly from the virtual source to the drain, and *vice versa*. Anyhow, and contrary to past beliefs, the transistor operation is still conserved [NatoJAP94]. The different current regime do not originates from carriers' drift and diffusion anymore, but from the differences of free carrier fluxes emitted by the source and the drain, as shown in Figure 2.1, which results in the following regime:

- If the source and drain bias are equal, the barrier is symmetrical, and the fluxes emitted by the source and the drain are equal. The current is thus zero ($F^+ = F^- \Rightarrow F = 0$, as schematized on Figure 2.1).
- If the drain bias is higher than the source bias, the flux coming from the drain side is weaker than the flux coming from the source side, which creates a positive carrier flux toward the drain ($F^+ > F^- \Rightarrow F > 0$). Increasing the drain voltage (i.e. lowering the energy on the drain side) increases at first the drain current, because of the lower counter contribution from the drain side flux ($F^- \downarrow \Rightarrow F \uparrow$). This regime is equivalent to the former linear (Ohmic[2]) regime in the sense that the current is a relatively strong function of Vd. However at a given drain voltage value, the contribution from the drain side becomes totally negligible compared to the one of the source side: the increasing further the drain voltage does not increase anymore the total drain current. The device enters in saturation regime ($F^+ >> F^- \Rightarrow F$ constant $= F^+$).
- If the gate voltage is increased and the drain voltage is high, the barrier is lowered. More electrons are consequently injected in the channel toward the drain. The total drain current therefore increases ($F^+ \uparrow \Rightarrow F \uparrow$). The device is in inversion.

Due to the small thickness of the DGFETs semiconductor film (t_{sc}), the gates and body stack creates a quantum well which confines carriers along the z axis. Consequently, the wave function associated to an electron is quantized in the z direction, but still considered as plane wave in the x and y axis. The drain currents therefore result from the difference of 2 dimensional electron gas fluxes. This quantization, present all along the channel and in the source and drain, is illustrated in Figure 2.1 by two potential wells in the z direction, one on the top of the source to drain barrier and one on the drain side.

The top of the source-drain energy barrier plays an important role in fully ballistic regime. This position in the channel is called the virtual source, as it is considered in several models and in particular the Natori one, as a *virtual electron point* where carriers are at equilibrium with the positive flux from the source and the negative flux emitted from the drain.

The next subsection will detail the Natori model and will explain the role of the virtual source, as well as the role of the injection velocity.

2.2.2 The Natori model of full ballistic transport

It has been shown in the previous subsection that ballistic transport still ensures the same current-voltage behaviour as in devices operating in close to equilibrium condition, and that 2D electron fluxes govern the drain current. The following subsection will present the

[2] Due to the absence of scattering in the channel, it is not rigorously possible to qualify this regime as "Ohmic".

formalization of the full-ballistic transport in the framework of the semi-classical Natori model [NatoJAP94].

At first, the Natori model considers source and drain as perfect electron reservoirs in equilibrium, which implies that the 2D degenerate electron gases follow a Fermi-Dirac distribution of the carrier with the energy. It assumes in addition an electron transport in a (100)/[100][3] silicon channel, whose device coordinate system is aligned with the Crystalline Coordinate System (CCS).

In addition, the Natori model is derived in the framework of the Effective Mass Approximation (EMA), in which the bandstructure is treated as several parabolic valleys. In bulk silicon, the bansdtructure in the EMA is composed of 6 equivalent Δ valleys, whose isoenergy values are represented as 6 ellipsoids, as illustrated in Figure 2.2.

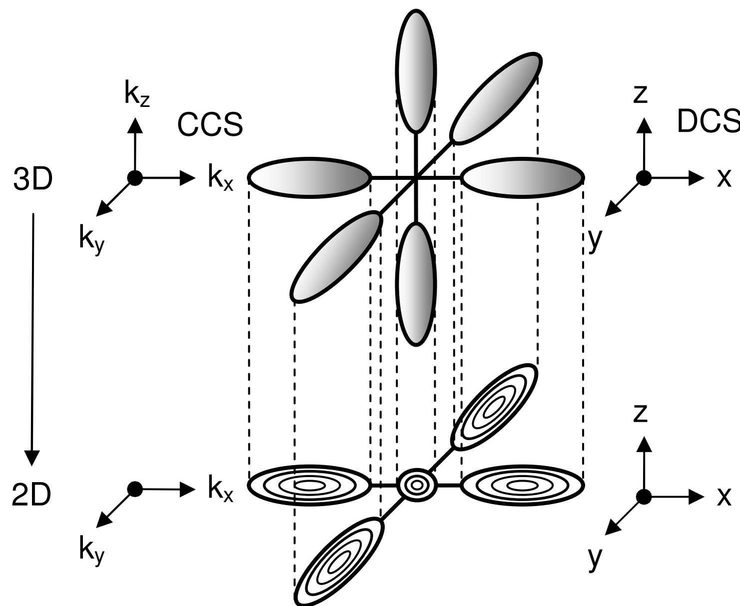

Figure 2.2 : Dispersion relation from 3D (bulk) to 2D (quantized) electron gases. In the particular case of the Natori model, the devices coordinate system (DCS) is aligned with the crystalline one (CCS) as the principal axes of the 2D ellipses are aligned with the x and y axis.

In the case of a 2D electron gas, the electron wave function loses one degree of freedom (in the z direction) and the isoenergy curves can be represented as several ellipses in the (k_x,k_y) plane, each ellipse corresponding to a different subband, as shown in Figure 2.2.

The Natori model can be obtained from the following Esaki integral [Ferry] of the current density from a single projected ellipse, neglecting at first the contribution from the drain for the sake of clarity :

[3] (confinement surface orientation)/[cristalline transport direction]

$$I_x^i = qW\sum_n \iint_{\substack{k_x>0 \\ -\infty<k_y<+\infty}} \frac{1}{\hbar}\frac{\partial E_{//}^i}{\partial k_x} f\left(E_n^i + E_{//}^i\right) T\left(E_x\right) \frac{dk_x dk_y}{2\pi^2}$$

$$\text{with } E_{//}^i = \frac{\hbar^2}{2}\left(\frac{k_x^2}{m_x^i} + \frac{k_y^2}{m_y^i}\right),\ E_x = \frac{\hbar^2}{2}\left(\frac{k_x^2}{m_x^i}\right) \text{ and } f\left(E_n^i + E_{//}^i\right) = \frac{1}{1+\exp\left(\frac{E_n^i + E_{//}^i - E_f}{k_b T}\right)} \quad (2.1)$$

In equation (2.1), q is the elementary charge, W the transistor width, ħ is the reduced Plank constant, k_x and k_y the wave vector component of the electron respectively in the x and y direction, $T(E_x)$ the transparency of the source-drain barrier at an E_x energy (energy of the carrier in the x direction) and E_f the Fermi level at the source. The n and i index respectively correspond to the index of the subband and the index of the valley considered. Thus, E_n^i is the energy of the nth subband (at the virtual source) of the ith valley with m_x^i and m_y^i its two in-plane effective masses. In this particular case, m_x^i and m_y^i are either equal to the transverse or longitudinal effective masses (resp. m_t or m_l), depending on the ellipse considered.

In (2.1), $\frac{1}{\hbar}\frac{\partial E_{//}^i}{\partial k_x}$ is the group velocity in the k_x direction of an electron whose wave vector is (k_x,k_y) with a corresponding energy $E = E_n^i + E_{//}^i = E_n^i + \frac{\hbar^2}{2}\left(\frac{k_x^2}{m_x^i} + \frac{k_y^2}{m_y^i}\right)$. The Fermi-Dirac function represents the probability of this electron to occupy an energy state E, while $T(E_x)$ corresponds to the probability for this electron to move from source to drain (in the possible presence of an energy barrier). The integrated factor in (2.1) therefore represents the electrons "density of velocity in phase space" at an energy E. The integral in phase space sums the contribution of all electrons with a positive velocity in the x direction (k_x from 0 to $+\infty$, k_y from $-\infty$ to $+\infty$) and the discrete sum over n adds the contributions from all subbands of the ellipse considered.

To obtain an analytical equation from (2.1), the following assumptions is made : Carriers are emitted by the 2D electron gas at the virtual source. Since the ground state lays above the bottom of the conduction band, $T(E_x) = 1$ for all carriers. The tunnelling contribution from the source is thus considered negligible.

Considering these assumptions, equation (2.1) becomes :

$$\begin{aligned} I_x^i &= \frac{qW\hbar}{2\pi^2 m_x^i}\sum_n \iint_{k_x>0}\left(1+\exp\left(\frac{E_n^i - E_f + E_{//}\left(k_x,k_y\right)}{k_b T}\right)\right)^{-1} k_x dk_x dk_y \\ &= \frac{q\hbar W}{2\pi^2 m_x^i}\sum_n \iint_{k_x>0}\left(1+\exp\left(\frac{E_n^i - E_f}{k_b T}\right)\exp\left(\frac{\hbar^2}{2k_b T}\left(\frac{k_x^2}{m_x^i} + \frac{k_y^2}{m_y^i}\right)\right)\right)^{-1} k_x dk_x dk_y \end{aligned} \quad (2.2)$$

The following polar variable change is then required to simplify further (2.2):

$$\begin{cases} r\cos(\theta) = \dfrac{k_x\hbar}{\sqrt{2k_bTm_x^i}} \\ r\sin(\theta) = \dfrac{k_y\hbar}{\sqrt{2k_bTm_y^i}} \end{cases} \Rightarrow \begin{cases} k_x = r\cos(\theta)\dfrac{\sqrt{2k_bTm_x^i}}{\hbar} \\ k_y = r\sin(\theta)\dfrac{\sqrt{2k_bTm_y^i}}{\hbar} \end{cases} \Rightarrow dk_xdk_y = r\frac{2k_bT\sqrt{m_x^im_y^i}}{\hbar^2}d\theta dr \quad (2.3)$$

Equation (2.2) then becomes:

$$I_x^i = \frac{qW(k_bT)^{3/2}\sqrt{2}\sqrt{m_y^i}}{\pi^2\hbar^2W}\sum_n\int_{-\frac{\pi}{2}}^{\frac{\pi}{2}}\cos(\theta)\,d\theta\int_0^\infty\left(1+\exp\left(\frac{E_n^i-E_f}{k_bT}\right)\exp\left(r^2\right)\right)^{-1}r^2dr \quad (2.4)$$

The θ integral, carried out between –π/2 and π/2 to account for only positive values of k_x, is equal to 2, while the r integral is a tabulated complete Fermi-Dirac integral :

$$\int_0^\infty\left(1+\exp\left(\frac{E_n^i-E_f}{k_bT}\right)\exp\left(r^2\right)\right)^{-1}r^2dr = \frac{1}{2}\int_0^\infty\frac{\sqrt{v}}{1+\exp(v-u)}dv = \frac{1}{2}F_{1/2}(u)$$
$$\text{with } v = r^2 \text{ and } u = \frac{E_f-E_n^i}{k_bT} \quad (2.5)$$

Finally, equation (2.4) gives :

$$I_x^i = \frac{qW(k_bT)^{3/2}\sqrt{2}\sqrt{m_y^i}}{\pi^2\hbar^2}\sum_n F_{1/2}\left(\frac{E_f-E_n^i}{k_bT}\right) \quad (2.6)$$

The total current is then obtained by summing the contribution from all silicon valleys.

The valley dependent factors in (2.6) are indexed by i. The valley dependence of the current is then accounted by the m_y^i in-plane effective mass and the E_n^i subband energy level, itself function of the confinement effective mass. Consequently, valleys are degenerated if they have the same m_y^i in-plane effective mass and the same confinement mass.

Due to confinement, the 6 Δ ellipsoids in silicon are thus part in 2 groups of 2D quantized ellipses: 2 ellipses confined with a longitudinal effective mass m_l (Δ_2) and 4 ellipses confined with a transversal effective mass m_t (Δ_4), as shown in Figure 2.2.

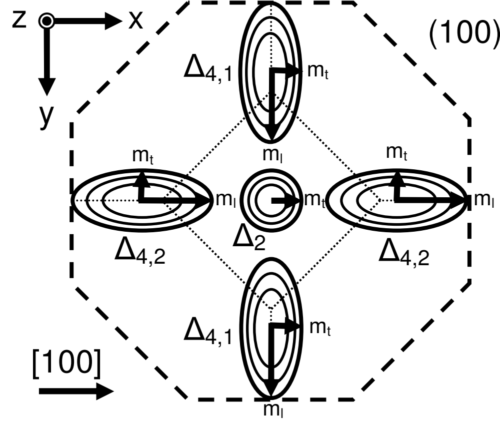

Figure 2.3 : Projection of the first Brillouin zone on a (100) surface and the 2 degenerated family of ellipses in silicon.

In addition, because of the perpendicular in-plane orientation of the Δ_4 ellipses, the current contribution from this valley originates from 2 ellipses with a longitudinal effective mass in the y direction ($\Delta_{4,1}$), and 2 with a transverse effective mass in the y direction ($\Delta_{4,2}$), as shown in Figure 2.3.

The total current is therefore:

$$I_x = 2\frac{qW(k_bT)^{3/2}\sqrt{2}}{\pi^2\hbar^2}\left(\underbrace{\sum_n \sqrt{m_t}F_{1/2}\left(\frac{E_f - E_n^l}{k_bT}\right)}_{\Delta_2} + \underbrace{\sum_n \sqrt{m_l}F_{1/2}\left(\frac{E_f - E_n^t}{k_bT}\right)}_{\Delta_{4,1}} + \underbrace{\sum_n \sqrt{m_t}F_{1/2}\left(\frac{E_f - E_n^t}{k_bT}\right)}_{\Delta_{4,2}}\right) \quad (2.7),$$

with E_n^l and E_n^t the respective subband levels from an ellipse confined with a longitudinal effective mass (Δ_2) and from an ellipse confined with a transverse effective mass (Δ_4).

The derivation of these equations is the same if the drain contribution has to be taken into account. The only change lies in the "Fermi-Dirac supply functions" and equation (2.7) becomes:

$$\begin{aligned}
I_x = {} & 2\frac{qW(k_bT)^{3/2}\sqrt{2}}{\pi^2\hbar^2}\left(\sum_n \sqrt{m_t}\left(F_{1/2}\left(\frac{E_f - E_n^l}{k_bT}\right) - F_{1/2}\left(\frac{E_f - E_n^l - qV_d}{k_bT}\right)\right)\right) && \Big\}\Delta_2 \\
& + 2\frac{qW(k_bT)^{3/2}\sqrt{2}}{\pi^2\hbar^2}\left(\sum_n \sqrt{m_l}\left(F_{1/2}\left(\frac{E_f - E_n^t}{k_bT}\right) - F_{1/2}\left(\frac{E_f - E_n^t - qV_d}{k_bT}\right)\right)\right) && \Big\}\Delta_{4,1}, \quad (2.8), \\
& + 2\frac{qW(k_bT)^{3/2}\sqrt{2}}{\pi^2\hbar^2}\left(\sum_n \sqrt{m_t}\left(F_{1/2}\left(\frac{E_f - E_n^t}{k_bT}\right) - F_{1/2}\left(\frac{E_f - E_n^t - qV_d}{k_bT}\right)\right)\right) && \Big\}\Delta_{4,2}
\end{aligned}$$

where $F_{1/2}\left(\frac{E_f - E_n^t - qV_d}{k_b T}\right)$ represents the contribution from the drain side. If V_d is sufficiently large, $F_{1/2}\left(\frac{E_f - E_n^t - qV_d}{k_b T}\right)$ becomes negligible compared to $F_{1/2}\left(\frac{E_f - E_n^t}{k_b T}\right)$ and the device enters the saturation regime.

As the Natori model assumes that the charge at the virtual source is fully controlled by the gate and not influenced by the drain, which is contradictory to short channel effects conditions. In addition, as this model is based on flux theory, the charge at the virtual source can be expressed as :

$$
\begin{aligned}
Q_{inv}^{VS}\left(V_d = 0V\right) &= q\frac{kbT}{\pi\hbar^2}\sum_i \sqrt{m_t m_l}\left(\left(\underbrace{F_0\left(\frac{E_{f_s} - E_n}{k_b T}\right)}_{\rightarrow N_{\Delta_4}^+} - \underbrace{F_0\left(\frac{E_{f_s} - E_n - qV_d}{k_b T}\right)}_{\rightarrow N_{\Delta_4}^-}\right)\right)\Bigg\}\Delta_{4,1} \text{ and } \Delta_{4,2} \\
&+ q\frac{kbT}{2\pi\hbar^2}\sum_i m_t\left(\underbrace{F_0\left(\frac{E_{f_s} - E_n}{k_b T}\right)}_{\rightarrow N_{\Delta_2}^+} - \underbrace{F_0\left(\frac{E_{f_s} - E_n - qV_d}{k_b T}\right)}_{\rightarrow N_{\Delta_2}^-}\right)\Bigg\}\Delta_2 \\
&= q\left(N^+\left(V_g\right) + N^-\left(V_g, V_d\right)\right)
\end{aligned}
\tag{2.9}
$$

where Q_{inv}^{VS} is the inversion charge at the virtual source obtained by 1D Poisson-Schrödinger calculation, q the elementary charge, N^+ and N^- are respectively the carrier density with a wave vector oriented in the positive and the negative direction, at the virtual source (i.e. respectively $k_x > 0$ or $k_x < 0$). In (2.9), F_0 is defined as :

$$F_0(\eta) = \int_0^{\infty} \frac{du}{1 + e^{u-\eta}} = \ln(1 + e^{u-\eta}) \tag{2.10}$$

According to (2.9), if V_d is increased, the contribution of N^- is progressively decreased, which globally reduces Q_{inv}^{VS} (less contribution to the charge from the drain side in (2.9)). To maintain Q_{inv}^{VS} constant as in a properly scaled devices (no short channel effect), a shift on V_d is introduced following:

$$Q_{inv}^{VS}\left(V_d = 0V\right) = q\left(N^+\left(V_g\right) + N^-\left(V_g, V_d + \Delta\right)\right) \tag{2.11}$$

The shift Δ is then numerically determined to verify (2.11). This procedure is described in detail in [FerrTNano07], [NatoJAP94], [AssaTED00].

The importance of the injection velocity has been underlined in the introduction of this thesis. In the Natori model, the injection velocity is defined as:

$$V_{inj}(x_s) = \frac{I_x^+(x_s)}{q \cdot N^+(x_s)} \tag{2.12}$$

In (2.12), N^+ is the carrier density of a 2D electron gas with a velocity oriented in the positive x value, and x_s is the position of the virtual source in the channel. The injection velocity can be expressed as :

$$V_{inj} = \frac{2\sqrt{2}(k_bT)}{\pi^2} \frac{\sum_i \sum_n \sqrt{m_y^i} F_{1/2}\left(\frac{E_f - E_n^i}{k_bT}\right)}{\sum_i \sum_n \sqrt{m_x^i}\sqrt{m_y^i} F_0\left(\frac{E_f - E_n^i}{k_bT}\right)} \tag{2.13}$$

This equation can be extended to display the contribution of all valleys to the total injection velocity of silicon:

$$\begin{aligned} V_{inj} = & \left.\frac{2\sqrt{2}(k_bT)}{\pi^2} \frac{\sum_n \sqrt{m_t}\sqrt{m_t} F_0\left(\frac{E_f - E_n^l}{k_bT}\right)}{\sum_i \sum_n \sqrt{m_x^i}\sqrt{m_y^i} F_0\left(\frac{E_f - E_n^i}{k_bT}\right)} \frac{\sum_n \sqrt{m_t} F_{1/2}\left(\frac{E_f - E_n^l}{k_bT}\right)}{\sum_n \sqrt{m_t}\sqrt{m_t} F_0\left(\frac{E_f - E_n^l}{k_bT}\right)}\right\}\Delta_2 \\ & \left. + \frac{2\sqrt{2}(k_bT)}{\pi^2} \frac{\sum_n \sqrt{m_t}\sqrt{m_l} F_0\left(\frac{E_f - E_n^t}{k_bT}\right)}{\sum_i \sum_n \sqrt{m_x^i}\sqrt{m_y^i} F_0\left(\frac{E_f - E_n^i}{k_bT}\right)} \frac{\sum_n \sqrt{m_l} F_{1/2}\left(\frac{E_f - E_n^t}{k_bT}\right)}{\sum_n \sqrt{m_t}\sqrt{m_l} F_0\left(\frac{E_f - E_n^t}{k_bT}\right)}\right\}\Delta_{4,1} \\ & \left. + \frac{2\sqrt{2}(k_bT)}{\pi^2} \frac{\sum_n \sqrt{m_t}\sqrt{m_l} F_0\left(\frac{E_f - E_n^t}{k_bT}\right)}{\sum_i \sum_n \sqrt{m_x^i}\sqrt{m_y^i} F_0\left(\frac{E_f - E_n^i}{k_bT}\right)} \frac{\sum_n \sqrt{m_t} F_{1/2}\left(\frac{E_f - E_n^t}{k_bT}\right)}{\sum_n \sqrt{m_t}\sqrt{m_l} F_0\left(\frac{E_f - E_n^t}{k_bT}\right)}\right\}\Delta_{4,2} \end{aligned} \tag{2.14};$$

which can be written as :

$$V_{inj} = \frac{N_{\Delta_2}^+}{N^+} V_{inj}^{\Delta_2} + \frac{N_{\Delta_{4,1}}^+}{N^+} V_{inj}^{\Delta_{4,1}} + \frac{N_{\Delta_{4,2}}^+}{N^+} V_{inj}^{\Delta_{4,2}} \tag{2.15},$$

where $V_{inj}^{\Delta 2}$, $V_{inj}^{\Delta 4,1}$ and $V_{inj}^{\Delta 4,2}$ are the respective injection velocity of the Δ_2, $\Delta_{4,1}$ and $\Delta_{4,2}$ valleys.

Equation (2.15) therefore shows that the total injection velocity is the average of the injection velocity of each valley weighted by their relative occupancy.

Equations (2.8) and (2.13) illustrate the simplicity of the Natori model of ballistic current. It however requires the calculation of the subband energy levels E_n^i and the Fermi-Dirac integral. The subband structure can easily be obtained by analytical models like the one

presented in [GeTED02] or [FerrJJAP06], or with more rigorous one dimensional Poisson-Schrödinger simulations (as carried out in this work).

The Poisson Schrödinger code simply consists in solving the coupled 1D differential equations of Schrödinger (eigenvalues problem to find the energy levels of each different valleys) and the Poisson equation (matrix inversion). This coupling constitutes the only difficulty to the numerical solution of this quantum problem. To overcome it, an over-relaxation approach has been initially suggested by Stern [SterJCP70], but it is commonly accepted nowadays that the Newton-Raphson scheme (using the approximated classical Jacobian) is much more numerically efficient [Berkley].

The Fermi-Dirac integrals are also calculated numerically, but it can be also approximated with known approaches if the electron gas is degenerated or not (respectively the Thomas-Fermi approximation if $E_f << E_n$ and the Boltzmann approximation for $E_f >> E_n$,).

However, several weaknesses of this model arise from this simplicity. In particular, the model is only valid for silicon channel under a (100) surface, in a [100] direction and short channel effects are neglected as well as additional subthreshold leakage currents. It thus needs to be generalized to be used in the scope of alternative-channel device performance estimation.

The following subsection describes the generalisation of the Natori model to any channel orientation and any channel material. The issue of source-drain tunnelling leakage current will be addressed in chapter 3.

2.2.3 Generalized Natori model

Generalizing the Natori model requires to re-write the formalism presented in the previous subsection carefully accounting for the drain current parameter dependence with the channel material and orientation. In this framework, it appears that the channel material and orientation dependence is fully taken into account using more general and relevant transport and confinement effective masses.

At first, to model alternative channel material, all valleys of the semiconductor must be taken into account, and not only the 6 fold Δ ones like in the case of silicon. Any bandstructure treated in the EMA of a semiconductor of the zinc-blend or diamond lattice structure, including silicon, consists in fact of 11 valleys :

- 6 ellipsoidal Δ valleys aligned on the 6 equivalent [100] axis of the first Brillouin zone in phase space (X direction);
- 8 halves (or 4 full) ellipsoidal Λ valleys aligned on the 8 equivalent [111] axis of the first Brillouin zone in phase space (L direction);
- 1 Γ spherical valley ($m_x = m_y = m_z = m_t$), at the centre of the first Brillouin zone.

Figure 2.4 shows the X, L and Γ points of the first Brillouin zone of a zinc-blend or diamond lattice structure (face-center cubic) material, like Si, Ge, GaAs InAs and most of the common semiconductors.

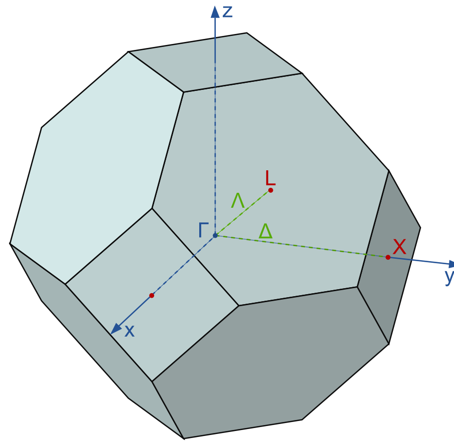

Figure 2.4 : Scheme of the first Brillouin zone, showing the 6 equivalent X direction (100), the 8 equivalent L direction (111) and the central Γ point. The Δ and Λ valleys are respectively located on the X and L direction.

Figure 2.5 shows a 2D projection of the silicon bandstructure on the X and L direction, showing the gaps bewteen Δ, Λ and Γ.

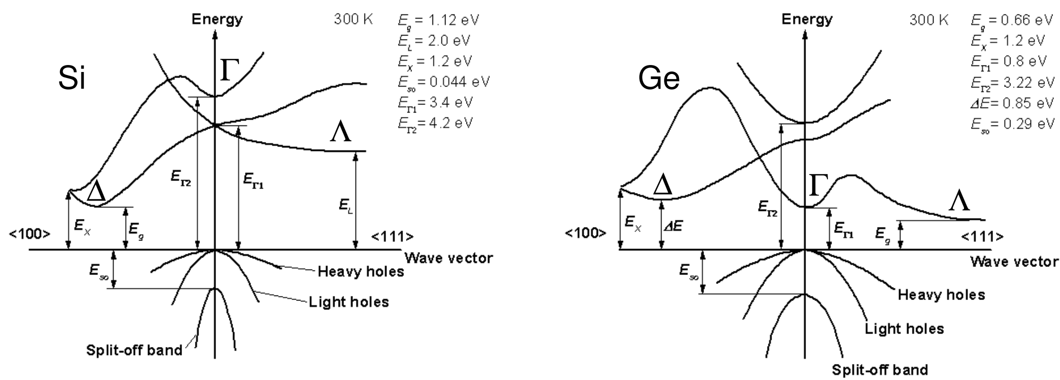

Figure 2.5 : Bandstructure of silicon (left) and germanium (right), showing the Δ, Λ and Γ valleys of these materials. It can be seen that Si also features Λ and Γ valleys. However the impact of these valleys is negligible as their energy are very high. (Taken from [Ioffe.ru])

Table 2.1 presents the longitudinal (m_l) and transverse (m_t) effective masses and energy gaps of the Δ, Λ and Γ valleys for relevant semiconductors considered in this work.

The ballistic current of an alternative channel material device is thus the sum over the current contributions from all these additional valleys.

In the case of a silicon channel, it has been shown in (2.7) that the current contribution of 6 Δ valleys of silicon could be reduced to the contribution of 3 ellipses degenerated twice, due to the confinement and the transport direction considered (respectively (100) and [100]). The degeneracy of the Δ and Λ valleys in the case of an alternative channel material therefore, depends on the surface and transport orientation of the channel.

	Δ Valley			Λ Valley			Γ Valley	
	m_L (m_0)	m_T (m_0)	ΔE_g (eV)	m_L (m_0)	m_T (m_0)	Gap (eV)	m (m_0)	ΔE_g (eV)
Si	0.92	0.19	0	–	–	–	–	–
Ge	0.95	0.2	0.19	1.64	0.08	0	–	–
GaAs	1.9	0.19	0.48	1.538	0.127	0.29	0.067	0
InAs	1.126	0.175	1.02	1.565	0.124	0.72	0.023	0
InSb	1.126	0.175	0.83	1.565	0.124	0.51	0.014	0
AlAs	0.813	0.223	0	1.386	0.148	0.033	0.149	0.72
InP	1.321	0.273	1.42	1.872	0.153	0.83	0.082	0
GaP	1.993	0.250	0	1.493	0.142	0.415	0.126	0.50

Table 2.1 : Effective masses and gaps of the X, L and Γ valleys for Si, Ge, GaAs, InAs, InSb, AlAs, InP et GaP. The data for Si and Ge are taken from [Ioffe.ru] as there is a large consensus on the parameters of these materials. However, for GaAs, AlAs, InP, and GaP, the data gathered in [FiscTED91_1] have been used. As InAs and InSb are not studied in the previous reference, their effective masses have been taken from [PethIEDM05]

Figure 2.6 represents the projection of the first Brillouin zone on (100), (110) and (111) surface. This figure is equivalent to Figure 2.3, but Figure 2.6 illustrates the case for an arbitrary semiconductor of the zinc-blend or diamond lattice.

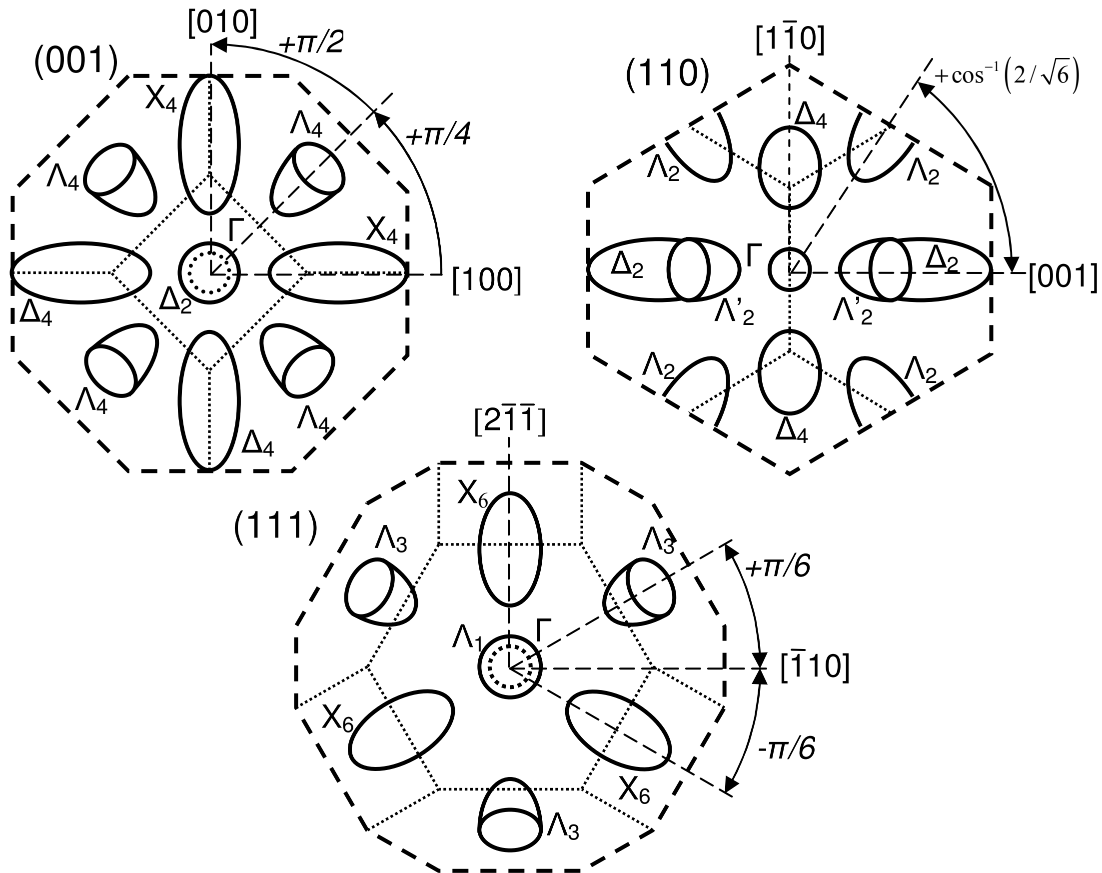

Figure 2.6 : Projection of the first Brillouin zone on (100), (110) and (111) including the angle between the crystalline reference ([010] for (100), [001] for (110) and for (111)) and the longitudinal principal axis of the recasted ellipsoid from the X, L and Γ valleys. This figure shows the 2D ellipses of the Δ, Λ and Γ valleys resulting from the quantization on these surfaces and their degeneracy due to confinement only. The degeneracy due to transport is hence ignored.

Due to the misalignment of the device coordinate system and the ellipse principal axis, or the misalignment of the device coordinate system and the crystalline one, the quantization and in-plane effective masses of the ellipses shown in Figure 2.6 are not equal to the transverse or longitudinal effective masses of the 3D ellipsoids. Figure 2.7 shows the projection of an arbitrary ellipsoid on a surface, showing how the difference between the projected in-plane effective mass m_1 and m_2 and the transverse and longitudinal effective mass of the 3D ellipsoid. In [SternPhysRev67], Stern and Howard derived the relations between the in-plane and quantization effective masses and the longitudinal and transversal effective masses. These results are summarized in Table 2.2.

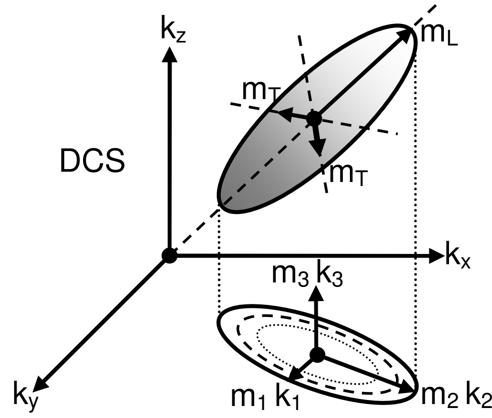

Figure 2.7 : Recasted effective masses in the device coordinate system. m_T and m_L are aligned with the principal axis of the ellipsoid while m_1 and m_2 are aligned with the principal axis of the projected ellipse on the surface. m_3 is normal to the surface (confinement direction)

	Δ					Λ				
Surface orientation	Valley	m_l	m_2	m_3	n_v	Valley	m_l	m_2	m_3	n_v
(100)	Δ_2	m_t	m_t	m_l	2	Λ_4	m_t	$\frac{m_t+2m_l}{3}$	$\frac{3m_tm_l}{m_t+2m_l}$	4
	Δ_4	m_t	m_l	m_t	4					
(110)	Δ_4	m_t	$\frac{m_t+m_l}{2}$	$\frac{2m_tm_l}{m_t+m_l}$	4	Λ_2	m_t	m_l	m_t	2
	Δ_2	m_t	m_l	m_t	2	Λ_2'	m_t	$\frac{m_l+2m_t}{3}$	$\frac{3m_tm_l}{m_l+2m_t}$	2
(111)	Δ_6	m_t	$\frac{m_t+2m_l}{3}$	$\frac{3m_tm_l}{m_t+2m_l}$	6	Λ_1	m_t	m_t	m_l	1
						Λ_3	m_t	$\frac{m_t+8m_l}{9}$	$\frac{9m_tm_l}{m_t+8m_l}$	3

Table 2.2 : In-plane (m_1,m_2) and quantization (m_3) effective masses as a function of the transverse and longitudinal effective masses of the Δ, Λ and Γ valleys on a (100), (110) and (111) surface. n_v denotes the degeneracy of the ellipses regarding confinement only.

Using these effective masses, the generalized formalization of the Natori model is obtained considering at first the current from an arbitrary oriented ellipse, as shown in Figure 2.8.

Conventionally, k_1 is always aligned in the small principal axis of the ellipse. Therefore, m_1 is always the smallest effective mass of the ellipse, and, as given in Table 2.2, always equal to m_t (due to geometrical properties of a projected ellipsoid on a surface).

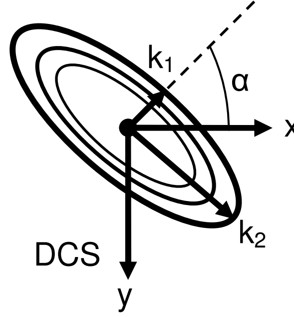

Figure 2.8 : Arbitrary oriented ellipse with respect to the device coordinated system. The α angle represent the misalignment of the small principal axis of the ellipse (k_1) with the source drain direction of the device.

As in the silicon case, the starting equation is also an Esaki formula of the current from a single ellipse :

$$I_x^{i+} = qW\sum_n \iint_{k_x>0} \frac{1}{\hbar}\frac{\partial E_{//}^i}{\partial k_x} f\left(E_n^i + E_{//}^i\right) T\left(E_x\right) \frac{dk_x dk_y}{2\pi^2} \tag{2.16}$$

But in the case of a misaligned ellipse with respect to the device coordinate system, the dispersion relation becomes [SterPhysRev67],[RahmJAP05]:

$$E_{//}^i = \frac{\hbar^2}{2}\left(\frac{k_x^2}{m_x^i} + \frac{k_y^2}{m_y^i} + \frac{2k_x k_y}{m_{xy}^i}\right) = \frac{\hbar^2}{2}\left(\frac{k_1^2}{m_1^i} + \frac{k_2^2}{m_2^i}\right) \tag{2.17}$$

In (2.17), m_x, m_y and m_{xy} are the in-plane component of the effective mass tensor in the DCS, as explained in [SterPhysRev67],[RahmJAP05], and where m_1 and m_2 are the in-plane recasted effective masses given in [SterPhysRev67], in the CCS.

Equation (2.17) shows that the E(k) relation is only parabolic in the ($\mathbf{k_1}$,$\mathbf{k_2}$) coordinate system, while cross term are present in the ($\mathbf{k_x}$,$\mathbf{k_y}$) one. As the integration of equation (2.16) is only possible in the absence of cross term like the $k_x k_y$ one, k_x and k_y must therefore be expressed as a function of k_1 and k_2 through this variable change:

$$\begin{cases} k_x = \cos(\alpha)\, k_1 + \sin(\alpha)\, k_2 \\ k_y = -\sin(\alpha)\, k_1 + \cos(\alpha)\, k_2 \end{cases}$$
$$\Downarrow \tag{2.18}$$
$$dk_x dk_y = dk_1 dk_2 \text{ and } \frac{1}{\hbar}\frac{\partial E_{//}^i}{\partial k_x} = \hbar\left(\frac{k_1}{m_1^i}\cos\left(\alpha\right) + \frac{k_2}{m_2^i}\sin\left(\alpha\right)\right)$$

where α is the angle between the channel direction and the small principal axis of the ellipse, as shown in Figure 2.8.

By replacing (2.17) and (2.18) in (2.16), and considering the same assumption as in the silicon case (top of the barrier model, absence of source-to-drain tunnelling – see 2.2.2) and after straightforward calculations, the following drain current equations are obtained :

$$I_x^{i+} = I_1^{i+} + I_2^{i+} \tag{2.19}$$

$$I_1^{i+} = \sum_n \frac{qW\hbar\cos(\alpha)}{2\pi^2 m_1^i} \iint \left(1+\exp\left(\frac{E_n^i - E_f + E_{//}(k_1,k_2)}{k_b T}\right)\right)^{-1} k_1 dk_1 dk_2 \tag{2.20}$$

$$I_2^{i+} = \sum_n \frac{qW\hbar\sin(\alpha)}{2\pi^2 m_1^i} \iint \left(1+\exp\left(\frac{E_n^i - E_f + E_{//}(k_1,k_2)}{k_b T}\right)\right)^{-1} k_2 dk_1 dk_2 \tag{2.21}$$

As carried out in the silicon case, the integral can be simplified using a polar variable change:

$$\begin{cases} r\cos(\theta) = \dfrac{k_1\hbar}{\sqrt{2k_b T m_1^i}} \\ r\sin(\theta) = \dfrac{k_2\hbar}{\sqrt{2k_b T m_2^i}} \end{cases} \Rightarrow \begin{cases} k_1 = r\cos(\theta)\dfrac{\sqrt{2k_b T m_1^i}}{\hbar} \\ k_2 = r\sin(\theta)\dfrac{\sqrt{2k_b T m_2^i}}{\hbar} \end{cases} \Rightarrow dk_1 dk_2 = \frac{2k_b T\sqrt{m_1^i m_2^i}}{\hbar^2} r dr d\theta \tag{2.22}$$

which leads to :

$$I_1^{i+} = \sum_n \frac{qW(2k_b T)}{4\pi^2\hbar^2} F_{1/2}\left(\frac{E_f - E_n^i}{k_b T}\right)\cos(\alpha)\int_{-\frac{\pi}{2}+\alpha}^{\frac{\pi}{2}+\alpha} \cos\theta \, d\theta \tag{2.23}$$

and

$$I_2^{i+} = \sum_n \frac{qW(2k_b T)}{4\pi^2\hbar^2} F_{1/2}\left(\frac{E_f - E_n^i}{k_b T}\right)\sin(\alpha)\int_{-\frac{\pi}{2}+\alpha}^{\frac{\pi}{2}+\alpha} \sin\theta \, d\theta \tag{2.24}$$

Finally, after straight forward trigonometric calculations:

$$I_x^{i+} = \sum_n \chi \cdot \sqrt{m_{j_x}^i(\alpha)} \cdot F_{1/2}\left(\frac{E_f - E_n^i}{k_b T}\right) \tag{2.25}$$

with

$$\chi = qW\frac{(2k_b T)^{3/2}}{2\pi^2\hbar^2} \tag{2.26}$$

and

$$\sqrt{m_{j_x}^i(\alpha)} = \sqrt{m_1^i}\sin^2(\alpha) + \sqrt{m_2^i}\cos^2(\alpha) \tag{2.27}$$

Equation (2.27) represents the ballistic current from a single arbitrary oriented ellipse. Knowing that m_1 is always lower than m_2, it can be deduce from equation (2.27) that the best transport direction for a single ellipse is in the perpendicular direction of the largest effective mass. In addition, equation (2.25) also shows that the in-plane orientation is only accounted for in m^i_{jx} (2.27).

The total current can then easily be obtained by summing the contribution of all the subbands of all the different minima, leading to :

$$I_x^+ = \sum_i \sum_n \chi \cdot \sqrt{m_{j_x}^i \left(\alpha - \alpha_0^i\right)} \cdot F_{1/2}\left(\frac{E_f - E_n^i}{k_b T}\right) \tag{2.28}$$

In (2.28), α_0^i is the angle between a reference direction and the ith ellipse. This shift is needed to introduce a common crystalline reference direction to all ellipses. Figure 2.6 shows some of the non-trivial angles with respect to the common crystalline reference, which are [010] for (100), [001] for (110) and [110] for (111). The α angle is thus the in-plane angle between the source-drain direction and these reference axis.

E_n^i in equation (2.28) are the subband energy levels which are function of the m_3 quantization effective mass. These subbands are computed in this work using Poisson Schrödinger self consistent simulations, generalized to different orientation according the procedure described in [SterPhysRev67], and accounting for the wave function penetration through the gate dielectrics.

The generalized equation of the injection velocity therefore becomes :

$$V_{inj}\left(\alpha\right) = \frac{I_x^+\left(\alpha\right)}{q \cdot N^+} \tag{2.29}$$

Simple calculation shows that N^+ is not dependent of the in-plane orientation of the device. However, as N^+ is a function of the subband level (see equation (2.13)), it consequently depends on the surface orientation through the quantization effective mass m_3.

Equation (2.29) can also be expended to show the contribution of each ellipse to the total injection velocity, like in equation (2.15) :

$$V_{inj}\left(\alpha\right) = \sum_i \frac{N_i^+}{q \cdot N^+} V_{inj}^i\left(\alpha\right) \tag{2.30}$$

In equation (2.30), V_{inj}^i is the injection velocity of the ith ellipse and n_i^+ its carrier density.

It has to be noticed that such a model has also been derived in [DeMiTED07].

As discussed in detail in [FerrTNANO07] but only in the case of (100) Silicon, it is clear from equations (2.28) and (2.29) that ballistic current can be enhanced by :

- Improving the mass terms in (2.27) ;
- Increasing the E_n^i – E_f difference, by enhancing the occupancy of subbands with a light transport mass.

For this purpose, the strength of quantum confinement, the value of the quantization effective mass and the subband density of states are particularly effective in changing the E_n^i – E_f difference. Material, substrate orientation, channel direction, body thickness of the DGFET, and applied fields are thus the main parameters that can impact the ballistic current.

However, one of the main drawbacks of the Natori model and of this generalized model is their significant overestimation of the drain currents compared to what can be possibly expected from a well designed device. This discrepancy is partially due to the impact of parasitic series resistances, which degrades the drain currents obtained for ultra-scaled devices. The procedure described in Figure 2.9 is applied, to include the effect of series resistance (as carried out in chapter 3),

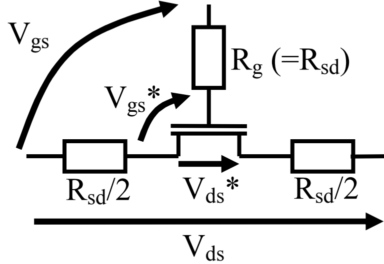

$$V_{ds} = V_{ds}^{*} + R_{sd}^{*} \cdot I_d(V_{gs}, V_{ds}) \quad (2.31)$$

$$V_{gs} = \frac{R_{sd}}{2} I_d(V_{gs}, V_{ds}) + V_{gs}^{*} \quad (2.32)$$

Figure 2.9 : Sketch of an intrinsic transistor and the parasitic resistances on the gate, source and drain terminals. Equation (2.31) and (2.32) are the voltage and current equation of this circuit.

The applied voltages are functions of the intrinsic voltage applied to the intrinsic transistor, of the parasitic resistances, and of the drain current. Assuming that the devices is in saturation (I_d independent of V_d) lead to neglect equation (2.31). Consequently, the evaluation of the effect of series resistances consists in finding the intrinsic source to gate voltage which verifies (2.32). The corresponding value of drain current obtained for this V_{gs}^{*} gives the value of the drain current including the effect of the parasitic resistances.

The next sections therefore aims to discuss in more details the complex role of material, surface orientation and channel direction employing the model which has been described. Thanks to its relative simplicity, and contrary to more exact time consuming numerical simulations, the generalized semi-analytical Natori approach presented here allows a fast evaluation of performances of a broad variety of devices and options.

2.3 Impact of channel material and channel orientation on the on state performance of ultra-scaled DGFETs

In this section, the generalized Natori model previously presented will be used to investigate the impact of channel material and orientation on the ballistic on state current of DGFETs.

In [LowIEDM03] and [LauxIEDM04], it has been deduced, by time consuming numerical simulations, that the ballistic drain current, and injection velocity on Ge Double Gate nMOSFETs (DGFETs) was isotropic on (100) and (111) surfaces and anisotropic for (110) surfaces. In addition, it has been shown that the best drain current was obtained in this anisotropic case, i.e. for a (110) substrate surface, with a channel oriented in the [110] direction.

However, these results have not been understood in its detail and the impact of channel orientations in other alternative materials has not been investigated so far. The use of semi-analytical modelling instead of numerical simulation will not only help to have a better understanding of this issue, but also to generalize these results to other materials.

Using the generalized model, the current on (100) and (111) surface will be shown to be isotropic in the first subsection, while the second subsection will study the drain current anisotropy on the (110) surface. Finally, a third subsection will present a literature review of the impact of the bandstructure modification in strongly quantized structures. Most of results presented in this section have been published in [RafhSSE08].

2.3.1 Impact of channel direction in (100) and (111) substrates

In this subsection, the impact of the in-plane orientation of (100) and (111) DGFETs (100) on the ballistic drain current is investigated. Figure 2.10 schemes the orientation convention used in this work. The considered source-drain direction is included in the (100) or (111) surface, and form an angle α with the reference crystalline direction, which are respectively the [100] and the [110] axis.

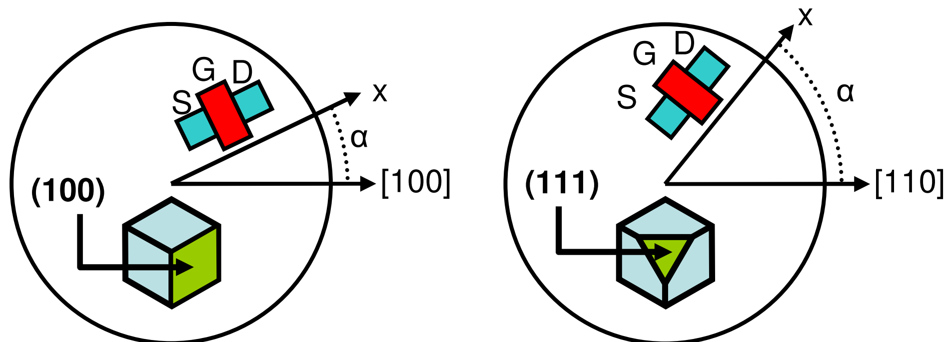

Figure 2.10 : In-plane device orientation on the (100) and (111) surfaces showing the angle between the crystalline reference (resp. [100] and [110]) and the source-drain transport direction of the device.

The dependence of currents (and corresponding injection velocity) on the in-plane orientation of the channel is explicitly contained in equation (2.28) through the mass factor (2.27). This explicit mass dependence enables an analytical evidence of the current isotropy of the (100) and (111), not only in the case of Ge devices, but in the case of any semiconductor featuring a zinc-blende crystallin lattice.

At first, regarding the (100) surface, the drain current is the sum of the Δ_2, Δ_4, Λ_4 and Γ valleys as shown in Figure 2.6. The Δ_2 and Γ contributions are isotropic as these valleys have an isotropic shape ($m_l = m_2$, as shown in Figure 2.6). The Δ_4 and Λ_4 valley are perpendicular or opposed valleys to each other. According to equations (2.25) and (2.27), it is obvious that opposite ellipsoids have the same orientation dependence of carrier injection. Then, according to (2.28), the contribution from opposed and perpendicular valleys is given by :

$$\begin{aligned} I_x^{+\Delta_4} &= 2\chi\left(\sqrt{m_1^{\Delta_4}}\sin^2(\alpha)+\sqrt{m_2^{\Delta_4}}\cos^2(\alpha)\right)\sum_n F_{1/2}\left(\frac{E_f-E_n^i}{k_bT}\right) \\ &+2\chi\left(\sqrt{m_1^{\Delta_4}}\sin^2\left(\alpha+\frac{\pi}{2}\right)+\sqrt{m_2^{\Delta_4}}\cos^2\left(\alpha+\frac{\pi}{2}\right)\right)\sum_n F_{1/2}\left(\frac{E_f-E_n^i}{k_bT}\right) \end{aligned} \quad (2.33)$$

Or

$$\begin{aligned} I_x^{+\Lambda_4} &= 2\chi\left(\sqrt{m_1^{\Lambda_4}}\sin^2(\alpha)+\sqrt{m_2^{\Lambda_4}}\cos^2(\alpha)\right)\sum_n F_{1/2}\left(\frac{E_f-E_n^i}{k_bT}\right) \\ &+2\chi\left(\sqrt{m_1^{\Lambda_4}}\sin^2\left(\alpha+\frac{\pi}{2}\right)+\sqrt{m_2^{\Lambda_4}}\cos^2\left(\alpha+\frac{\pi}{2}\right)\right)\sum_n F_{1/2}\left(\frac{E_f-E_n^i}{k_bT}\right) \end{aligned} \quad (2.34)$$

As the perpendicular ellipses have the same confinement mass m_3, the subband level energies are the same and the two $F_{1/2}$ factors are equal. Trivial trigonometric calculations show that adding these two perpendicular ellipses, as done in equation (2.33) and (2.34), cancel out the dependence with α, which implies that the injection from two perpendicular ellipses is isotropic. Therefore, the total current is isotropic on (100) surfaces, since the contributions of the X_2, Γ, Δ_4 and Λ_4 valleys are all isotropic.

Same calculations show that the sum of the contribution to the current from the three Δ_3 ellipses and from the three Λ_3 ones, both separated by a π/3 angle on the (111) surface (see Figure 2.6) is also isotropic.

In addition, as these conclusions are consequences of the symmetries of the band structure of semiconductor of the zinc-blend and diamond lattices, i.e. the symmetries of the Δ, Λ and Γ valleys, the isotropy of the (100) and (111) ballistic drain current is true for all semiconductors of these lattice groups.

To illustrate this point, undoped symmetrical DGFETs on (100) and (111) surfaces with various channel materials (Si, Ge, GaAs, InAs, InSb, AlAs, InP and GaP) have been simulated. In these simulations, the body thickness t_{sc} for these DGFETs is 5 nm and the gate dielectrics Equivalent Oxide Thickness (EOT) is 1 nm.

Figure 2.11 shows the drain current at a constant inversion charge as a function of the α angle of these alternative channel material devices. The isotropy of the current versus channel direction is clearly shown on (100) and (111) substrates, which confirms the results obtained

in [LowIEDM03] and [LauxIEDM04] and the analytical demonstration carried out previously.

However, the mathematical simplifications possible under (100) and (111) surfaces are not possible for the current on a (110) surface. The contribution of the Δ_4, Δ_2, Λ_2 and Λ_2' projected ellipses on the (110) surface (see Figure 2.6) are intrinsically anisotropic and their sum does not cancel out the dependence with α. This anisotropy of the carrier injection, already reported for Ge DGFETs in [LowIEDM03] and [LauxIEDM04], is studied in more details in the next subsection, not only for Ge, but also for different III-V semiconductors of the Zinc Blend lattice structure.

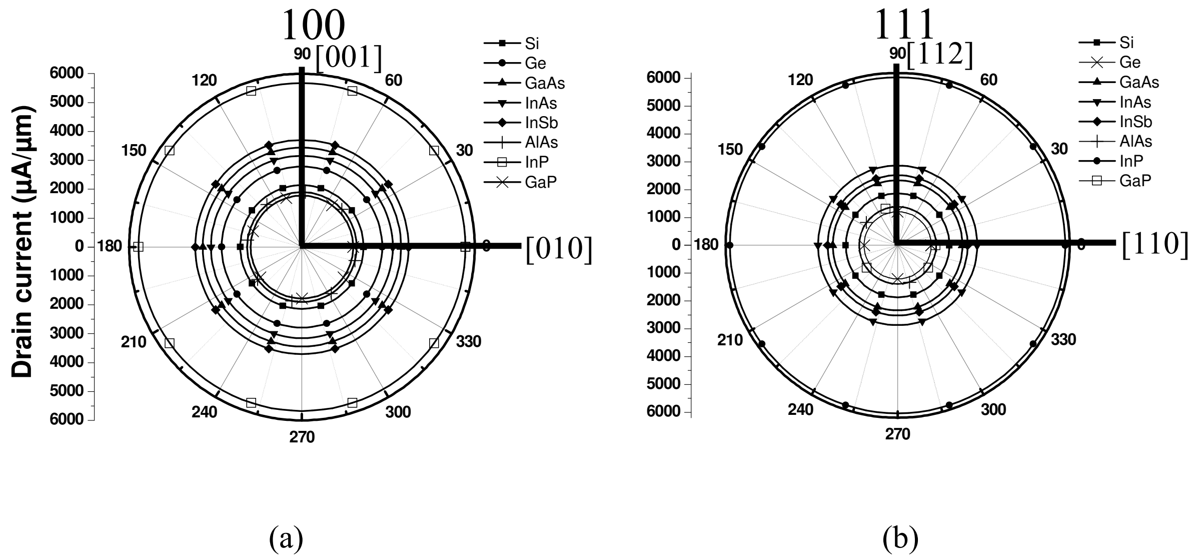

Figure 2.11 : DGFETs drain current in the fully ballistic regime as a function of the channel orientation on (100) (a) and (111) (b) surface with Si, Ge, GaAs, InAs, InSb, AlAs, InP and GaP channel material. Current are taken at a constant carrier density of $10^{13}cm^{-2}$/gate. Gate work function is chosen so that it gives a constant off current equal to 1 nA/µm. Body thickness t_{sc} for these DGFETs is 5nm and the Equivalent Oxide Thickness t_{ox} is 1 nm.

2.3.2 Impact of channel direction in (110) substrates

2.3.2.1 Semiconductors optimum channel orientations on the (110) surface

The same simulations have been carried out for the same alternative channel material DGFETs, but on the (110) surface, with an orientation convention illustrated in Figure 2.12. Figure 2.13 shows the ballistic drain current of 5 nm body DGFETs on (110) surfaces in strong inversion as a function of the α angle.

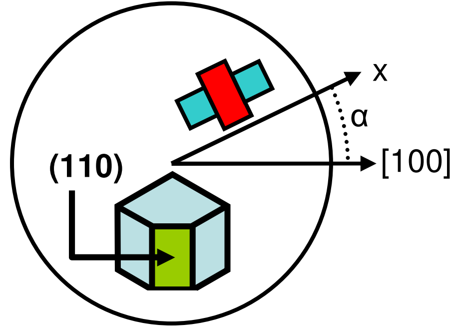

Figure 2.12 : In-plane device orientation on the (110) surface showing the angle between the crystalline reference (100) and the source-drain transport direction of the device

Among the various materials simulated, some general trends are obtained.

First of all, materials like Si, AlAs and GaP have their best ballistic current along the [001] axis (see Figure 2.13 (a)). In these materials, the first minima of the conduction band are located in Δ valleys, which always carry most of the charge, even when taking into account the occupancy of other valleys, possibly modified by quantum confinement enhancement. Consequently, on the (110) surface, the carriers are located mainly in Δ_4 valleys, thanks to a larger quantization effective mass compared to the Δ_2 valleys ($m_t < \frac{2m_t m_l}{m_t + m_l}$, see Table 2.2). As shown in Figure 2.14 (a), the Δ_4 have their largest in-plane effective mass in the [110] direction, which results in a larger current in the perpendicular direction, i.e. [100].

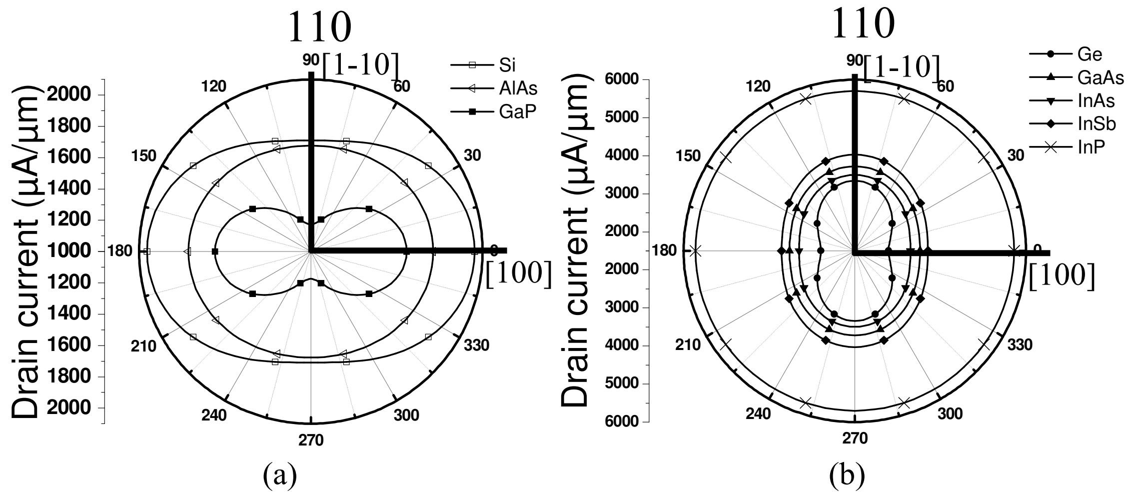

Figure 2.13 : DGFETs drain current in the fully ballistic regime as a function of the channel orientation on (110) substrate with Si, AlAs and GaP (a) and Ge, GaAs, InAs, InSb, InP channel material (b). Current are taken at a constant carrier density of 10^{13}cm^{-2}/gate. Gate work function is chosen so that it gives an I_{off} constant and equal to 1 nA/µm. Body thickness t_{sc} for these DGFETs is 5nm and the Equivalent Oxide Thickness is EOT = 1 nm.

Then, in Ge, GaAs, InAs and InSb DGFETs, the higher drain current on the (110) surface is obtained for a channel oriented in the [110] direction (see Figure 2.13(b)). This may seem surprising, as GaAs, InAs and InSb materials have their gap in Γ, an isotropic valley. However, as already shown in [PethIEDM05] for GaAs, InAs and InSb on (100) substrate,

carriers, when confined, move from the subbands of the Γ valley to the subbands of the Λ valleys because of the extremely small effective masses of the Γ valleys. A similar effect also occurs on (110) surfaces, as the charge in this case is also located in the Λ_2' valleys (higher confinement mass than Λ_2). As it can be seen from equations (2.25) to (2.27), the current is higher in the direction perpendicular to the direction of the higher in-plane mass of this valley, i.e. [110] in this case, as shown in Figure 2.14 (b).

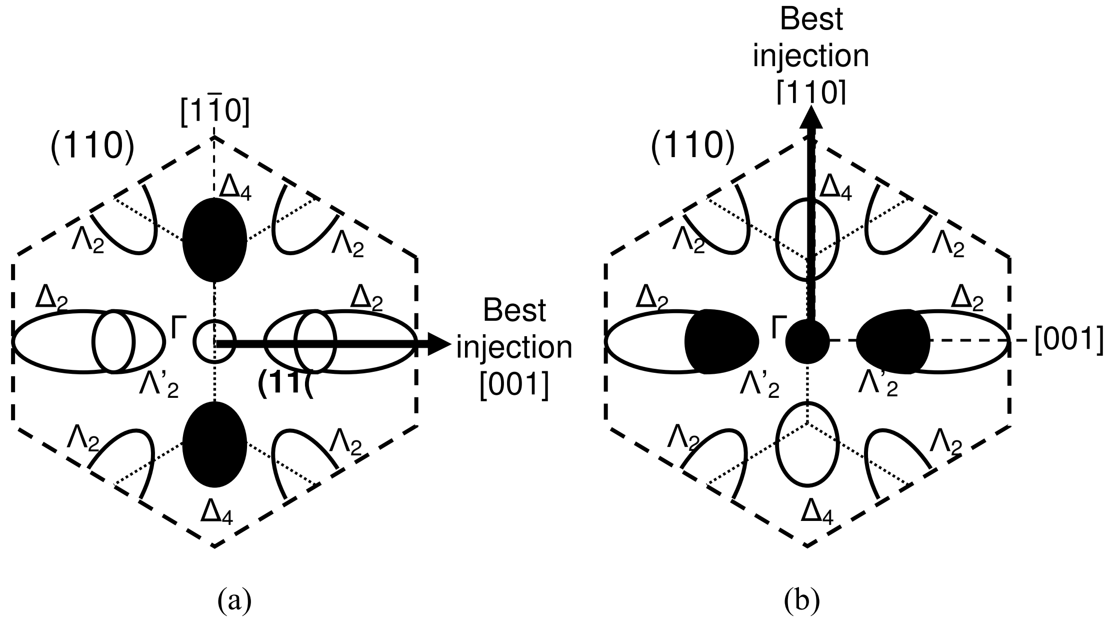

Figure 2.14 : Projection of the first Brillouin zone on a (110) surface, showing in dark the populated valleys in the case of Si, AlAs and Gap channel material (a) and Ge, GaAs, InAs, InSb channel material (b). The corresponding best current/injection directions are also shown (direction perpendicular of to the largest effective masses of most populated valleys)

Finally, InP DGFETs may appear as a particular case in Figure 2.13 (b), as the current in this device does not seems to show any anisotropy on the (110) surface. Indeed, in InP inversion layers, carriers remain mainly in the (isotropic) Γ valley because of the large gap between the Γ and the Λ valleys and the larger effective mass of the Γ valley compared to GaAs, InAs and InSb. However, the Λ valley subbands of InP can occasionally be populated if t_{sc} is further reduced and if the carrier density is increased. In these conditions, InP DGFETs will present the same anisotropic drain current as GaAs, InAs or InSb.

It can be seen on Figure 2.13 that the magnitude of currents are also very different on the (110) surface for these two class of materials. However, it can not be concluded yet that Ge, GaAs, InAs, InSb or InP are more promising channel material, since the source drain tunnelling leakages have not been included yet. This will be done in chapter 3 of this thesis

2.3.2.2 Impact of confinement on Anisotropy

The previous subsection has showed that quantum confinement and the relative subband filling play a significant role in the ballistic current anisotropy of the (110) surface. It is found

that the most occupied valleys determine the best current direction: when the Δ valleys are more occupied, the best current is in the [100] direction and when the Λ valleys are more occupied, the best current is found to be in the [100] direction.

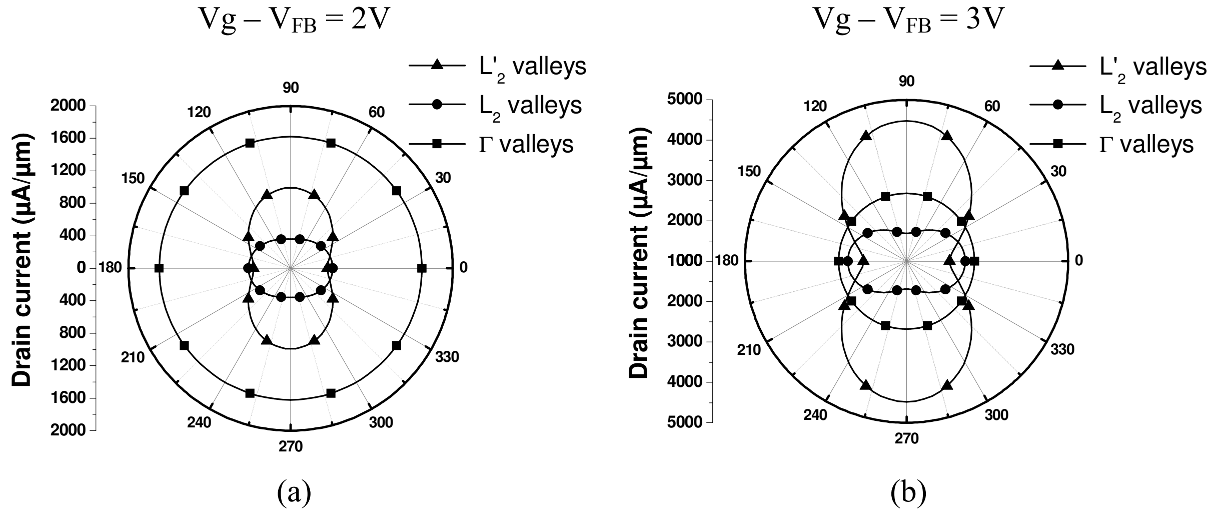

Figure 2.15 : DGFETs drain current in the fully ballistic regime as a function of the channel orientation on (110) GaAs substrate at two different gate voltages (Fig. 5 A : $Vg - V_{FB} = 2V$, Fig. 5 B : $Vg - V_{FB} = 3V$). Body thickness t_{sc} for these DGFETs is 5nm, the Equivalent Oxide Thickness (EOT) is t_{ox}=1 nm and I_{off} is 1nA/µm.

However, the other non-negligibly populated valleys will also contribute to the total current, and to the amount of anisotropy. As the occupancy of the different subbands depends both on effective mass and the confinement strength, the role of the different subbands is therefore a function of the bias conditions and body thicknesses (t_{sc}). As shown in Figure 2.16, the ground originates for $Vg-V_{FB}$ = 2 or 3V from the Γ valley. However, most of the higher subband originates form the Λ valley. As the Fermi level is higher in the case of $Vg-V_{FB}$ = 3V, these satellite valleys contribute more to the total current.

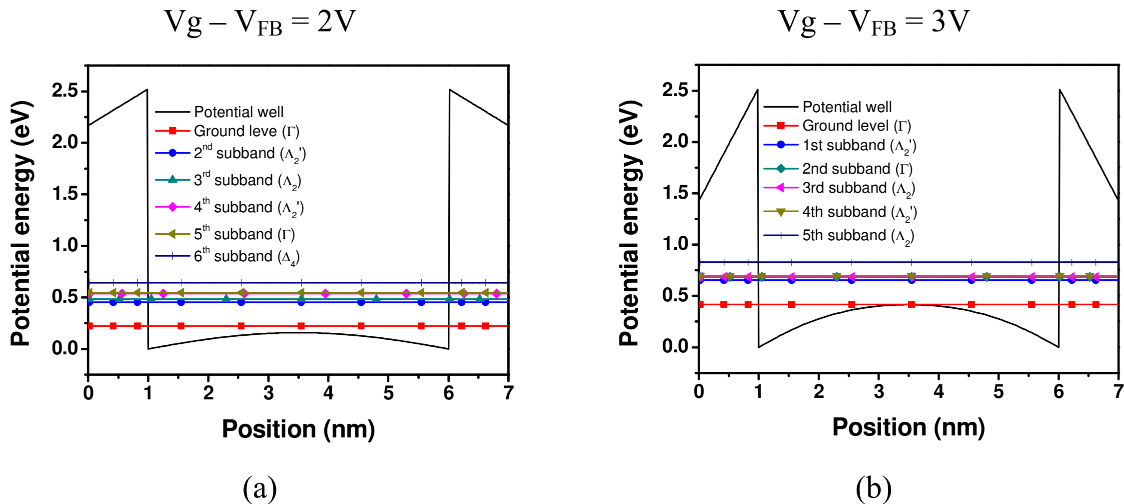

Figure 2.16 : Subband structure of a GaAs DFGETs oriented on a (110) surface. t_{ox} is equal to 1nm, t_{sc} to 5nm. The gates voltage is equal to 2V (a) and 3V (b).

To illustrate the role of the valley occupation on the drain current anisotropy versus applied bias, drain current versus in plane channel orientation have been plotted for 5 nm body GaAs DGFETs for each valleys in Figure 2.15 at different gate bias conditions ($Vg - V_{FB} = 2V$ and 3V). In both cases, a current anisotropy is observed, but the amplitude of this anisotropy in the [110] direction is modulated by the applied gate voltage. At $Vg - V_{FB} = 2V$, the Γ valleys still dominates, but the contribution from the Λ_2' induced an anisotropy with a best current in the [110] direction. However, at $Vg - V_{FB} = 3V$, the contribution from the Γ valleys decreases, while the one of the Λ_2' increases as its occupancy increases, leading to an increased anisotropy in the [110] direction.

This is confirmed on Figure 2.17 (a), which shows the relative occupancy of most populated valleys in GaAs, i.e. the Γ, Λ_2 and Λ_2' valleys. At low voltage (subthreshold condition), carriers are located in the Γ valley. When the gate voltage is increased, the relative Λ valleys population increase, as the density of states of the Γ valleys is extremely small ($m = 0.067\ m_0$) while the Λ_2' ones is much larger. At large voltage, the relative occupancy of the Γ valleys is even lower than the one of the Λ valleys.

It can be also noticed on Figure 2.17 (b) that the best injection velocity is obtained in Γ valleys (due to its lower effective mass, the $F_{1/2}$ factor in (2.25) is much larger than in the case of other Δ or Λ valleys). However, the global injection velocity (which is an average of all the subband injection velocities weighted by subband occupancy [AssaTED00][FerrTNANO07], as shown in equation (2.30)) is lower in strong inversion than the Γ valley own injection velocity, because of the increasing role of Λ_2' valleys. This confirms the necessity of properly taking into account all the valley minima in this kind of study.

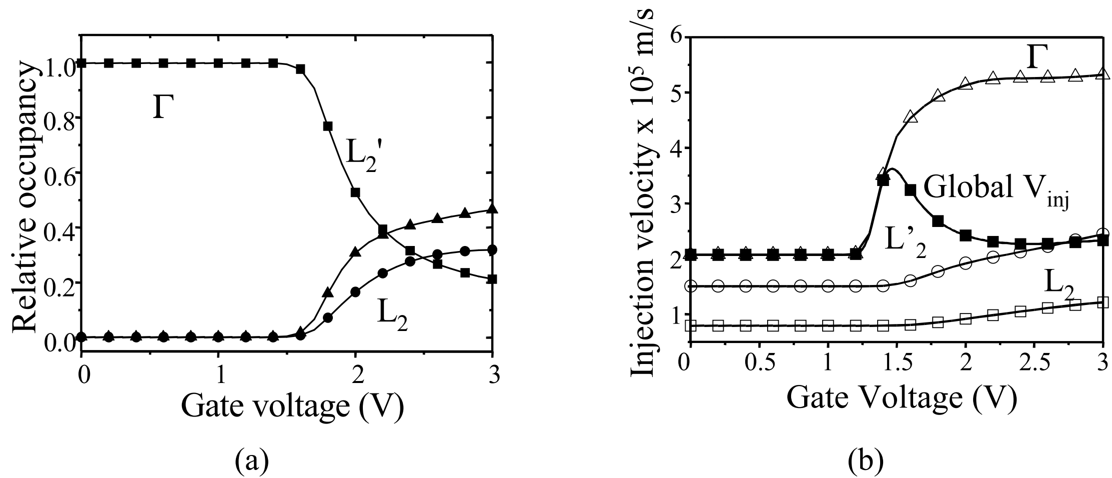

(a) (b)

Figure 2.17 : Impact of gate voltage on relative subband occupancy (Fig. 6A) and injection velocity in channel direction (Fig. 6B) in (110) GaAs DGFETs. Body thickness tsc for these DGFETs is 5nm and the Equivalent Oxide Thickness is EOT = 1 nm.

In addition, these results, also obtained in [PethIEDM03] and [DeMiTED07], underlines that despite the good expected on state performance of alternative channel material thanks to their small effective masses, the filling of satellite valleys with lower injection velocity could severely degrade the on current of these devices.

2.3.2.3 Transport in (110) substrate compared to (100) and (111)

GaAs, InAs and InSb (110) DGFETs have been shown in the previous subsection to have their optimum channel direction in [110], as previously reported for (110) Ge DGFET [LowIEDM03]. In this paper, it is also mentioned that ballistic current obtained in [110] /(110) on Ge device is higher than on the (100) and (111) substrate.

This aspect is thus reinvestigated for GaAs, InAs and InSb DGFETs in Figure 2.18. This figure shows the ratio at a constant inversion charge and as a function of the semiconductor film thickness of the drain currents on (110) surface with a channel along [110] divided by the currents obtained on (100) surfaces.

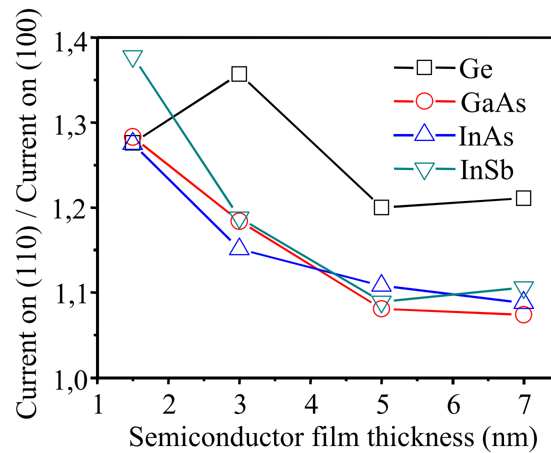

Figure 2.18 : Ratio of the maximum current on (110) and the current on (100) substrate as a function of the semiconductor film thickness for Ge, GaAs, InAs and InSb DGFETs. The value of the current are taken at a constant carrier density of 10^{13} cm^{-2}/gate.

It can be seen from Figure 2.18 that the drain current of GaAs, InAs and InSb DGFETs on (110) surface with channels aligned in the [110] direction is always higher than the drain current on (100) surface for all semiconductor thicknesses. In addition, except for Ge, these ratios tend to increase with the reduction of the semiconductor film thickness t_{sc}.

This slight decrease of the current ratio for Ge DGFETs at body thickness lower than 3 nm is explained by a strong increase of the injection velocity under the (100) due to the filling of the Δ_2 valleys [LowIEDM03], [LauxIEDM04] (better injection velocity of the Δ_2 valleys due to smaller in-plane masses).

This effect is analyzed on Figure 2.19, showing subband occupancy and injection velocity in the case of GaAs for both (100) and (110) substrates. While the injection velocity tends to remain constant in the case of (100) substrate, it increases in [110]/(110) devices when reducing the body thickness at same inversion charge, thanks to the role of Λ_2’ valleys.

Finally, the (111) surfaces have not been considered here, as it is already clear from Figure 2.11 that the current on (111) is lower than on (100) for the 4 materials considered here.

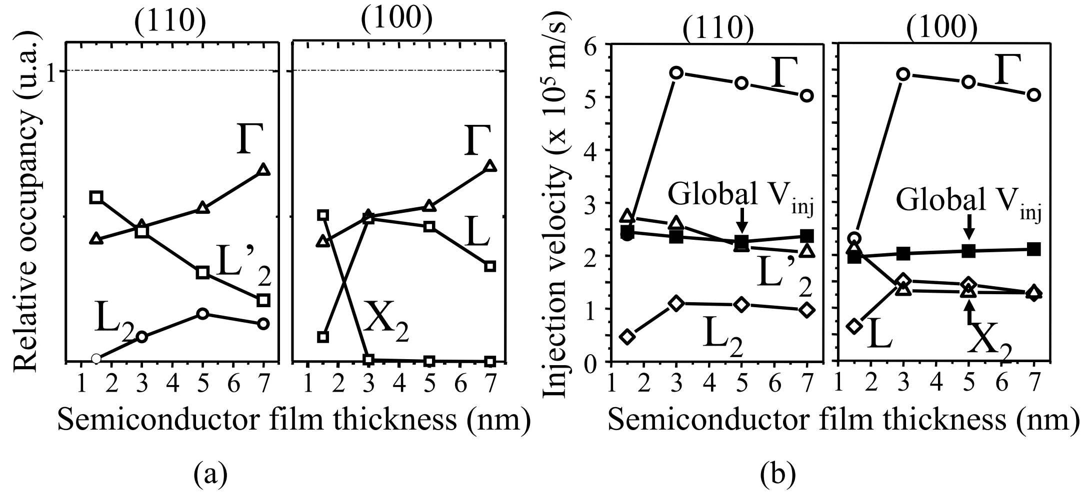

Figure 2.19 : Impact of body thickness on relative subband occupancy (a) and injection velocity in channel direction (b) in (110) and (100) GaAs DGFETs. The values of current are taken at a constant carrier density of 10^{13} cm^{-2}/gate.

2.3.3 Impact of the bandstructure modification in presence of strong quantization: a literature review

It is important to note that the results presented in the previous subsection have been obtained in the framework of the effective mass approximation and that the effective masses used in this work were the bulk ones. However, the DGFETs simulated often featured ultra-thin semiconductor film and the bandstructure is known to be strongly modified in these quantum structures.

It has been proved at first in [RahmIEDM04] that using the bulk effective mass leads to significant overestimation of the ballistic drain current of germanium DGFETs. The authors therefore suggest that full bandstructure should be used to properly model alternative channel performance.

However, this analysis did not demonstrate that the effective mass approximation, i.e. the assumption of parabolic bands, was not valid anymore for ultra-thin film devices. In [SteeTED07], [ZhuIEDM], [CantIEDM07], [LiuTED08] and [PalTED08], the authors have shown that the effective mass of Si, Ge, InSb GaAs and InAs could be fitted on the modified bandstructure of ultra-thin film. In [SteeTED07], the authors have used the Local Combination of Bulk Band approach, while in the other reference (all from the Purdue group), a Tight Binding calculation has been used.

Figure 2.20 presents the in-plane effective mass as a function of the film thickness of Si, Ge, GaAs, InAs and InSb obtained in these references. It can be seen at first that above 5nm, the bulk effective mass value still fairly reproduce the bandstructure. When the semiconductor film thickness is reduced below 5nm, the effective mass required to fit the bandstructure increases significantly. According to [ZhuIEDM06], only the in-plane effective mass of the Δ_2 valley of silicon is decreased in one direction, which seems however to be in contradiction with the results obtained in [SteeTED07] where this valley remains isotropic.

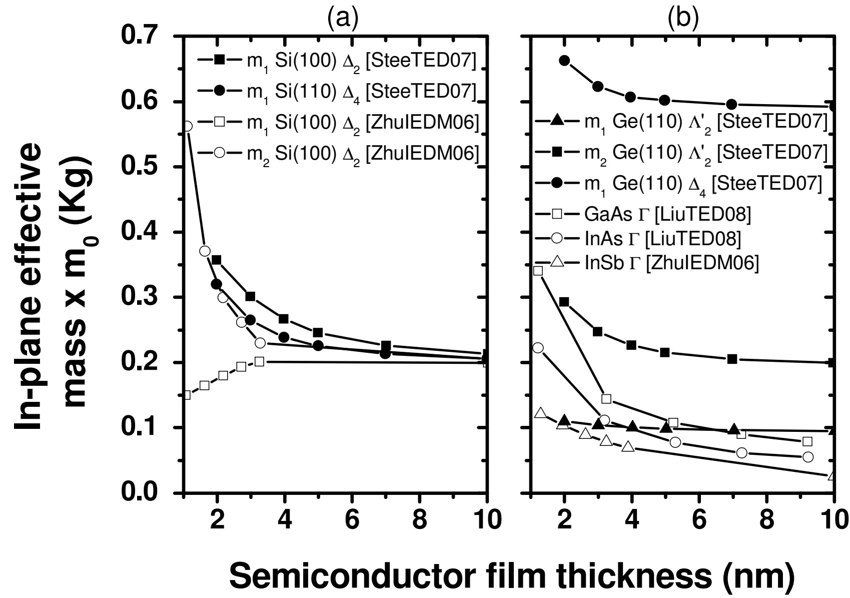

Figure 2.20 : In-plane effective as a function of the semiconductor film thickness of Si (a), Ge, GaAs, InAs and InSb (b). The name of the valleys corresponds to Figure 2.6, while m_1 and m_2 correspond to the in-plane effective mass in the principal axis of the ellipse.

Even if the work presented in this chapter should rigorously need a full re-investigation, it is possible to evaluate qualitatively the impact of these increasing effective mass with a reduction of the semiconductor film thickness.

Assuming that the isotropy of the Γ and Δ_2 are not modified, as shown in [SteeTED07], the drain current on a (100) and (111) surface would still be isotropic on ultra-thin film. Due to the increase of the effective mass of the Γ valleys in III-V material, the satellite valleys causing the anisotropy of the (110) surface will be depopulated. This anisotropy is thus expected to be weaker in ultra-thin film.

In this framework, the impact of the effective mass increase on the overall device performance is less obvious, as two antagonist mechanisms are being involved. The depopulation of the satellite valleys would indeed reduce the injection velocity degradation (shown in Figure 2.17), inducing a drain current increase. But the increase of the effective mass is also expected to decrease the injection velocity, resulting in a lower drain current. It is therefore compulsory to carry out the full calculation in this case. This has already been carried out for Ge and InSb, where it has been respectively shown in [RahmIEDM04] and [ZhuIEDM06] that the drain current is globally lower with fitted effective mass than with bulk effective masses. This procedure, not included in this present chapter, will be investigated in the future.

2.4 Conclusion

A semi-analytical model of the ballistic drain current valid for any channel material and any channel orientation has been presented in this chapter. This model has been obtained from the generalization of the Natori model only valid in its original version for conventionally oriented silicon channel devices. This generalized model allows a fast estimation of many technological options.

However unrealistic in Silicon channel longer than 10 nm, the full ballistic transport approximation used in this work is expected to be more appropriate in high mobility channel material such as Ge or GaAs (even if transport simulation accounting for scattering are required to investigate this point). Nevertheless, factor of merits in the full ballistic regime such as the injection velocity for instance has been shown to also play an important role in the quasi ballistic regime (where devices are more likely to operate), justifying the use of this transport regime in the analysis of the on state current in alternative channel material [LundTED02].

This analytical treatment of the full ballistic current enabled deeper investigation of the impact of substrate orientation and channel direction on the on state current of alternative channel material DGFETs and in particular its isotropy on the (100) an (111) surface and its anisotropy on the (110) one. The in-plane isotropy of the ballistic drain current on (100) and (111) surfaces, previously obtained only as a result of time consuming numerical simulations on Ge DGFETs [LowIEDM03], can be easily explained by the symmetry properties of the minima of the Zinc Blend semiconductor. A detailed study of the anisotropy of the ballistic drain current on (110) surface showed some common trends between various semiconductors of the zinc-blend and diamond lattice structure. The bandstructure (here treated through the simple Effective Mass Approximation) and hence the occupancy of the different valleys determine the best current direction on the (110) surface. Finally, this work showed that the optimum channel orientation of GaAs, InAs and InSb DGFETs is on (110) surfaces with a channel aligned in the [110] direction, as already obtained for arbitrarily oriented Ge DGFETs in [LowIEDM03] and [LauxIEDM04].

It has to be noted that the results obtained in this chapter considered constant effective mass equal to the bulk values. No effect of the quantization on the bandstructure has been taken into account. However, and as underlined in the last subsection, this work should be re-investigated using fitted effective mass, as carried out in [ZhuIEDM06], [CantIEDM07], [LiuTED08] or [PalTED08].

The results shown in this chapter cannot be seen a comparison, even though data for different channel material are shown on same graphs. The comparison at that stage is indeed too biased if done at constant charge. It is thus more rigorous to compare alternative channel material at the same device off current. In this scope, the impact of subthreshold leakage mechanisms on the ballistic I_{on}-I_{off} trade-off will be consequently investigated in chapter 3.

Chapter 3 : Source-drain leakages in alternative channel material

Chapter 3 : Source-drain leakages in alternative channel material 63
3.1 Introduction 64
3.2 Modelling of subthreshold source-drain leakage mechanisms...................................... 65
3.2.1 Impact of source-drain leakage mechanisms on the device performance 65
3.2.2 Short Channel Effect and Drain Induced Barrier Lowering (SCE and DIBL) 66
3.2.3 Source to Drain Tunnelling (SDT)... 70
3.2.4 Band to Band Tunnelling (BBT).. 77
3.3 Impact of source-drain leakages on the performances of alternative channel material nano-MOSFETs 80
3.3.1 Comparing channel material 80
3.3.2 Role of effective masses and band gaps on the performances of nano nMOSFETs... 87
3.4 Conclusion... 95

3.1 Introduction

The previous chapter has described the modelling of the full ballistic on current of alternative channel material nMOSFETs. The impact of channel orientation has been at first identified as a possible mean of device performance enhancement. However, the accurate performance comparison versus material parameter requires to consider not only the on state current, but also the off state current. Thus, this comparison indeed requires to account for the determinant source-drain leakage mechanisms, which have been found in the literature to particularly impact the performance of these devices.

In previous works where tunneling leakage mechanisms have been ignored [TakaVLSI03] [DeMiTED07], alternative channel materials have been found to largely overcome silicon, despite their reduced Density of states (DOS), which leads to enhanced parasitic quantum capacitance [DeMiTED07] (or "DOS bottleneck" effect [FiscTED07]). In other works, Band-to-Band Tunneling (BBT) has been identified as a critical mechanism of leakage degradation, especially in small bandgap materials [SaraVLSI07] [PethIEDM05] [FiscTED07] [LauxTED07] [LowIEDM03]. More recently, the detrimental impact of Source-to-Drain Tunneling (SDT) on the leakages in alternative channel material devices has been also demonstrated [LowIEDM03] [CantIEDM07]. In this latter work, when gate lengths below 10 nm were considered, alternative channel materials were found to be even less attractive than conventional silicon.

The literature review presented in the introduction of this work underlined that the absence of consensus on the "best" existing alternative channel material. This is partially due to the fact that, most of the previous works do not consider all the relevant physical mechanisms. To our knowledge, such a complete analysis has only been carried out in reference [LauxTED07], combining results obtained by Monte Carlo and Non Equilibrium Green Function simulations. However, only relatively long channel devices were investigated in this work, tending to underestimate the impact of BBT and SDT leakage mechanisms (L = 22 and 17 nm in [LauxTED07], compared to the ITRS requirement for High Performance 22 and 16 nm nodes: L = 9 and 6 nm respectively).

This chapter aims to compare alternative channel materials in the framework of the full ballistic transport, accounting for all the relevant mechanisms impacting the performance of sub-15nm devices.

To this purpose, the first section of this chapter will describe the modelling of the source drain subthreshold leakage, which have been found to degrade the performance of alternative channel material devices: the short channel effects, the source-to-drain tunnelling and the band-to-band tunnelling.

Then, the second section will present the results obtained with this model in two different ways : a comparison between different alternative channel material DGFETs as carried out in the literature and a deeper study of the leakage mechanisms degrading the devices performances.

3.2 Modelling of subthreshold source-drain leakage mechanisms

The literature has underlined the necessity to take into account leakage mechanisms to compare rigorously alternative channel materials. The origins of the different subthreshold mechanisms considered in this work will be introduced in a first subsection, which will be followed by three subsections, successively describing the modelling of Short Channel Effects (SCEs), Souce-to-Drain Tunneling (SDT) and Band-to-band Tunnelling (BBT).

3.2.1 Impact of source-drain leakage mechanisms on the device performance

The main contributions to the subthreshold leakage current are illustrated in Figure 3.1. The first mechanism of leakages is the conventional thermionic current, which consists in electron moving from source to drain with an energy higher than the potential barrier at the virtual source. In long channel device and in absence of defect in the dielectric (trapped charge, interface states…), the subthreshold swhing may have its ideal value of 60mV/dec at room temperature. However, in scaled devices, the short channel effect increases this subthreshold slope, thus degrading the overall transistor performances. Source-to-drain tunnelling occurs in shorter channel (generally below 15nm) and consists in electron in the conduction band of the source which tunnel toward the drain though the energy barrier. As in the case of thermionic current enhanced by SCEs, SDT increases the subthreshold slope of the transistor. Finally, the last leakage mechanism considered in this work is band-to-band tunnelling, which arise from the tunnelling through the gap of electron from the valence band to the conduction band. This mechanism, known to limit the off current to a minimum value independent of any threshold voltage shift or metal gate work function adjustment, is enhanced by high field occurring close to the drain contact.

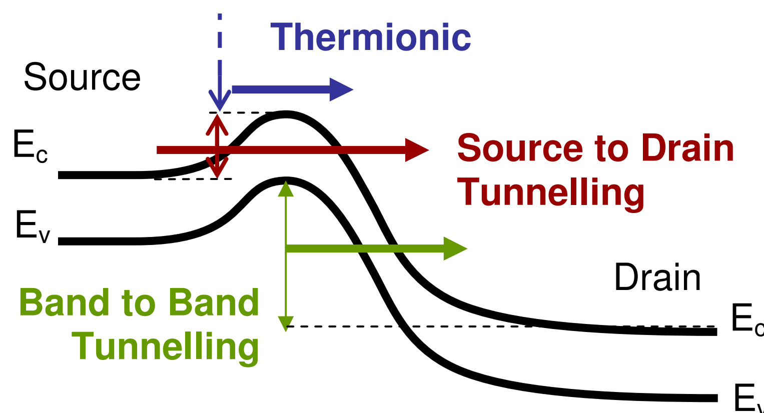

Figure 3.1: Scheme of the three different origins of source to drain leakage considered in this work.

The impact of these three leakage components on the current characteristics of the devices are summarized in Figure 3.2. This sketch highlights the detrimental effect of too large subthreshold current. Indeed, in practice, the threshold voltage (or metal gate work function in case of undoped devices) is adjusted to set the off current value. Therefore, if the subthreshold condition are degraded, a larger threshold voltage (or metal gate work function) will be required, which will also degrades the on state regime.

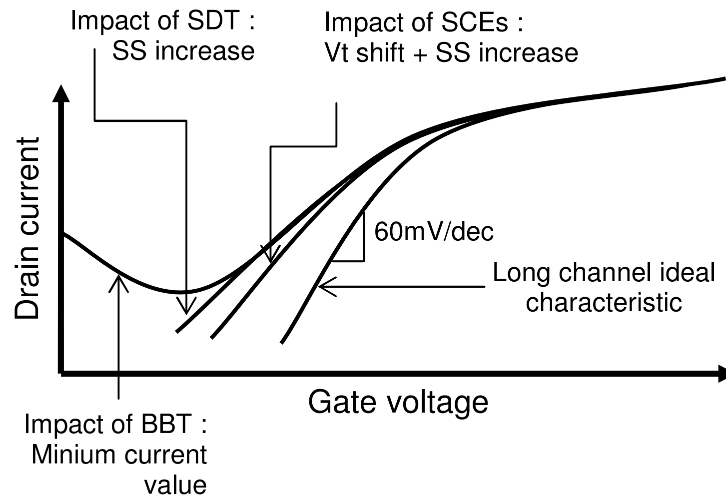

Figure 3.2 : Schematic representation of the impact of SCEs, SDT and BBT on the current-voltage characteristic of a MOS Transistor.

3.2.2 Short Channel Effect and Drain Induced Barrier Lowering (SCE and DIBL)

The short channel effects are electrostatic phenomena which perturb the normal operation of scaled transistors [Taur][Skot]. Due to the proximity of the source and drain, the inversion charge dependence with the external biases is modified with respect to the long channel case. The consecutive impact of the SCEs is illustrated in Figure 3.3 which shows the long and short channel source-drain potential barrier for different bias conditions.

For a long channel MOSFET, when the gate voltage is equal to the flat band one (V_{FB}) and when the drain voltage (V_D) is zero, the conduction band along the source drain direction forms a flat energy barrier whose height is equal to the built in potential of a non-biased pn diode. When the gate voltage is increased, the charge in the channel is also increased, and the energy barrier is self-consistently decreased. If a positive drain voltage is applied, a lateral field accelerates the carriers in the channel, inducing a positive current. In the long channel case, the inversion change at the top of the source drain barrier is fully controlled by the gate voltage, which implies that, for large drain voltage, the current is only a function of the gate voltage (saturation regime).

In the case of a short channel device, the drain is so close to the source that the potential barrier is no longer flat when the gate voltage is equal to the flat band one and when the drain voltage is zero. Therefore, assuming same bias conditions, same built-in and same flat-band voltage, a short channel device will feature a lower source-drain barrier than a long channel one. This lowering results in a smaller threshold voltage for the short devices. This first effect is rigorously called the short channel effect, as it is only caused by the small scale of the device.

In addition, when a driving voltage is applied, the drain potential now influences the potential, even at the source side, which used to be only controlled by the gate voltage in long channel devices. Consequently, an increase of the drain voltage induces a decrease of the source-drain barrier, which lowers the threshold voltage and increases the drain current. This effect is called the Drain Induced Barrier Lowering (DIBL).

For the sake of clarity, both effects will be referred to in this work as the short channel effects (SCEs).

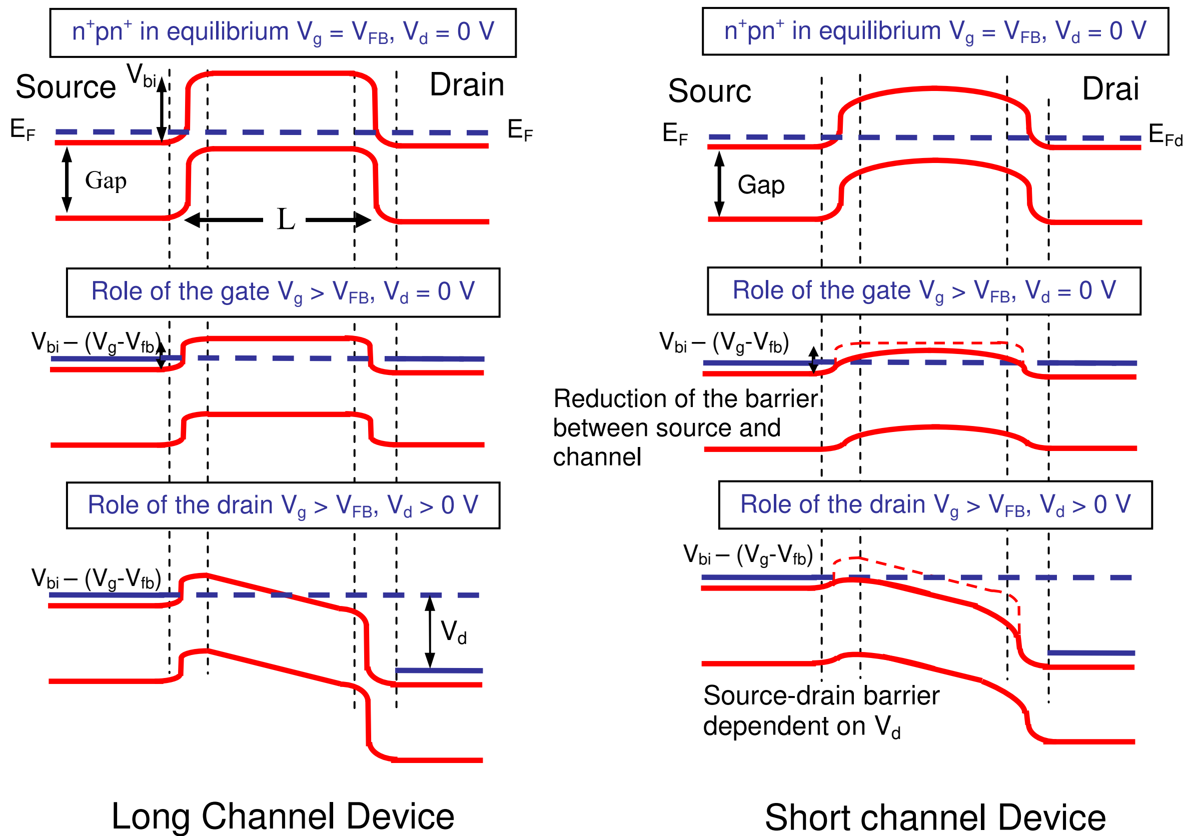

Figure 3.3 : Scheme of the source-drain potential barrier for a long and short channel, in different bias condition (courtesy of R. Clerc).

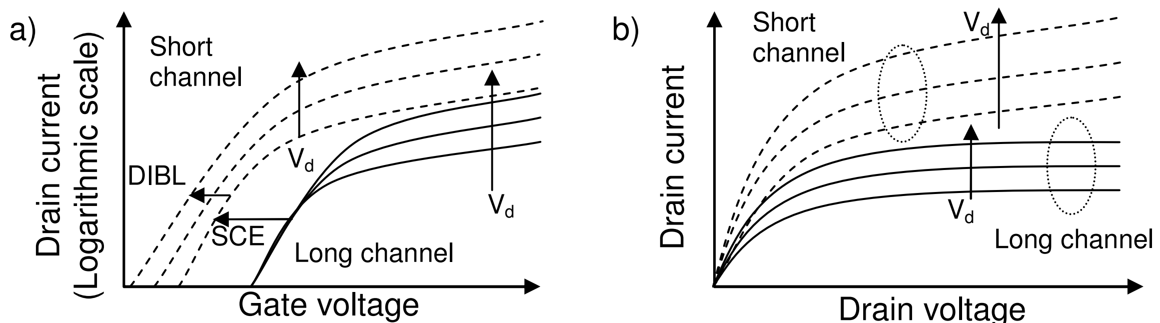

Figure 3.4 : Scheme of the impact of SCEs on a) the drain current versus gate voltage and b) the drain current versus drain voltage characteristics.

The impact of the SCEs on the ideal MOSFET characteristics is illustrated in Figure 3.4. In the case of a long channel MOSFET, the drain voltage increase does not modify the charge on the source side of the channel and the drain current saturates for large drain voltage value. However, for a short channel MOSFET, the threshold voltage is lowered with respect to the long channel device, and is decreased by drain voltage increase (the subthreshold slope is also increased when V_D is increased). In addition, the short channel MOSFET does not feature a clear saturation regime for high drain voltage value.

The modelling of the SCEs mainly consists in the description of the impact of the external bias on the source-channel energy barrier in weak inversion. In this work, the Liu [LiuTED93] analytical model has been chosen for its good first order accuracy and for its excellent computational efficiency. Efficiency is required by the additional and longer calculation involved in the case of SDT and BBT modelling, presented in the next subsections.

The Liu model is obtained by the solution of the Poisson equation in subthreshold condition, i.e. assuming that the charge in the channel and the surface potential are only governed by the depletion layer in the total absence of inversion charge. In this framework, the surface electric potential in the channel is given by :

$$V_s(x) = V_{sL} + (V_{bi} + V_{DS} - V_{sL}) \frac{\sinh(x/l)}{\sinh(L/l)} + (V_{bi} - V_{sL}) \frac{\sinh((L-x)/l)}{\sinh(L/l)} \quad (3.1)$$

With

$$V_{sL} = V_{GS} - V_{FB} + \frac{qN_{SUB}X_{dep}t_{ox}}{\varepsilon_{ox}} \quad (3.2),$$

the long channel surface potential and

$$l = \sqrt{\frac{\varepsilon_{si}t_{ox}X_{dep}}{\eta\varepsilon_{ox}}} \quad (3.3).$$

In (3.1), (3.2) and (3.3), V_{DS}, V_{GS}, V_{bi} and V_{FB} are respectively the drain, gate, built-in and flat band voltage. x is the position along the channel, whose length is L. N_{SUB} is the substrate doping, X_{dep} the depth of the depletion layer, t_{ox} the oxide thickness and η a fitting parameter set to 1. ε_{ox} and ε_{si} are respectively the oxide and the silicon dielectric constant.

To obtain the subband profile along the channel, the electric potential is converted into potential energy ($E_p(x) = -(V_s(x) - V_s(x=0))$ and the subband splitting, calculated at the virtual source by PS1D simulation, is assumed to be identical along the channel.

Figure 3.5 presents the comparison between the source-drain energetic barrier obtained with NanoMOS [NanoHub] (Non Equilibrium Green Function DGFET 2D simulator) and with the Liu analytical model. Even if depletion in the source/channel and channel/drain region and quantum reflection on the energy barrier at are not taken into account in the model, the overall agreement appears to be acceptable. In particular, the top of the source-drain barrier, i.e. energy range where SDT is particularly significant, is quite well reproduced by the model.

The Liu model can however be further improved to reproduce the effects accounted for NanoMOS. In this scope, an effective built-in potential has been considered to include the depletion in source and drain, which consist in increasing the built-in potential and adding a parabolic tail in the source and drain. In addition a Gaussian convolution with the energy barrier is carried out to mimic the effect of quantum reflection on the barrier [Ferry] [HurkALP], following :

$$E_p^{conv}(x) = \int_0^L \frac{E_p(x')}{\sqrt{2\pi\sigma^2}} \exp\left(\frac{-(x'-x)^2}{2\sigma^2}\right) dx' \quad (3.4)$$

where σ is set to 1 nm.

This procedure has also been used in the framework of the Monte Carlo approach in [Lucci]. Figure 3.6 presents the energy barriers of the same DGFETs (same geometries and bias condition) shown in Figure 3.5 but using the improved Liu model. It can be seen that the potential energy in the source and drain extension are now very well captured by the proposed procedure.

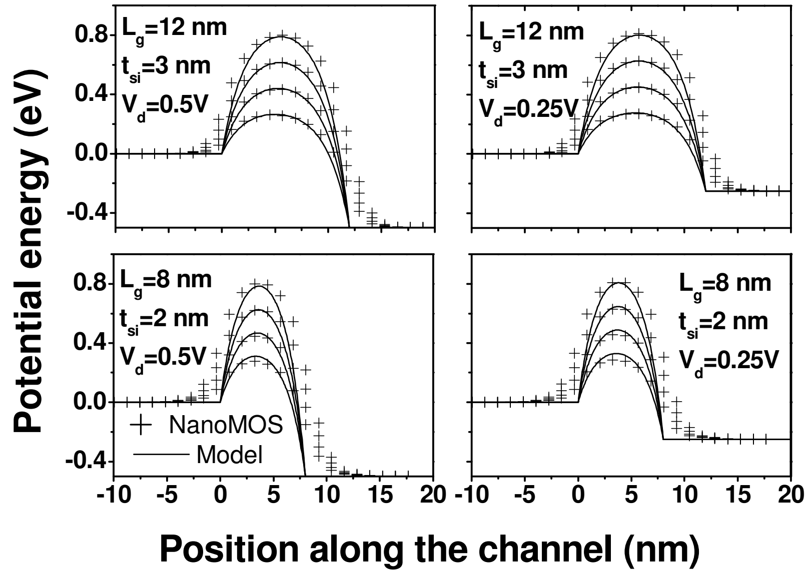

Figure 3.5 : Comparisons between the subthreshold potential energy profile in (100) Si DGFETs along the channel obtained using the Liu analytical model [LiuTED93] (line) and NanoMos simulation [NanoHub] (symbol), for different devices dimensions and drain bias conditions
(EOT 0.7 nm, V_g from -0.6 V to 0 V)

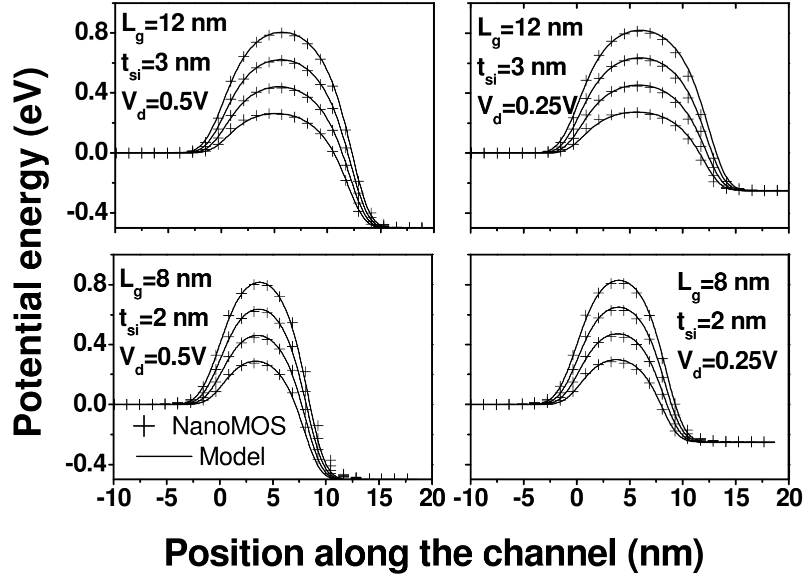

Figure 3.6 : Comparisons between the potential energies in (100) Si DGFETs along the channel in subthreshold regime obtained with the in-house model (line) and NanoMos [NanoHub] (symbol). (EOT 0.7 nm, Vg-V_{FB} from 0 V to 0.4 V)

It has to be noticed that this model is only valid in the subthreshold regime and that it only describes the surface potential. However, in subthreshold condition, the potential in a thin film device like a DGFET is almost constant along its depth, and the model is thus considered to be valid for any position in the film.

3.2.3 Source to Drain Tunnelling (SDT)

3.2.3.1 Starting equations

Direct source-to-drain tunnelling leakages occur in ultra-scaled devices which features gates length generally below 15 nm. This leakage has been identified as a possible source of MOSFETs scaling limitation both theoretically [WangIEDM02] and experimentally [LoliSOIC05].

To model the source-to-drain tunnelling, the same 2D Esaki formula as in the full ballistic current is used as a basis :

$$I_d/W = q\sum_v\sum_n \int_{-\infty}^{\infty}\int_0^{+\infty} \frac{1}{\hbar}\frac{\partial E(\vec{k})}{\partial k_x} T(E_x)\left[f\left(E(\vec{k}),E_{f_S}\right) - f\left(E(\vec{k}),E_{f_D}\right)\right]\frac{dk_x dk_y}{2\pi^2} \tag{3.5}$$

with

$$f\left(E(\vec{k}),E_{f_{S/D}}\right) = \left[1+\exp\left(\frac{E(\vec{k})-E_{f_{S/D}}}{k_b T}\right)\right]^{-1} \tag{3.6}$$

n and v the subband and valley index used also in the previous chapter, T(Ex) the transparency of the energy barrier, $\frac{1}{\hbar}\frac{\partial E(\vec{k})}{\partial k_x}$ the x component of the group velocity (along the channel).

Equation (3.5) is in principle valid for all operating regimes (subthreshold, weak and strong inversion), and takes into account the source-to-drain tunnelling and thermionic current (enhanced by short channel effect barrier lowering) contribution to the off state current. Indeed, the contribution from SDT is obtained by integrating (3.5) from the bottom to the top of the potential barrier while the contribution from thermionic current is obtained by integrating from the top of the barrier to the infinity (in practice, few k_bT are sufficient). It can be directly solved though time consuming self consistent two dimensional Poisson-Schrödinger calculations [CuraSSE04] or by Non Equilibrium Green Function (NEGF) simulations, which enable to solve $T(E_x)$.

As in the case of the full-ballistic on state current, simplification of equation (3.5) may be used to reduce the computational time. However, to account for source-to-drain tunnelling, the transparency can not be considered as equal to zero below the top of the enery barrier and equal to one above the barrier, as in the full ballistic case. Equation (3.5) must then be solved numerically and T(Ex) must be calculated. Nevertheless, the Natori model of the full ballistic current can be deduced from (3.5), if $T(E_x)$ is assumed to be equal to unity. This therefore ensures a good continuity between the formalism used off and on state current calculation, which are both derived from Esaki formulas, and thus avoids using too different modelling approach for these two regimes (like in the case of [LauxTED07], where the subthreshold regime is simulated using the NEGF formalism, and the on regime using the Monte Carlo approach).

3.2.3.2 Transparency calculation

The first step in carrying out this solution is to calculate the transparency $T(E_x)$ of the barrier. Considering an energy profile obtained with the Liu or improved Liu model, the barrier transparency, which is a function of the kinetic energy of the tunnelling wave function, can be calculated using the scattering matrix formalism [Ferry] or the WKB approximation:

$$T(E_x) = \exp\left(-\frac{2}{\hbar}\int_a^b \sqrt{2\, m_t (E_p(x) - E_x)}\, dx \right) \tag{3.7}$$

Where E_x is the energy of an electron in the source-drain direction, m_t the effective mass and $E_p(x)$ the source-drain potential energy barrier, with a and b the turning points values along the channel verifying $E_p(a,b) = E_x$.

The scattering matrix is known to be a more accurate approach than the WKB approximation [ClerJAP02], especially for thin shallow barriers where the turning point are close to each other. However, it is in the meantime a more computationally demanding method. Therefore, the WKB method will be used when computational efficiency is required and the scattering matrix approach when accuracy is needed.

Figure 3.7 compares the transparencies as a function of the kinetic energy of the electron in the source-drain direction, obtained with the scattering matrix approach and NanoMOS, for two geometries of silicon channel DGFET. As the scattering matrix transparency is used to maximize the accuracy of the model, the transparencies have therefore been calculated using an energy profile accounting for the depletion in source and drain and for the quantum reflection on the barrier (i.e. using the more comprehensive barrier model used to obtained results in Figure 3.6). It can be seen in Figure 3.7 that the model reproduce fairly well the results obtained using a more comprehensive tool like NanoMOS.

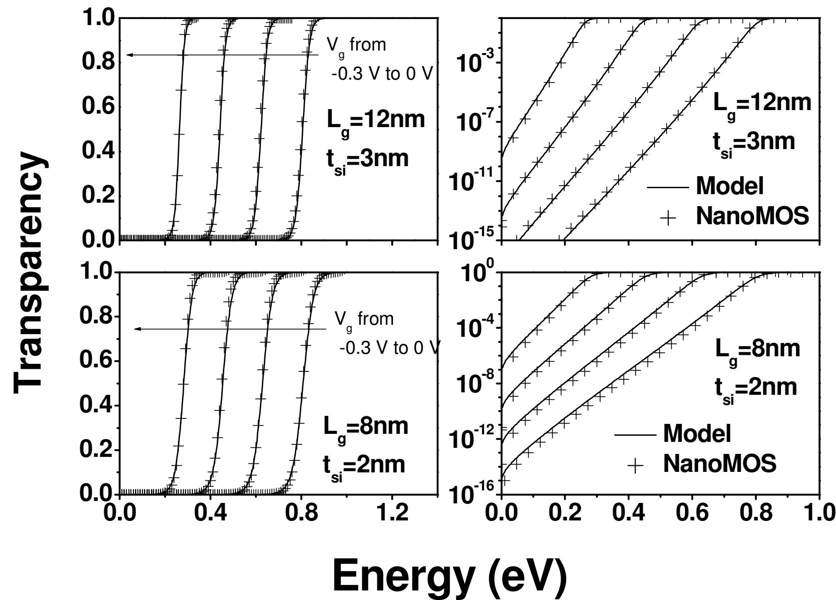

Figure 3.7: Comparison between the transparencies in (100) Si DGFETs vs energy in subthreshold regime obtained with this model using the scattering matrix formalism (line) and NanoMos (symbol) [NanoHub]. (EOT 0.7 nm, V_g-V_{FB} from 0 V to 0.3 V)

When time consuming efficiency is required, the transparency calculation is carried out using the (simple) Liu model converted in energy and the WKB approach. This faster calculation procedure is less accurate, but gives results acceptable enough to be used. Figure 3.8 compares the transparency obtained with the WKB approach and the Liu model and the NanoMOS simulation. It can be seen that a relatively good agreement between the two methods is achieved.

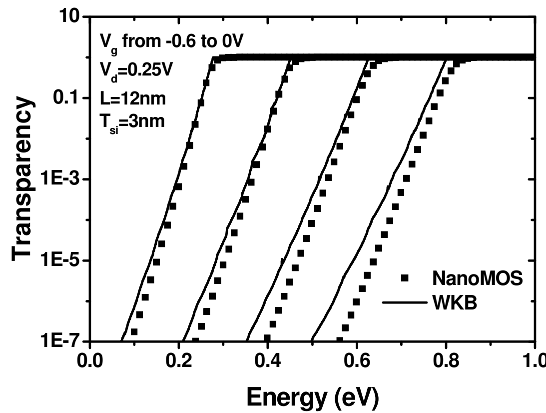

Figure 3.8 : Transparency versus energy, calculated by the WKB approximation on the barrier obtained with the Liu model, compared with NanoMOS results.

Once the transparency has been calculated, equation (3.5) can be integrated numerically. However, here also, two possible options have been considered: a complex model including the contribution from the whole subbands and generalized to any channel orientation (like in the complete model of the on state full ballistic current presented in chapter 2) or a more simple model, independent of the channel orientation, and accounting for only one subband. The two approaches will be presented in the following paragraphs.

3.2.3.3 Multi-subband channel orientation dependent source-to-drain tunnelling current model

A comprehensive model of SDT must include the contribution of several subband and must be derived to account for the source-drain orientation.

At first, the contribution from all subbands of all valleys is simply modeled by the sums over the index n and v in equation (3.5) (respectively the index of the subband and the index of the valley).

To account for the impact of channel orientation on SDT, it is more convenient to integrate equation (3.5) in the polar coordinate system. The source-drain direction is then included in the boundaries of the polar integrations. This change in the coordinate system has already been required to generalize the Natori model of the full ballistic current to any channel orientation. This therefore implies to rewrite all variables in (3.5) as a function of this coordinate system and especially E_x, the energy component in the x direction of an arbitrary oriented electron, of which the transparency is function.

Figure 3.9 sketches the relation between the devices coordinate system formed by (k_x,k_y) and the crystalline one formed by (k_1,k_2) (rotation of an angle α, as in chapter 2) aligned with the principal axis of a single ellipses. It shows in addition the integral boundaries for the polar coordinate θ as a function of the misalignment between the transport direction and the ellipse principal axis.

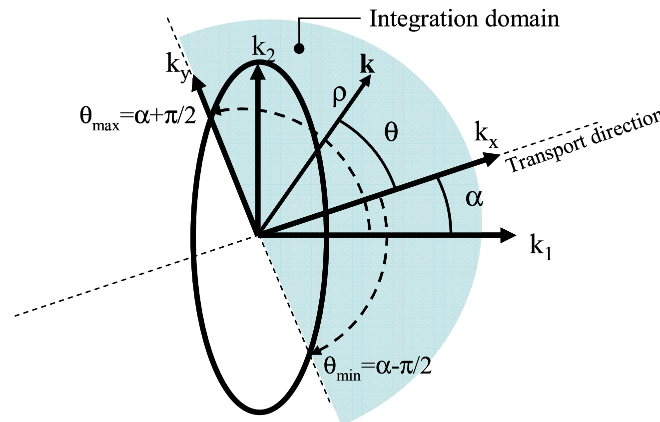

Figure 3.9 : Sketch of the polar integration and the integral boundaries as a function of the misalignment between the devices coordinate system and the crystalline coordinate system. Note that amplitude of θ depends upon angle between the device channel orientation and the crystalline axis.

The first dummy variable change is made to recast the coordinate system used in (3.5) from (k_x,k_y) to (k_1,k_2):

$$\begin{cases} k_1 = k_x \cos(\alpha) - k_y \sin(\alpha) \\ k_2 = k_x \sin(\alpha) + k_y \cos(\alpha) \end{cases} \tag{3.8}$$

This transformation is needed because the E(**k**) relation is only parabolic in the ellipsoid/device coordinate system:

$$E(\vec{k}) = E_n + \frac{\hbar^2}{2}\left(\frac{k_1^2}{m_1} + \frac{k_2^2}{m_2}\right) \tag{3.9}$$

While in the device coordinate system:

$$E(\vec{k}) = E_n + \frac{\hbar^2}{2}\left(\frac{k_x^2}{m_x} + \frac{k_y^2}{m_y} + 2\frac{k_x k_y}{m_{xy}}\right) \tag{3.10}$$

where m_{xy} is the non diagonal term of the mass tensor (see [SterPhyRev67], [RahmJAP05]). Using (3.8), (3.9) and (3.10), the effective masses m_x, m_y and m_{xy}, defined in the device coordinate system, can be expressed as a function of m_1 and m_2, defined in the ellipsoid coordinate system :

$$\begin{cases} \dfrac{1}{m_x} = \dfrac{\cos^2(\alpha)}{m_1} + \dfrac{\sin^2(\alpha)}{m_2} \\ \dfrac{1}{m_y} = \dfrac{\sin^2(\alpha)}{m_1} + \dfrac{\cos^2(\alpha)}{m_2} \\ \dfrac{1}{m_{xy}} = \left(\dfrac{1}{m_2} + \dfrac{1}{m_1}\right)\cos(\alpha)\sin(\alpha) \end{cases} \tag{3.11}$$

In the particular case of the L valleys, the ellipsoids are not aligned with the crystalline axis, but can be recasted in this coordinate system following the procedure detailed in [SterPhysRev67] [RahmJAP05], as explained in chapter 2.

A second variable change is then carried out, in which k_1 and k_2 are expressed as a function of the polar coordinates:

$$\begin{cases} k_1 = \dfrac{\sqrt{2m_1}}{\hbar}\rho\cos(\theta) \\ k_2 = \dfrac{\sqrt{2m_2}}{\hbar}\rho\sin(\theta) \end{cases} \tag{3.12}$$

In this coordinate system, (3.9) becomes :

$$E\left(\vec{k}\right) = E_n + \rho^2 \tag{3.13}$$

In addition, $\frac{1}{\hbar}\frac{\partial E\left(\vec{k}\right)}{\partial k_x}$ and E_X must also be rewritten as a function of θ and ρ to complete the variable change. Using successively (3.10), (3.11), (3.8) and (3.12) :

$$\begin{aligned}
\frac{1}{\hbar}\frac{\partial E\left(\vec{k}\right)}{\partial k_x} &= \frac{\hbar k_x}{m_x} + \frac{\hbar k_y}{m_{xy}} \\
&= \left(\frac{\cos^2(\alpha)}{m_1} + \frac{\sin^2(\alpha)}{m_2}\right)\hbar k_x + \left(\left(\frac{1}{m_2} + \frac{1}{m_1}\right)\cos(\alpha)\sin(\alpha)\right)\hbar k_y \\
&= \frac{\hbar k_1}{m_1}\cos(\alpha) + \frac{\hbar k_2}{m_2}\sin(\alpha) \\
&= \sqrt{\frac{2}{m_1}}\rho\cos(\theta)\cos(\alpha) + \sqrt{\frac{2}{m_1}}\rho\sin(\theta)\sin(\alpha) \\
&= V_x(\alpha,\rho,\theta)
\end{aligned} \tag{3.14}$$

E_x is then simply expressed as a function of the polar coordinate by :

$$E_x(\alpha,\rho,\theta) = \frac{1}{2}m_x(\alpha)V_x(\alpha,\rho,\theta)^2 \tag{3.15}$$

Using (14) and (15), equation (1) becomes:

$$I_d(\alpha)\big/W = q^{5/2}\frac{2\sqrt{m_1 m_2}}{\hbar^2\pi^2}\sum_v\sum_n\int_0^\infty \rho\, f\left(E_n,\rho^2\right)\int_{\alpha-\pi/2}^{\alpha+\pi/2} V\left(\alpha-\alpha_0^v,\rho,\theta\right)T\left(E_x\left(\alpha-\alpha_0^v,\rho,\theta\right)\right)d\theta d\rho \tag{3.16}$$

where :

$$f\left(E_n^v,\rho^2\right) = \left[1-\exp\left(\frac{E_n^v - E_{f_{s/d}}}{kbT} - \rho^2\right)\right]^{-1} \tag{3.17}$$

In (3.16), the α_0^v angle is introduced to shift all ellipses with respect to a common crystalline reference direction, as in the case of the full ballistic current model presented in chapter 2. The values of these specific angles are therefore the same as in the ballistic case and are given in the previous chapter (see subsection 2.2.3.).

Figure 3.10 compares the subthreshold drain current obtained with the NEFG simulator NanoMOS and equation (3.16) (using a transparency calculated using the scattering matrix formalism and the improved Liu model), for two geometries of silicon (100)/[100] DGFETs. It can be seen on this figure that the semi-analytical model and the simulation data are in very good agreement.

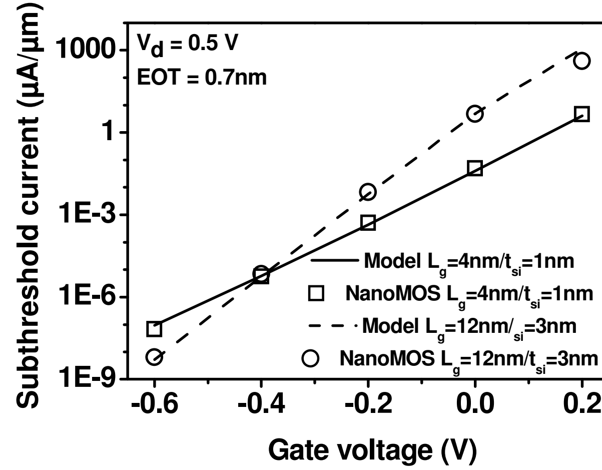

Figure 3.10: Subthreshold drain Current in (100) Si DG, using this model (line) and NanoMos (symbol) (EOT 0.7 nm). The increase of SDT current in 4 nm gate long device is correctly reproduced by the model.

3.2.3.4 Single subband, channel orientation independent source-to-drain tunnelling current model

A less rigorous but however very computationally efficient model of subthreshold drain current including SDT and thermionic current (enhanced by SCEs) can be obtained from equation (3.5). The aim of this model is to give a better understanding of the SDT current variation with the channel material parameter like the effective mass.

It assumes at first that only the first single subband contributes to the leakge current. Therefore, the two sums in (3.5) are dropped. Then, to simplify it at the maximum, it is also supposed that the valley of this single subband is isotropic ($m_1 = m_2 = m_t$), like in the case of the Δ_2 valleys of Si on a (100) surface or like the Γ valleys. In this framework, the integral over k_y in (3.5) can be solved, and the subthreshold drain current reduced to the calculation of a single integral on E_x, the kinetic energy of the wave-particle in the transport direction :

$$I_{off} = q\frac{4\sqrt{2m_t k_b T \cdot q}}{h^2}\int_0^{\infty} T(E_x)F_{-1/2}\left(\frac{E_f - E_0 - E_x}{k_b T}\right)dE_x \quad (3.18)$$

with :

$$F_{-1/2}(u) = \int_0^{\infty} \frac{2dy}{1+\exp\left(y^2 - u\right)} \quad (3.19)$$

In equation (3.18)-(3.19), k_b is the Boltzmann constant; T is the temperature; E_f is the Fermi level on the source side; E_0 is the energy of the single subband.

As this model aims to be as computational efficient as possible, the energy barrier transparency calculation required by equation (3.18) is carried out using the WKB approximation on a barrier obtained with the simple Liu model (no depletion in source and drain and not Gaussian convolution). In Figure 3.11, the subthreshold drain current computed with equation (3.18) has been found in good agreement with more accurate numerical

calculation performed with NanoMOS for two geometries of silicon DGFETs with thin films and conventional orientation.

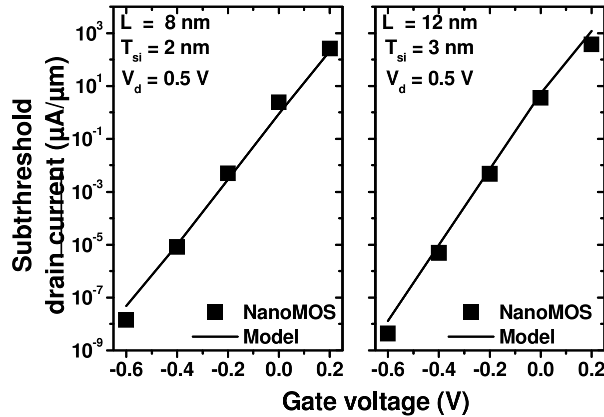

Figure 3.11 : Subthreshold drain current versus gate voltage obtained by the semi-analytical model and NanoMOS results, for different geometries.

3.2.4 Band to Band Tunnelling (BBT)

The Band-to-Band Tunnelling is known to be difficult to model [LyurSSE07], especially for indirect gap materials, where the tunnelling process from the valence band to the conduction band is phonon assisted. To illustrate this point, Figure 3.12 presents a comparison of different results found in the literature regarding the Band-to-Band generation rate in silicon, showing the absence of real consensus on this issue.

The commonly used models of Band-to-Band generation rates rely on the approaches of Kane [KaneJAP61] for direct bandgap semiconductor and of Keldysh [KeldJEPT58] for indirect one. The Kane model is based on a WKB approximation of the current tunnelling through a triangular barrier (the triangle height being the gap) assuming a 2 band dispersion relation in the gap. The Keldysh model rely on the same assumptions but includes the perturbation of the phonon assisted tunnelling process which modifies the wave vector from the centre of the Brioullin zone to the bordel (i.e. the Λ or Δ valleys).

These two models, although computationally efficient, show a great sensitivity on material parameters, and require calibrations on experimental data, which are not always available for alternative channel materials. For this reason, the Kane and Keldysh models for BBT generation rates in this work have been compared and benchmarked with more simulations by Fischetti et al. [FiscTED07]. In this work, the band-to-band regeneration rates is calculated following a simplification of Feymann integrals over all possible tunnelling path in the gap, assuming a parabolic dispersion of the valence and conduction band.

The results obtained in [FiscTED07] and the one obtained with equation (3.20) and (3.21), using the material parameters listed in
Table 3.1, are compared in Figure 3.13.

Equations (3.20) and (3.21), respectively based on the Kane and Keldysh approaches, have been found to fairly reproduce Monte Carlo simulations for wide range of field and materials,

providing the introduction of only one fitting exponential prefactor (independent of effective masses and bandgap) for each model, (A^d for the Kane model and A^i for the Keldysh model).

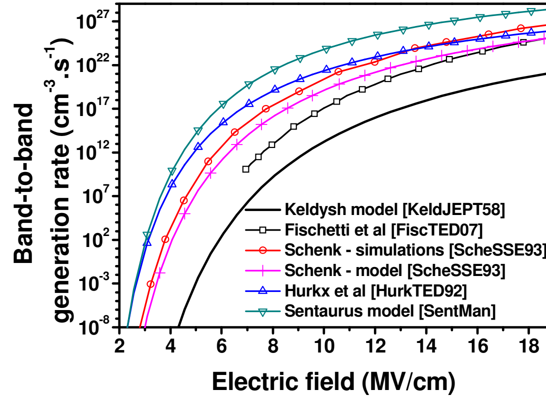

Figure 3.12 : Band-to-band generation rates in Si versus electric field from various literature references. It can be seen that without adjustment, the Keldysh model [KeldJEPT58] underestimates the band-to-band generation rate.

$$G_{bbt}^{dir}(F) = \frac{A^d q^2 \sqrt{m_{//}} F^2}{18\pi\hbar^2 \sqrt{E_g}} \exp\left(-\frac{\pi\sqrt{m_{//}} E_g^{3/2}}{2q\hbar F}\right) \tag{3.20}$$

$$G_{bbt}^{dir}(F) = \frac{A^i q^{2.5} \sqrt{m_x m_y m_z} F^{2.5} M^2 \upsilon}{2^{5.75} \pi^{2.5} \hbar^{4.5} m_{//}^{1.25} E_g^{1.75}} \exp\left(-\frac{4\sqrt{m_{//}} E_g^{3/2}}{3q\hbar F}\right) \tag{3.21}$$

$$\text{With } m_{//} = \frac{m_c \cdot m_v}{m_v + m_c},\ A^d{=}3.10^{-8} \text{ and } A^i M^2\upsilon = 1.10^{-65}\ Kg^{-3/2} m^{-9} s^{-1} \tag{3.22}$$

In equation (3.20) to (3.22), F is the electric field, m_x, m_y and m_z are the effective masse of a given valley of the conduction band in the x, y and z direction. m_c is taken as the minim effective mass of the conduction band (largest tunnelling probability). m_v is the equivalent valence band effective mass ($m_v = (m_{lh}^{3/2} + m_{hh}^{3/2})^{2/3}$).

Material	Gap (eV)	m_c (m_0)	m_{hh} (m_0)	m_{lh} (m_0)
AlAs	2.14	0.2	0.76	0.15
InP	1.35	0.08	0.6	0.089
GaAs	1.42	0.067	0.51	0.082
Si	1.12	0.191	0.49	0.16
$InGa_{0.53}As_{0.47}$	0.74	0.047	0.45	0.052
InAs	0.36	0.023	0.41	0.026
Ge	0.66	0.08	0.33	0.043

Table 3.1 : Material parameters [Ioffe.ru] used to obtain the results presented in Figure 3.13

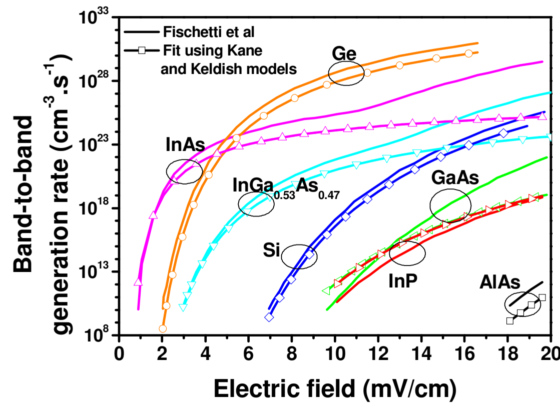

Figure 3.13: Band-to-band generation rates versus electric field taken from [FiscTED08] (straight line) and obtained with the adjusted Kane [KaneJAP61] for direct materials, and the adjusted Keldysh model [KeldJETP58] for of indirect ones (symbols).

Finally, the BBT contribution to the off current leakage is calculated by integrating the BBT generation rates over the electric field resulting from the source-drain subthreshold barrier calculated either with the simple or more comprehensive model.

3.3 Impact of source-drain leakages on the performances of alternative channel material nano-MOSFETs

In this section, the models previously presented, are used to compare different channel material, aiming to determine the most promising one for end of the roadmap devices. It details the results presented in [RafhSSE08_2]

This section is organised in two subsections. At first, the alternative channel material comparison as in other works found in the literature, i.e. by simulating/modelling DGFETs featuring germanium or III-V channels. In this subsection, the accurate but time consuming models are used. The results obtained in this first subsection are then more deeply investigated, focusing on the impact of the most influencing channel material parameters on the device performances. This detailed study requires using the computationally efficient model, as the numerous combinations of channel material parameters explored leads to significant time consuming calculations.

3.3.1 Comparing channel material

This subsection investigates the possible performance enhancement and more importantly the scalability of Ge and GaAs Double Gate MOSFETs (DGFETs) compared to Si and s-Si references. In this framework, the on state current has been assumed as fully ballistic, and estimated according to the generalized Natori model presented in chapter 2. The off state current has been modelled using the more accurate procedure presented in the first subsection of this chapter.

As a sanity check, the channel orientation optimisation in presence of non negligible SDT is at first re-investigated. Finally, the channel materials comparison along the 32nm, 22nm and 16nm nodes of the 2006 updated edition HP 2006 ITRS is then given.

3.3.1.1 Device orientation optimisation

Investigating the possible use of alternative channel material must be associated with the determination of the optimum channel orientation of these devices, as already shown in [LowIEDM03], [LauxIEDM04], [PethSISPAS05] [DeMiTED07] in the case of germanium, and in chapter 2 for various III-V compound materials.

This device orientation optimisation can provide non-negligible ballistic current increase with respect to the standard (100)/[100] device orientation. In the case of Ge, GaAs, InAs and InSb DGFETs, it has been shown in the previous chapter that a larger ballistic current (up to 30% for ultra thin body devices) was obtained for devices on the (110) surface, with a source-drain direction in the [110] crystalline orientation. However, in this study, even if the orientation optimisation has been carried out at constant I_{off}, the effect of source-to-drain leakage has not been included.

Figure 3.14 presents the re-investigation of channel orientation optimisation in presence of non negligible orientation dependent source-to-drain tunnelling when computing I_{off}, in Si, Ge

and GaAs double gate MOSFETs. It can be seen that the source to drain tunnelling does not impact significantly the on-state current dependence with the in-plane device orientation on (100), (110) and (111) substrates and that the previous results obtained in chapter 2 still holds : (100) is the best surface orientation for Si double gate MOSFETs and (110) surface with a channel aligned in the [110] direction is the best orientation for the Ge and GaAs ones.

In the following, Si, Ge and GaAs double gate MOSFETs will only be considered in their optimum orientation, while s-Si double gate MOSFETs will be considered under a (100) surface, like Si.

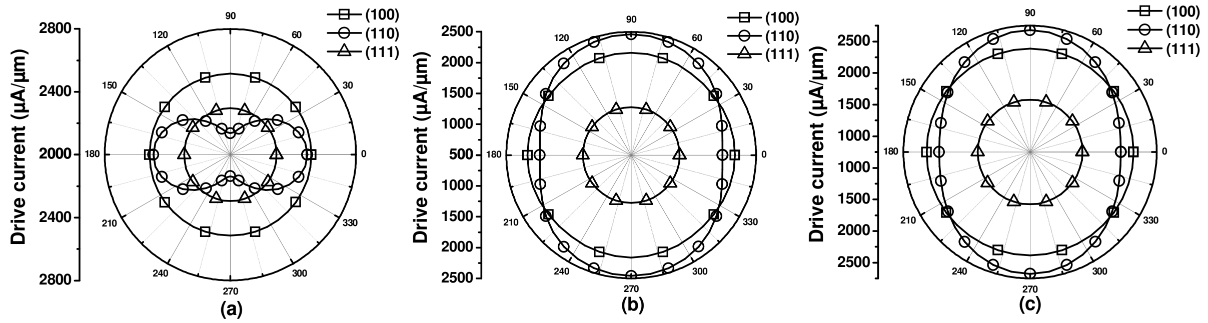

Figure 3.14 : On state drive current Ion versus in plane channel direction for Si (a), Ge (b) and GaAs (c) DGFETs on (100), (110) and (111) substrate (L = 9 nm, tbody = 3 nm, EOT = 1 nm, Vg-VFB = 1.5 V, Ioff = 0.01 µA/µm). Polar angle $\alpha = 0°$ corresponds to [100], [100], [110] on (100), (110), (111) surface respectively for Si, Ge and GaAs channel.

3.3.1.2 Alternative channel material MOSFET performance comparison

In this section, using the previously presented model, the on-state current of double gate MOSFETs optimally oriented with Si, s-Si, Ge and GaAs channels are compared along the 32nm, 22nm and 16nm node of the HP 2006 updated ITRS.

Table 3.1 sums up the various parameters used to design these devices as a function of the technological node while Table 3.3 sums up the bandstructure parameters of the considered materials. In all cases, for a fair comparison between each channel material, the gate work function of each device has been systematically adjusted to meet the ITRS I_{off} requirement specified, as illustrated in Figure 3.15.

	X Valley			L Valley			Γ Valley	
	m_L (m_0)	m_T (m_0)	Gap (eV)	m_L (m_0)	m_T (m_0)	Gap (eV)	m (m_0)	Gap (eV)
Si	0.92	0.19	0	–	–	–	–	–
Ge	0.95	0.2	0.19	1.64	0.08	0	–	–
GaAs	1.9	0.19	0.48	1.02	1.538	0.29	0.067	0
s-Si	0.92	0.19	2 fold: 0 / 4 fold: 0.203	–	–	–	–	–

Table 3.2 : Materials parameters used in this work

Technological Node	32 nm	22nm	16nm
Physical gate length (L)	13nm	9nm	6nm
Body thickness (t_{si} = L/3)	4.3nm	3nm	2nm
Equivalent Oxide thickness (t_{ox})	0.7nm	0.6nm	0.5nm
Power supply voltage (VDD)	0.9 V	0.8 V	0.7 V
Off state leakage current (I_{off})	0.11µA/µm	0.11µA/µm	0.11µA/µm
Effective series resistance	90 Ω.µm	75 Ω.µm	60 Ω.µm

Table 3.3 : Device parameters used in this work to design DG nMOSFET according to the 2006 High Performance ITRS roadmap

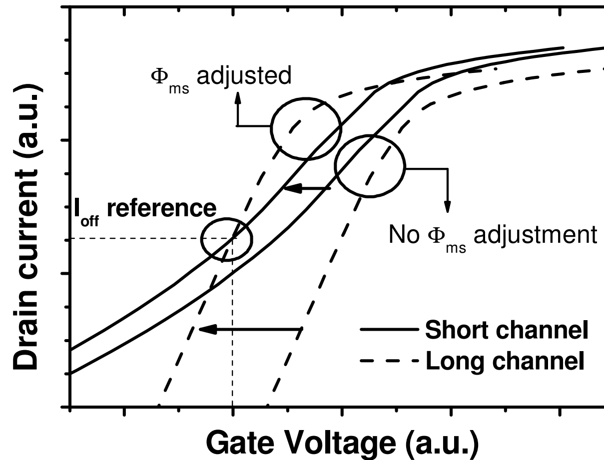

Figure 3.15 : Gate work function adjustment procedure to fix Ioff at the value specified by the ITRS. It can be seen that, after adjustment, all Id-Vg curves meet the Ioff requirement. It can be seen a degraded subthreshold slope leads to a weak gate work function shift than in the case of an ideal subthreshold slope. Consequently, the on state current taken at the supply voltage will be higher for small subthreshold slope than for large one.

At first, the band-to-band tunnelling current including the contribution of all subbands has been estimated in these devices and plotted versus the physical gate length in Figure 3.16. It has been found that, although significant [LowIEDM03], [LauxTED07], [PethIEDM05] and [KimSISPAD06], BBT leakage currents were always lower than the ITRS specifications. Therefore, due to the gate work function adjustment procedure, the fixed common I_{off} value mostly consists, for gate length below 13nm, in source-to-drain tunnelling and increased thermionic current resulting from larger SCEs. These results have be found to be in qualitatively good agreements with [PethIEDM05] and [LauxTED07] (except for the shortest gate length of Ge devices, whose minimum off current have been found in [LauxTED07] to exceed the ITRS specifications).

The on-current of Si, biaxially strained Si, Ge and GaAs double gate MOSFETs, including the effect of source-to-drain tunnelling, quantum capacitance (through PS1D calculations), short channel effect and series resistances (as described in chapter 2) has been simulated following the more comprehensive approach presented in the previous section. Strained Si has been simulated by lifting the degeneracy between the Δ_2 and Δ_4 valleys via the introduction of a gap of 0.192 eV between them. This corresponds to a biaxally strained SOI substrate whose silicon film is grown on a buffer of $Si_{0.7}Ge_{0.3}$ layer.

The on current of these devices has been plotted versus the physical gate length on Figure 3.17, alongside the ITRS expectations. It can be seen that the performances of Ge and GaAs

devices are significantly degraded when the physical gate length is reduced, while their Si and s-Si counterparts maintain relatively constant performances along the technological nodes. In addition, only strained silicon double gate MOSFETs meets the on-current requirements of the ITRS thanks to its moderate SDT equal to the unstrained silicon and its enhanced injection velocity compared to unstrained Si (larger Δ_2 relative population compared to Si) [FerrTNANO07].

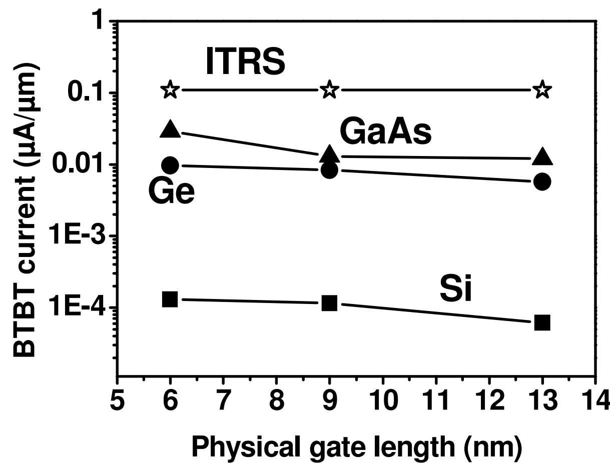

Figure 3.16 : Band to band leakage current at Vg = 0 V (after adjustement) versus physical gate length of double gate MOSFETs devices with Si, Ge and GaAs channel optimally oriented. The Ioff HP 2006 ITRS expectation are also reported (stars).

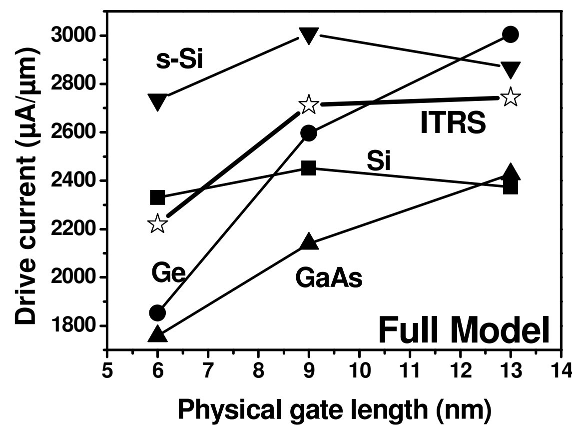

Figure 3.17 : On state drive current versus physical gate length, computed at same Ioff = 0.11 µA/µm (including SDT, BBT, SCEs and access resistances), for Si, s-Si, Ge and GaAs DGFETs. For each length, devices have been scaled according to the 2006 HP ITRS roadmap. The Ion expectation of the ITRS have also been reported (stars)

On Figure 3.18 and Figure 3.19 are respectively reported the threshold voltages, gate work functions and subthreshold slopes corresponding to the on-currents plotted in Figure 3.17. It can be seen that the gate work functions of all materials remain relatively constant along the technology nodes beside significant increase of threshold voltages, resulting from the body thickness thinning (increased quantization). In the meantime, due to large SDT increase, the subthreshold slope of Ge and GaAs are significantly degraded while the ones of the Si and s-Si stay constant thanks to more moderate SDT increase.

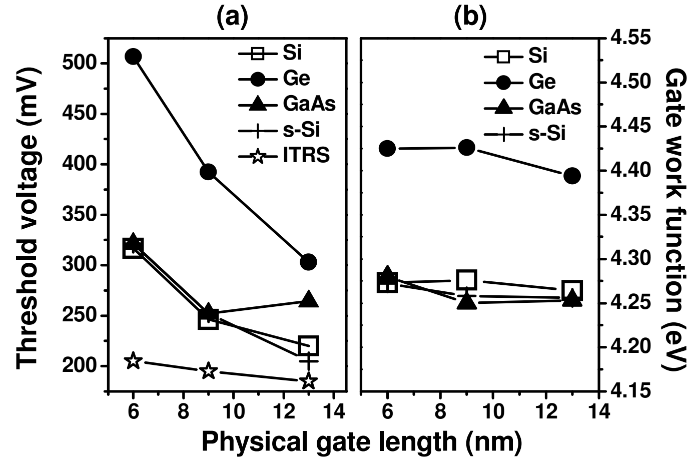

Figure 3.18 : Threshold voltage (a) and gate work function (b) versus physical gate length of Si, s-Si, Ge and GaAs DGFETs, computed to meet the ITRS Ioff requirements (including the effect of SDT, BBT, SCEs and access parasitic resistances). For each length, devices have been scaled according to the 2006 HP ITRS roadmap

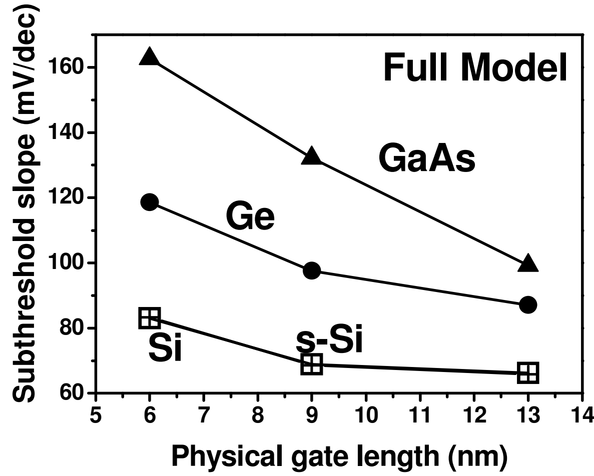

Figure 3.19 : Subthreshold slope vs physical gate length of Si, s-Si, Ge and GaAs DGFETs, computed to meet the ITRS Ioff requirements (including the effect of SDT, BBT, SCEs and access parasitic resistances). For each length, devices have been scaled according 2006 HP ITRS roadmap

This increase of source-to-drain tunnelling in the specific case of Ge and GaAs devices is explained by their smaller effective masses (0.08 m_0 for Ge and 0.067m0 for GaAs) compared to Si and s-Si (0.19 m_0). Even though these results has been computed using the scattering matrix formalism, the dependence of SDT can be more simply understood from the WKB approximation formula in which the mass term is explicit: a reduction of the effective mass increases the transparency and hence increases the tunnelling current.

$$T(E) = \exp\left(-\frac{2}{\hbar} \int_a^b \sqrt{2\, m_x (E_p(x) - E)}\, dx \right) \qquad (3.23)$$

In (3.24), Ep is the potential energy barrier, and a and b the “turning points” along the channel at which Ep(a)=E and Ep(b)=E.

Even though the reduction of the effective mass is beneficial to the on-state current thanks to lower DOS, the increase of the subthreshold current in the Ge and GaAs devices is large enough to significantly degrade their Ion-Ioff trade off. Si and especially s-Si therefore exhibit better scalability properties thanks to a good compromise between injection velocity enhancement with the body thickesses reduction and relative SDT immunity, even at extremely short channel length (around 9nm).

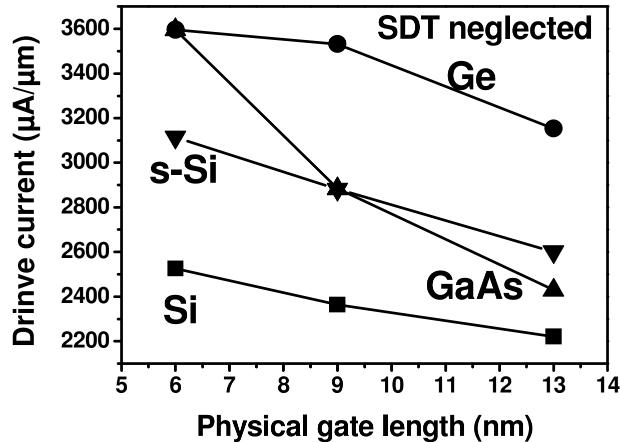

Figure 3.20 : On state drive current versus physical gate length, computed at same Ioff = 0.11 µA/µm (including BBT, SCEs and access resistances but neglecting SDT), for Si, s-Si, Ge and GaAs DGFETs. For each length, devices have been scaled according 2006 HP ITRS roadmap.

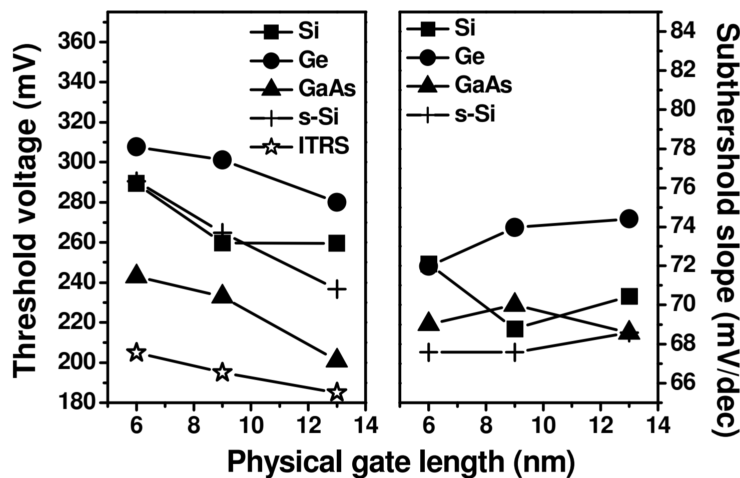

Figure 3.21 : Threshold voltage (a) and subthreshold slope (b) versus physical gate length of Si, s-Si, Ge and GaAs DGFETs, computed to meet the ITRS Ioff requirements (including the effect of BBT, SCEs and access parasitic resistances, but neglecting SDT). For each length, devices have been scaled according 2006 HP ITRS roadmap

Figure 3.20 plots the same I_{on} current as in Figure 3.14, but neglecting the effects of source-to-drain tunnelling. In this framework, Ge and GaAs now outperform Si and s-Si, as obtained in [LowIEDM03] [LauxIEDM04] [RahmIEDM03] [PethIEDM05], [DeMiTED07]

and [LauxTED07]. They indeed take fully advantage of their low density of states, which enhances their injection velocities [FerrTNANO07], despite the quantum capacitance degradation and the progressive filling of low density of states subbands [FerrTNANO07]. As seen in Figure 3.21, the threshold voltages increases fewer when neglecting SDT, and subthreshold slopes remain constant, showing that the short channel effects are well controlled for these geometries.

3.3.1.3 Conclusions

The performance and scalability of Si, s-Si, Ge and GaAs double gate MOSFETs have been investigated in this work with a semi-analytical model accounting for quantum capacitance degradation, short channel effects and source-to-drain tunnelling in any channel orientation. It has been shown that the scalability of the alternative channel material devices, such as Ge or GaAs double gate MOSFETs was very poor due to significant source-to-drain tunnelling increase resulting from their small effective masses. On the contrary, the relatively large effective masses of Si and s-Si temperate the source-to-drain tunnelling increase in these devices. According to the results obtained in this work, only biaxially strained silicon double gate MOSFETs meets therefore the HP 2006 ITRS performance expectations for the 32nm, 22nm and 16nm node. These results confirms the one obtained in [CantIEDM07] with the NEGF simulator NanoMOS and emphasize that SDT may change significantly the prediction in [PetheIEDM05], [TakaVLSI03] and [LauxIEDM04].

In the following subsection, the origin of the performance degradation of alternative channel material devices will be more deeply studied by using a different approach were masses and bandgaps have been considered as continuous variables.

3.3.2 Role of effective masses and band gaps on the performances of nano nMOSFETs

The results obtained in the previous subsection confirmed the conclusions obtained by Cantley et. al. in [CantIEDM07]. For channel length below 15 nm, results suggest that, unless a technological solution is found to reduce SDT in the off state, alternative channel materials would probably not offer significantly enhanced I_{on}-I_{off} performances compared to conventional silicon channel.

The following subsection is an attempt to determine qualitatively the effect of the most impacting channel material parameter on ultra-scaled devices performances. The effective masses and bandgaps have indeed been identified in the previous subsection and in the literature as the most relevant physical parameters responsible for I_{on} and I_{off} degradation in undoped Double Gate nMOSFETs (DGFET). In the spirit of [DeMiTED07], a simplified approach will enable a better understanding of the advantages and drawbacks of alternative channel materials. The approach proposed here considers quantum capacitance degradation Short Channel Effects (SCE), Band-to-Band Tunneling (BBT) and Source-to-Drain Tunneling (SDT).

In this subsection, the original methodology applied in this study is at first described. The results and the conclusion are then presented. This subsection gather the results published in [RafhESoi08] and [RafhSSDM08].

3.3.2.1 Models and methodology

The philosophy of this approach is not to simulate an individual existing channel material, whose effective masses and bandgaps are not continuous enough to give a good understanding of the effect of the material parameters on the device performance[4]. On the contrary, in this work, a generic channel material is considered and its effective mass and energy bandgap are considered as variables. This study therefore focuses on the impact of these channel material parameters on the Ion-Ioff trade off of a template DGFETs.

In this framework, any combination of effective mass and bandgap constitute a single device. Solving the dependence of the Ion-Ioff trade off with the effective mass and bandgap is thus a very time consuming task. Consequently, the computationally efficient models are required. For the subthreshold current, the simple approach described in 3.2.3.4 has been used. For the on current, a specific single subband, orientation independent full ballistic current model is derived as follow :

In this scope, and as carried out in [DeMiTED07], the body thickness t_{sc} has been assumed sufficiently scaled, in order to guarantee a device operation in the quantum limit regime (only one degenerated subband). These two assumptions are not only helpful to develop simple and efficient analytical models, but also to ensure an estimation of the maximum current achievable in ultra scaled DGFETs.

[4] In addition, due to the quantum confinement, the value of the semiconductors effective mass and bandgap are strongly modified and no consensus has yet been obtained on their values in ultra-thin film devices (see 2.3.3.)

The on state current has then been modelled using the Natori approach as in chapter 2 (still accounting for the quantum capacitance degradation, significant in low DOS alternative channel material). This model, in the quantum limit, leads to the completely following analytical formula (3.25):

$$I_{on} = \frac{8\, q^{5/2}\sqrt{m_t}}{3\pi^2\hbar^2}\left(\frac{Q_{inv}}{C_q}\right)^{3/2} \tag{3.25}$$

with

$$Q_{inv} = 2\frac{C_{ox}\cdot C_q}{C_q + 2C_{ox}}\left(V_g - V_t\right) \tag{3.26}$$

and

$$C_q = \frac{q^2 m_t}{\pi\hbar^2} \tag{3.27}$$

In equation (3.25)-(3.27), m_t is the transport effective mass, C_{ox} the oxide capacitance, V_g the gate voltage and V_t the threshold voltage (function of the single subband energy and thus of the semiconductor film thickness t_{sc}).

The validity of the quantum limit approximation is investigated in Figure 3.22, showing the total capacitance, the inversion charge and the drain current as a function of the gate voltage (corrected from the flat band voltage). A good agreement with numerical Poisson Schrödinger simulation is obtained in extremely thin body (1 nm) device. But, as expected, the quantum limit approximation no longer applies when thicker body device (5nm) are considered. As shown in Figure 3.22 (b), the semiconductor film thickness only impact the threshold voltage : the current voltage curve is simply shifted toward smaller voltage value when going from t_{si} = 1 to 5 nm. In more complex calculation, the current characteristic of a 5 nm thick silicon DGFET operating in the ballistic limit is degraded by lower injection velocity due to the filling of large density of states subbands [DeMiTED07], [PetheIEDM05], [RafhSSE08].

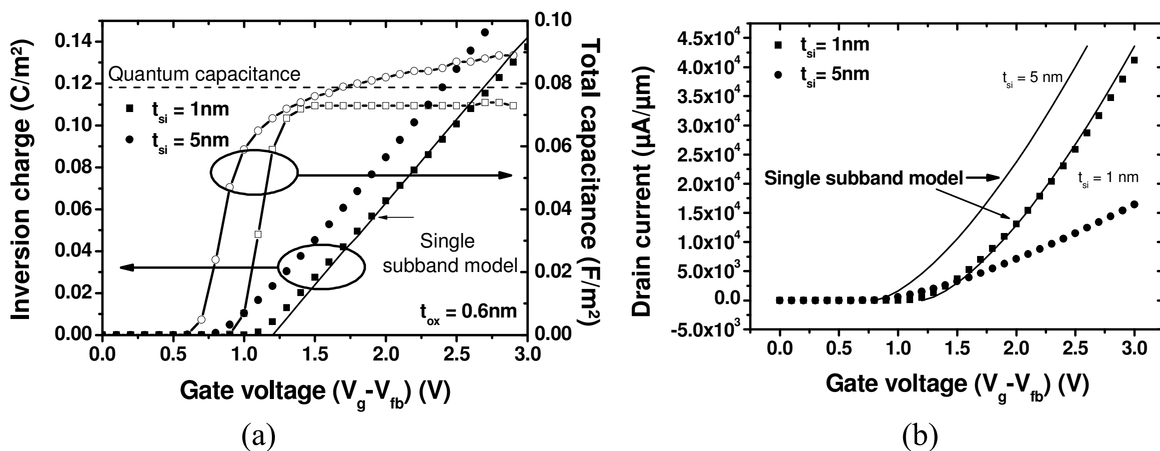

Figure 3.22 : (a) Inversion charge and total capacitance as a function of the gate voltage in silicon, obtained by Poisson-Schrödinger 1D (PS1D) simulation (open and filled symbols) and single subband model (solid line). The quantum limit approximation only applies in extremely thin body thicknesses. (b) Ballistic drain current as a function of the gate voltage obtained by PS1D calculation in silicon channel, compared with the analytical quantum limit model. On both figures, V_d = 1 V, EOT = 1nm.

Even though this model is less accurate than the on current model used in the previous subsection, the single subband assumption ensures to consider systematically the largest possible on state current achievable by the device.

To study the impact of the alternative channel material on the DGFETs performances, the following standard procedure has been applied:

1. The DGFETs geometries and bias conditions have been selected according to the 2007 ITRS [ITRS2007]. High Performance specifications for the 22 and 16 nm technological nodes;
2. Considering a constant quantization mass m_q equal to 1 m_0, the off and on state currents of the DGFETs have been calculated for varying transverse transport effective mass m_t and varying gap E_g;
3. For each device and each combination of effective mass and bandgap, the metal work function has been tuned in order to meet the HP ITRS 2007 off leakage requirements.

3.3.2.2 Results and discussions

An illustration of the impact of effective masses and energy bandgaps on the subthreshold characteristics on DGFETs is shown on Figure 3.23 and Figure 3.24, considering a DGFET designed according to the 16 nm node, with an indirect channel material.

It can be seen on Figure 3.23 that, when only SDT and thermionic current (enhanced by SCEs) are taken into account, the subthreshold slopes of the device are significantly increased when the effective mass is decreased. When BBT is included, the subthreshold characteristic features in addition a minimum current value I_{off_min}, which tends to increase, when reducing the effective mass. On the contrary to SDT and SCEs leakages, that can be reduced at $V_g = 0V$ by increasing the threshold voltage, this I_{off_min} is not affected by a simple change of gate work function. In the worst case, for very low bandgap and effective mass, I_{off_min} can eventually exceed the ITRS I_{off} requirements.

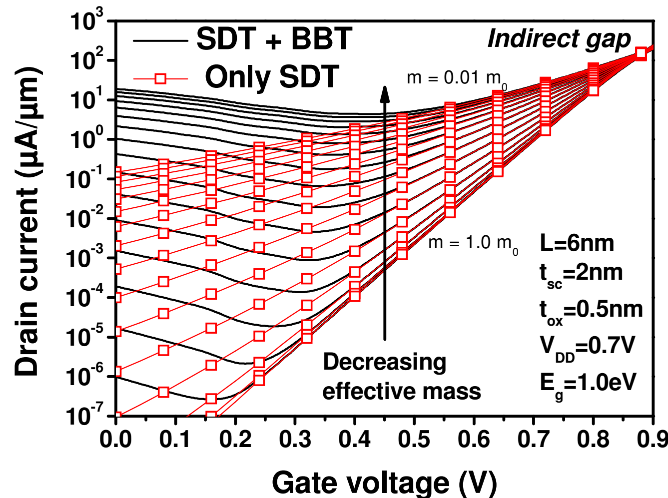

Figure 3.23 : Subthreshold drain current versus gate voltage including SDT, SCEs and BBT, or SDT and SCEs only, for various effective masses in indirect materials. Decreasing effective mass degrades subthreshold slope (because o SDT) and increases the BBT contribution. The effective mass goes from 0.01 to 1.00mo logarithmically. (no metal gate work function adjustment)

The subthreshold I_d–V_g characteristics of the same DGFET (at same work function) with different bandgaps and a constant effective mass is shown on Figure 3.24. When only SDT and thermionic current are accounted for, the characteristics are simply shifted due to threshold voltage increase. Nevertheless, when BBT is included, the reduction of the bandgap value induces an increase of this leakage, and consequently an increase of the minimum off current achievable $I_{off\ min}$.

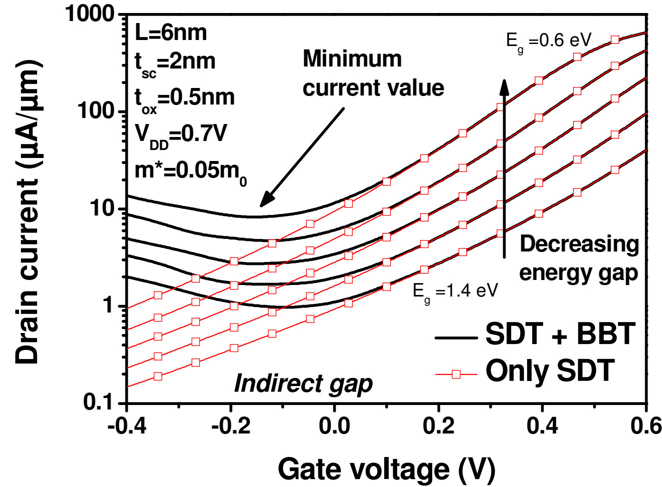

Figure 3.24 : Subthreshold drain current versus gate voltage including SDT, SCEs and BBT, or SDT and SCEs only, for various E_g in indirect materials. The metal gate work function is kept constant in this figure. Decreasing the energy gap leads to an increased minimum current value when BBT is included, while the SDT and SCEs contributions are only shifted when the gap increase, due to the increase of threshold voltage V_t. The bandgap value goes from 0.6 to 1.4 eV (steps of 0.2eV). (no metal gate work function adjustment)

These variations of subthreshold characteristics with the effective mass or bandgap have been found to strongly impact the corresponding on current if a constant I_{off} is assumed.

Considering moderate indirect or direct gaps (1.0 eV) material, the on state current of DGFETs designed according to the 22 and 16 nm nodes of the ITRS have been plotted as a function of the effective mass in Figure 3.25. For both direct and indirect material, if E_g is sufficiently large, a maximum of on state current is obtained for an effective mass of 0.15 m_0 in case of the 16nm node, and 0.25 m_0 in the case of the 22 nm one.

This maximum of on state currents results from the competition between two mechanisms enhanced by the effective mas reduction. First, the decrease of the effective mass induces a beneficial increase of injection velocity in the on state [FerrTNANO07], and hence of the drain current. Second, when the effective mass becomes too small, the Source-to-Drain Tunneling significantly degrades the off state current characteristics. To keep a constant leakage current, the threshold voltage has to be increased by metal gate work function tuning, penalizing the on current.

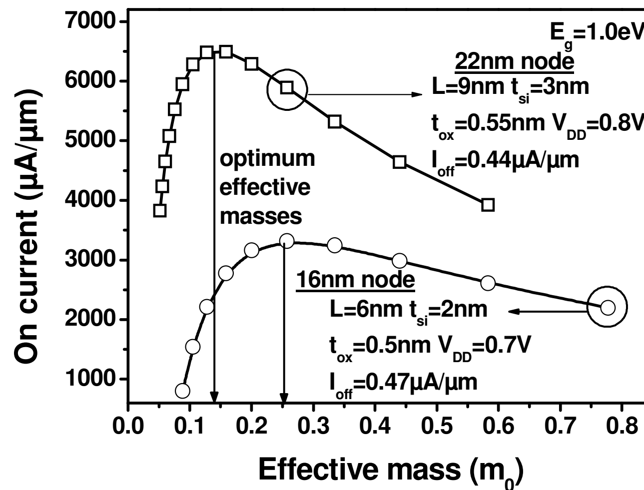

Figure 3.25 : On current versus effective mass for different bandgaps for the 22nm and 16nm nodes of the HP-ITRS 2007 for indirect and direct material, at constant I_{off}., for a large bandgap of 1.0eV.

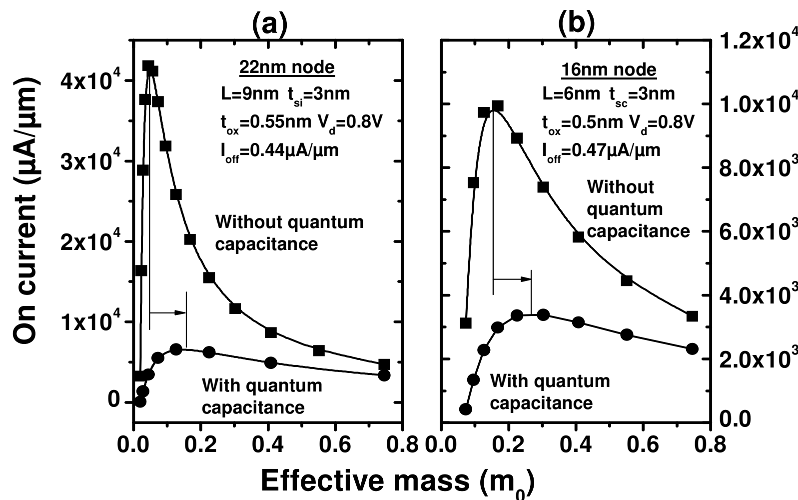

Figure 3.26 : On state drain current versus effective mass for two double gate FETs designed according to the 22 (a) and 16nm (b) node of the ITRS with and without quantum capacitance. Including quantum capacitance increases the optimum effective mass value.

In addition to the detrimental impact of SDT, the decrease of quantum capacitances in low DOS material (see equ. (3.26)) also plays a role in the on current degradation of small effective mass material. Figure 3.26 compares the on current versus the transport effective masses of the two different DGFETs designed according to the 22 and 16 nm node of the ITRS, including or not the quantum capacitance. It can be seen that, even though the on currents feature a maximum values in both cases, the optimum on current is found to be much larger when the quantum capacitance is neglected, and the corresponding ideal effective mass is found lower. This demonstrates that, even if SDT is the main cause of on current degradation for excessively light effective masses, the quantum capacitance (or DOS bottleneck effect) also amplifies this degradation.

At large bandgap, there is thus no difference between the on current of a direct and an indirect material as shown in Figure 3.25 and Figure 3.26, since BBT has been found

negligible compared to SDT in these conditions. This is obviously no longer true in alternative channel material with lower bandgap.

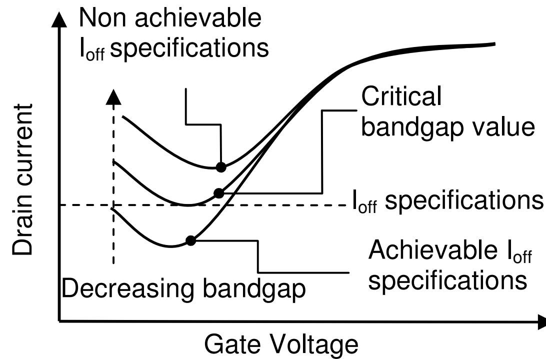

Figure 3.27 : Scheme of the drain current for different energy bandgap at same transport effective mass. The critical bandgap is defined as the bandgap value where the minimum leakage current I_{off_min} (defined by both SDT and BBT currents) becomes higher than the ITRS specification.

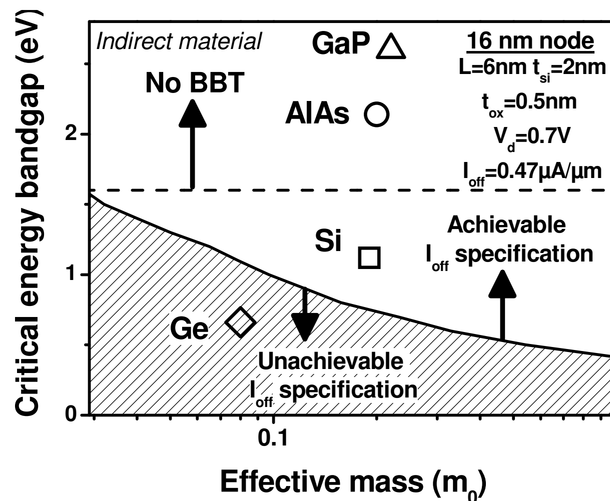

Figure 3.28 : Critical energy bandgap as a function of the effective mass, showing the range of effective mass and bandgap for which the off current ITRS specification for the 16nm node cannot be achieved. The plot has been done for semiconductor with indirect bandgap.

As explained in Figure 3.27, for a given effective mass, there is a critical energy bandgap value below which the minimum off current achievable I_{off_min} exceed the ITRS specification due to too large BBT contributions. This critical energy bandgap is plotted versus transport effective mass for indirect gap material in Figure 3.28. Devices have been designed according to the 16 nm technological node requirements. Three different zones can be identified in this plot :

- The patterned one, below the curve, is the area where the effective masses and bandgaps are too small to meet the off state specification (due to too large BBT).
- In the second one, above the curve and below the dashed line, is the area where BBT is weak enough to ensure a minimum achievable off current smaller than the ITRS specification.
- In the third one, above the dashed line, i.e for gap higher than 1.6eV and for the considered drain bias of 0.7V, is the area where BBT is totally suppressed due to the absence of

equivalent energy states in the valence and the conduction band to allow the tunneling process (the energy bandgap is too high compared to the supply voltage, BBT can not occur).

The coordinate (m_t, E_g) in this plot corresponding to germanium, silicon, AlAs and GaP has been indicated. These results suggest for instance that BBT is likely to be a severe issue in Ge device, preventing to achieve the ITRS roadmap specifications, as already reported in [CantIEDM07]. (Note however that the beneficial impact of quantum confinement in reducing BBT [SaraVLSI07], [PethIEDM05],[KimSISPAD07]) has not be includied in this simple approach).

In the case of direct material, the impact of BBT appears to be significantly weaker. Figure 3.29 shows the relative contribution of BBT with respect to the total off current as a function of the effective mass in direct and indirect materials. Following [FiscTED07], it shows that, at same effective mass and bandgap, BBT generation rates are higher in indirect materials than in direct one. This result has been attributed in [FiscTED07] to the larger density of states typically available in the conduction band of indirect materials, compared to direct material.

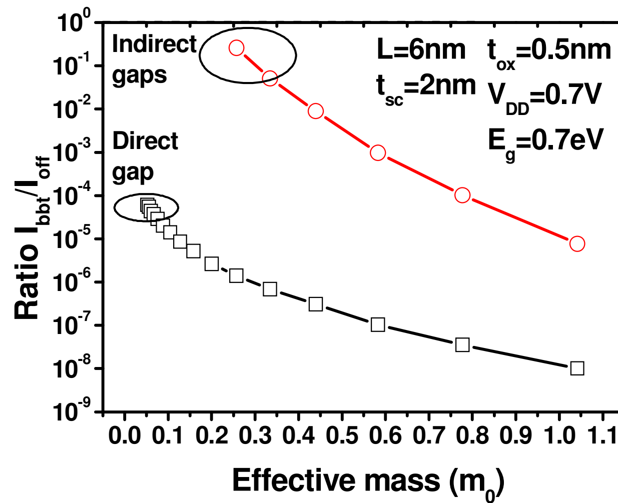

Figure 3.29 : Ratio of the BBT current in direct and indirect material on total I_{off} versus effective mass and different E_g, after Φ_{ms} adjustment. In the case of direct material, the BBT is found negligible whatever the value of m_t or Eg.

Finally, the relative contribution of thermionic current (enhanced by SCEs), SDT and BBT with respect to the total off current are compared on Figure 3.30 for an indirect channel with constant and moderate effective mass and bandgap. It shows that, for gate length from 20nm down to 4 nm, SDT dominates subthreshold leakages, while the contribution of SCEs over the total off current is reduced with reduced channel length (Note that in this plot, the body thickness t_{sc} is scaled down for each gate length, to keep SCEs under control, according to the t_{sc} = L/3 ratio). BBT, although becoming more and more significant as the gate length is scaled down, remains negligible compared to SDT in this particular case.

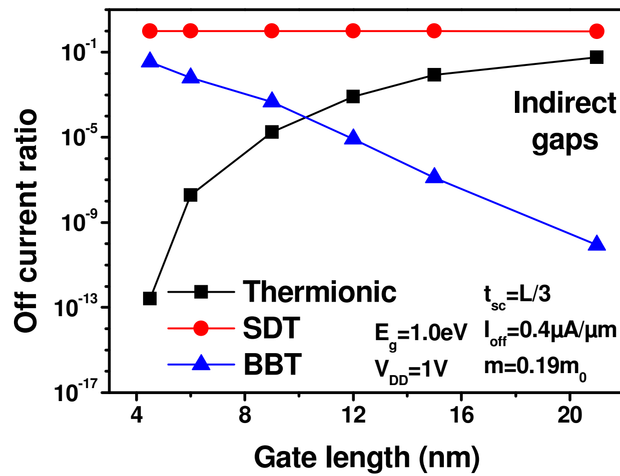

Figure 3.30 : Ratio of thermionic (+SCEs), SDT and BBT current on the total I_{off} versus gate length. SDT overcomes other leakage mechanisms in the end of the roadmap.

3.3.2.3 Conclusions

Simple models have been proposed in this work in an attempt to clarify the advantages and drawbacks of alternative channel materials for end of the roadmap CMOS application. This simplified approach has made possible to examine the qualitative impact of effective masses and bandgaps on ballistic transport, quantum capacitance, Source-to-Drain Tunneling (SDT) and Band-to-Band Tunneling (BBT) mechanisms.

Extremely small effective masses (below 0.1 m_0) have been found to severely enhance SDT in devices with channel length lower than 15 nm, which is the case, according to the ITRS roadmap, of the last High Performance nodes (22 nm and 16 nm nodes and beyond). BBT has also been found enhanced in small effective mass materials, and appears to be particularly detrimental in indirect bandgap materials with both small effective masses and small bandgaps, such as Germanium.

The particular dependence of BBT and SDT with gate voltage and metal work function adjustments explains that SDT typically dominates leakage currents, except in the previously mentioned case where BBT is so strong that ITRS leakage requirements can no longer be fulfilled.

For channel length below 15 nm, these results suggest that, in agreement with [CantIEDM07], unless a technological solution is found to reduce SDT in the off state, alternative channel materials would probably not offer significantly enhanced I_{on}-I_{off} performances compared to conventional silicon channel.

3.4 Conclusion

This chapter aimed to evaluate the impact of source-to-drain leakage on the performances of alternative channel material devices and to compare them on a fair basis (I_{on} at same I_{off}).

In this scope, two approaches have been developed to account for the most relevant source of subthreshold leakages, i.e. thermionic current enhanced by short channel effects, direct source-to-drain tunnelling and band-to-band tunnelling:

1. A time consuming but comprehensive approach (including the effect of source and drain depletion and channel orientation) which reproduces fairly more rigorous results obtained with the NEGF simulator NanoMOS
2. A more simple but computationally efficient model, assuming single subband transport in conventional channel orientation, which also compares well with NanoMOS when devices are ultra-scaled.

These two approaches have been used in two different scopes.

The first one has been involved in the investigation of possible performance enhancement when replacing silicon as a channel material for alternative one, like Ge or GaAs. The results obtained showed that alternative channel material scalability was particularly poor due to significant source-to-drain tunnelling increase : the on state performance of such devices have even been found to be lower than conventional Si or strained-Si channel, confirming the results obtained in [CantIEDM].

The origin of this on state degradation has then been more deeply investigated using the second approach. Thanks to an improved computational efficiency, this model enabled the fast treatment of numerous configurations, and hence to consider a generic channel material, whose effective mass and bandgap was varying, instead of discrete channel material whose physical parameter were too spread to quantify and discriminate the impact of the different source of performance degradation (quantum capacitance, SCEs, SDT or BBT). It has been shown in this study that the mechanism limiting the Ion-Ioff trade off was SDT, more than BBT, except in the case of low effective mass and small bandgap indirect semiconductors where BBT has been found to be dominant. In addition, this study showed a trade-off in the effective mass reduction for moderate gap semiconductors. Also beneficial at one stage thanks to injection velocity increase, the effective mass decrease becomes detrimental for the Ion-Ioff trade off due to significant SDT increase. BBT have been found to be critical only in the case of low gap, low effective mass and indirect bandgap material.

In this framework, large gap and moderate effective mass channel material are required for device featuring gate length below 10nm. Silicon and strained-Silicon thus seems to offer in this condition a good trade off as channel material.

However, two important issues remains

1. The results presented in this chapter have been obtained considering the high performances specifications of the ITRS. In the case of LSTP devices, it could be foreseen that the degraded off condition would be even more detrimental to alternative channel. But this would require rigorous re-calculations and this problematic remains an open question.

2. The possibility that the gate length scaling could be stopped at 15nm has to be investigated, as alternative channel material could in this case outperform conventional material. Therefore, a roadmap dedicated to alternative channel material should be investigated. For these gate lengths (above 10nm), the impact of carrier scattering would be significant. This point will be studied in the following chapter.

Chapter 4 : Scattering and Quasi-Ballistic (QB) transport in alternative channel material nano-nMOSFETs

Chapter 4 : Scattering and Quasi-Ballistic (QB) transport in alternative channel material nano-nMOSFETs 97
4.1 Introduction 98
4.2 The Boltzmann Transport Equation and the Monte Carlo approach 99
4.2.1 The Boltzmann Transport Equation (BTE) 99
4.2.2 Monte Carlo (MC) solution of the BTE 101
4.3 Specificities of the Multi Subbands Monte Carlo 108
4.4 Germanium and gallium-arsenide bulk mobility 111
4.5 Germanium inversion layer mobility 115
4.5.1 The nMOS mobility issue 115
4.5.2 Monte Carlo simulation study 116
4.5.3 Inversion layer mobility in Germanium On Insulator (GeOI) nMOSFET..... 121
4.6 Quasi Ballistic transport in Ge DGFETs 123
4.6.1 The Lundstrom model of quasi-ballistic transport 123
4.6.2 Monte Carlo simulations of backscattering in Ge DGFETs........ 125
4.6.3 Results and discussion 126
4.7 Conclusions 129

4.1 Introduction

In the previous chapters, the on-state current of alternative channel material devices has been computed in the fully-ballistic approach. Even though unrealistic for silicon channel length above 10nm, this assumption could be adequate for channel material featuring higher mobility and thus higher carrier mean free path. In addition, the full ballistic transport regime provides an upper bound for device performance [LundEDL97], which therefore gives a good metric for alternative channel materials comparison. However, although these high mobility channel materials are likely to be closer to the ballistic limit than silicon channel, the impact of scattering needs to be estimated.

Indeed, the advantages of the high bulk mobilities of these materials are not granted *a priori* at the device scale. For instance, in the silicon case, carrier confinement and channel/dielectric interface roughness are known to greatly reduce the electron mobility from 1300cm²/V/s in bulk down to 650cm²/V/s in inversion layer at low effective field, and to even lower values at high fields.

Due to the small dimensions at which devices based on alternative channel material may be competitive with respect to the actual silicon technology, quasi-ballistic (QB) transport is more likely to be the prevailing operating regime. The carrier mean free path and the backscattering coefficient in silicon devices have been proven in [PalesIEDM06] to be correlated with the device effective mobility. Therefore, a high mobility implies a small mean free path and hence a high quasi ballistic current. This important result links two essentially different figures of merit for transport: the mobility which is a low field and long scale transport property, and the mean free path and the backscattering coefficient that are high field and short scale ones.

The investigation of theses points for alternative channel material involves necessarily the solution of the Boltzmann Transport Equation (BTE) to rigorously account for the impact of carrier scattering, determinant in QB transport. In this framework, the Monte Carlo method is versatile enough to be easily adapted to various device architectures, including devices with alternative channel material.

In the first section of this chapter, the Boltzmann Transport Equation, on which the Monte Carlo approach is based, will be briefly reviewed. Then, the general structure of a Monte Carlo simulator will be detailed, insisting on the main inputs of such tool, which are the bandstructure and the scattering rates, and the specific ingredients needed to handle alternative channel material.

The following second section will detail the particular examples of the Multi-Subband Monte Carlo simulator, which has been exploited in this work to account for quantum effect and non-equilibrium transport in alternative channel material.

The three last sections of this chapter will then be dedicated to the applications of the Monte Carlo method. At first, the simulation of bulk crystal mobility of germanium and gallium-arsenide will be presented. Then, the particular issue of germanium nMOS inversion layer mobility will be addressed. Finally, the quasi-ballistic transport in germanium will be presented, studying the correlation between germanium mean free path and germanium inversion layer mobility.

4.2 The Boltzmann Transport Equation and the Monte Carlo approach

This section aims to briefly present the theoretical foundation of semi-classical transport in the framework of the Boltzmann Transport Equation and its solution through the Monte Carlo method. More detailed descriptions can be found in [LundNano] regarding carrier transport, while [TomiNum] gives an extensive explanation of the Monte Carlo methods and of the implementation of the various part of a MC simulator.

4.2.1 The Boltzmann Transport Equation (BTE)

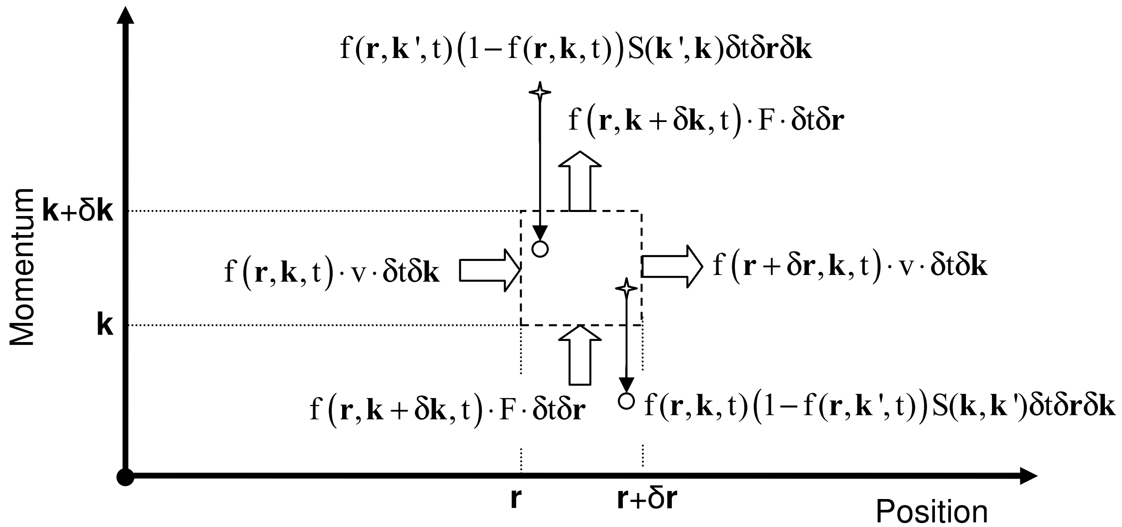

Figure 4.1 : Scheme of carrier fluxes contributing to f(**r**,**k**,t) in a two dimensional element of size δ**r**δ**k** in phase space.

The most significant information about carriers in a semiconductor device can be obtained from the distribution function in phase space (both real space and momentum space) f(**r**,**k**,t). This function corresponds to the carrier density at a position r, with a momentum p, at a time t. Many relevant quantities can be deduced from the distribution function, as for example :

- the electron density, following :

$$n(r,t) = \sum_{\mathbf{k}} f(\mathbf{r},\mathbf{k},t) \qquad (1.1),$$

where the sum over **k** adds the contribution of all possible states[5].

- Or the current density, following :

$$\vec{J}_n(\mathbf{r},t) = q\sum_{\mathbf{k}} \mathbf{v}(\mathbf{k}) f(\mathbf{r},\mathbf{k},t) \qquad (1.2),$$

where v(**k**) is the group velocity of the electron.

The distribution function is determined by solving the Boltzmann Transport Equation. This equation is based upon the carrier conservation in phase space, including the impact of carrier

[5] The sum over k is evaluated using the corresponding transformation : $\sum_{\mathbf{k_f}} f(\mathbf{k_f}) \Rightarrow \frac{\Omega}{(2\pi)^3}\int_{\Omega} f(\mathbf{k_f})d\mathbf{k}$

scattering. To establish the BTE, all mechanisms influencing f(**r**,**k**,t) must be balanced. Figure 4.1 schemes theses different mechanisms.

By definition, the variation of the number of carriers in a a two dimensional element of the phase space during a δt time is δf(r,k,t)δ**r**δ**k**. According to Figure 4.1, this term results from the difference of fluxes entering and leaving a δrδk element of phase space :

- Due to the carriers velocity, $f\left(\mathbf{r},\mathbf{k},t\right)\cdot\mathbf{v}\cdot\delta t\delta\mathbf{k}$ particles are entering the δrδk element while $f\left(\mathbf{r}+\delta\mathbf{r},\mathbf{k},t\right)\cdot\mathbf{v}\cdot\delta t\delta\mathbf{k}$ are leaving. **v** is the group velocity of the electron defined by :

$$\mathbf{v}=\frac{1}{\hbar}\nabla_{\mathbf{k}}E(\mathbf{k}) \quad (1.3)$$

  Where E(k) is the bandstructure (crystal bandstructure and applied potential).
- Due to the electric force e**F**, where **F** is the electric field applied to the carrier and since $\frac{d\mathbf{k}}{dt}=-\frac{q\mathbf{F}}{\hbar}$ particles $f\left(\mathbf{r},\mathbf{k}+\delta\mathbf{k},t\right)\cdot\frac{q\mathbf{F}}{\hbar}\cdot\delta t\delta\mathbf{r}$ are entering the δ**r**δ**k** element, while $f\left(\mathbf{r},\mathbf{k}+\delta\mathbf{k},t\right)\cdot\frac{q\mathbf{F}}{\hbar}\cdot\delta t\delta\mathbf{r}$ are leaving.
- Due to scattering, $f(\mathbf{r},\mathbf{k}',t)\left(1-f(\mathbf{r},\mathbf{k},t)\right)S(\mathbf{k}',\mathbf{k})\delta t\delta\mathbf{r}\delta\mathbf{k}$ particles are entering the δ**r**δ**k** element after scattering from a **k**' state, while $f(\mathbf{r},\mathbf{k}',t)\left(1-f(\mathbf{r},\mathbf{k},t)\right)S(\mathbf{k}',\mathbf{k})\delta t\delta\mathbf{r}\delta\mathbf{k}$ are leaving the element after a scattering with a **k'** state.

Balancing these different terms gives:

$$\begin{aligned}\delta f\delta\mathbf{r}\delta\mathbf{k}&=\left(f\left(\mathbf{r},\mathbf{k},t\right)-f\left(\mathbf{r}+d\mathbf{r},\mathbf{k},t\right)\right)\cdot\mathbf{v}\cdot\delta t\delta\mathbf{k}\\&+\left(f\left(\mathbf{r},\mathbf{k},t\right)-f\left(\mathbf{r},\mathbf{k}+d\mathbf{k},t\right)\right)\cdot\frac{q\mathbf{F}}{\hbar}\cdot\delta t\delta\mathbf{r}\\&+\cdot\sum_{\mathbf{k}'}\left(f(\mathbf{r},\mathbf{k}',t)\left(1-f(\mathbf{r},\mathbf{k},t)\right)TR(\mathbf{k}',\mathbf{k})-f(\mathbf{r},\mathbf{k},t)\left(1-f(\mathbf{r},\mathbf{k}',t)\right)TR(\mathbf{k},\mathbf{k}')\right)\end{aligned} \quad (1.4)$$

where the sum over **k'** accounts for the contribution of all possible in and out scatterings and where the (1 – f(r,k,t)) factor represents the occupation of the final state after scattering, (generally dropped by assuming available final state). In (1.4), **F** is the electric field, and **v** is the group velocity of the electron defined by :

$$\mathbf{v}=\frac{1}{\hbar}\nabla_{\mathbf{k}}E(\mathbf{k}) \quad (1.5)$$

where E(**k**) is the bandstructure, as introduced in chapter 2.

The Boltzmann Transport Equation is obtained from (1.4) by performing the limit to zero of phase space element and the time variation, leading to:

$$\begin{aligned}&\frac{\partial f}{\partial t}+\mathbf{v}\cdot\nabla_{\mathbf{r}}f+\frac{q}{\hbar}\mathbf{F}\cdot\nabla_{\mathbf{k}}f=\\&\sum_{\mathbf{k}'}\left(f(\mathbf{r},\mathbf{k}',t)\left(1-f(\mathbf{r},\mathbf{k},t)\right)TR(\mathbf{k}',\mathbf{k})-f(\mathbf{r},\mathbf{k},t)\left(1-f(\mathbf{r},\mathbf{k}',t)\right)TR(\mathbf{k},\mathbf{k}')\right)\end{aligned} \quad (1.6)$$

The BTE is intrinsically a semi-classical equation. Electrons are indeed treated as classical particles whose non-scattered motion follows Newton's law, but the scatterings probabilities of these electrons are calculated in the framework of quantum mechanical laws (using the Fermi golden rule described in 4.2.2.2.2). Consequently, quantum tunnelling processes are impossible in the framework of the BTE, since it requires treating carriers as waves and not as particles with defined position and momentum.

The direct solving of this equation for the operation of semiconductor device is rigorously possible [JungSSE93], but the formalism involved to carry it out is extremely complex. Approximated analytical solutions of the BTE are also possible (drift-diffusion or hydrodynamic models), but the assumptions made to obtain these models are too restrictive to account for far-from-equilibrium phenomenon like quasi-ballistic transport [LundEDL97], [AssaTED2002].

However, an indirect but efficient solving of the BTE is possible thanks to the Monte Carlo approach. The following subsection will describe this method.

4.2.2 Monte Carlo (MC) solution of the BTE

The Monte Carlo approach is a general method developed in the 50s to indirectly solve by statistical means complex integro-differential equation like the BTE[6]. In the case of transport in semiconductor crystal and devices, the aim of the Monte Carlo method is to determine the distribution function f(**r**,**k**,t) by simulating a large number of carrier, whose trajectories follow Newton's law of motion, and whose random scattering events follow quantum mechanical laws.

The first Monte Carlo study of transport in semiconductor has been carried out in 1966 by Kurosawa [KuroICPS66]. Unipolar device have been simulated using this technique in 1980 [ZimmSSE80]. An important review of the understanding of carrier transport in silicon and germanium during the 70s has been published in 1983 by Jacoboni and Reggiani [JacoRMP83], but so far, no semiconductor devices were simulated. The Bologna group has presented the Monte Carlo studies of MOSFET between 1986 and 1988 [SanTCADICS88]. In 1988, Fischetti and Laux developed the first full band Monte Carlo code, and in 1993 the first Multi Subband Monte Carlo. Then, many groups around the world have developed MC simulator [BuflTED00],[DollJAP97][FerrIEDM00][RavaTED86][JungSSE93]

Some improvements in the Monte Carlo techniques are still studied. In an attempt to correctly reproduce the subthreshold characteristic of MOSFET in presence of tunnelling, a Monte Carlo code solving the Wigner Transport Equation has been developed in the University of Paris Sud [QuerIEDM2006]. Recently, the first Multi Subband Monte Carlo for hole transport has been developed by the Udine's group [DeMiULIS08].

This subsection describes the common structure of Monte Carlo simulators, as well as its main inputs.

[6] The formal equivalence between the Monte Carlo method and the BTE can be established mathematically (see [LundFund]).

4.2.2.1 Principle of Monte Carlo simulations

In Monte Carlo simulators, the main macroscopic quantities are obtained from the carrier distribution function. To do so, carrier transport is simulated by the sequence of carrier ballistic free flight interrupted by scattering events. The carrier free flights obey Newton's law of motion and are therefore deterministic:

$$\frac{d\mathbf{k}}{dt} = \frac{q\mathbf{F}}{\hbar} \text{ and } \frac{d\mathbf{r}}{dt} = \mathbf{v} = \frac{1}{\hbar}\nabla E(\mathbf{k}) \tag{1.7}$$

On the contrary, scattering randomly modifies the carrier momentum, in an instantaneous process and does not change the particles positions.

Figure 4.2 illustrates a sequence of free flights and scatterings of a single carrier. This process is looped until enough statistics are gathered or until a defined time step is reached. At the end of a simulation or a time step, the statistical information on the carrier sample are collected and the macroscopic quantities are calculated from the distribution function.

Generally, Monte Carlo codes contain many more features to guarantee its physical accuracy and stability. For instance, in device simulation, self-consistency between the distribution function and the electric potential obtained from the Poisson equation is often compulsory, which add more steps in the calculation process [JungSSE93][PaleTED06].

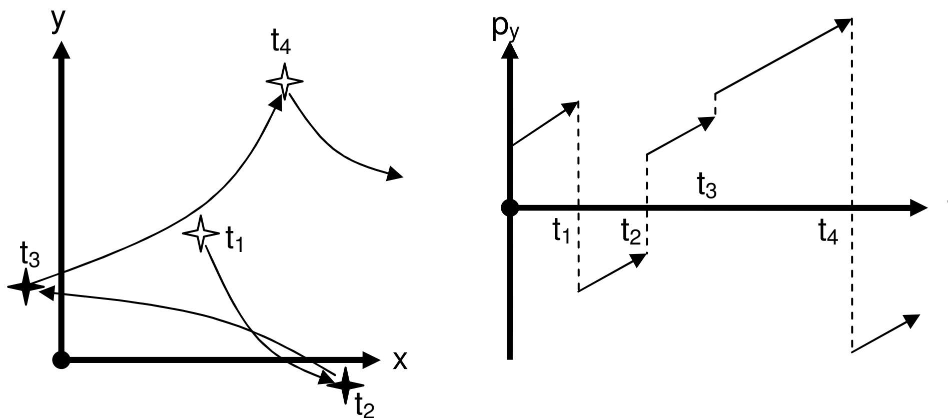

Figure 4.2 : Sketch of a single electron trajectory in a 2D real space and corresponding projection of its momentum in the y direction as function of time.

4.2.2.2 Main inputs of a MC simulator

Monte Carlo thus appeared to be a conceptually simple but robust method to solve the BTE. However, as underlined previously, this procedure requires the definition of the bandstructure and calculation of the scattering rates, which govern the free flight sequences and the frequency of the scattering event These two inputs are of primary importance to understand material properties, to reproduce experimental data and to give physically based prediction. In addition, the simulation of alternative channel material involves a careful determination of these quantities.

The following subsection will explain the role and the calculation of the bandstructure and of the scattering rates, as well as their specificities in the case of alternative channel material simulations.

4.2.2.2.1 Material bandstructure

The role of the bandstructure on the on-state full ballistic current has already been presented in Chapter 2. In Monte Carlo simulations, the bandstructure is essential as it links the carrier momentum with its energy, and hence to its scattering probability (see 4.2.2.2.2). In addition, the group velocity of the particles are deduced from the bandstructure, following equation (1.3).

In the Monte Carlo approach, the dispersion relation can be treated in the framework of the Effective Mass Approximation (EMA), like previously presented in this work in the case of the full ballistic transport, or more rigorously in full band approach [Fisc,Bandit]. This full bandstucture can be obtained thought k.p non local pseudo-potential or tight-binding calculations.

However the EMA has been used in this work for sake the of simplicity, including the impact of band non-parabolicity on transport.

It is worth noticing that the values of the effective masses used in the Monte Carlo simulation of alternative channel material (such as Ge or GaAs) slightly differ from the values commonly used in full ballistic transport modelling. Table 4.1 sums up the masses used in the literature for full ballistic transport and the one used in the literature and in this work for Monte Carlo simulations of silicon, germanium and GaAs.

		Si		Ge		GaAs	
		FB	MC	FB	MC	FB	MC
Δ	m_t (m_0)	0.19	0.19	0.2	0.288	0.19	0.43
	m_l (m_0)	0.92	0.92	0.95	1.353	1.9	
	α (eV^{-1})	–	–	–	0.3	–	0.3
Λ	m_t(m_0)	–	–	0.08	0.0815	0.127	0.17
	m_l (m_0)	–	–	1.64	1.588	1.538	
	α (eV^{-1})	–	–	–	–	–	0.5
Γ	m (m_0)	–	–	–	–	0.067	0.063
	α (eV^{-1})	–	–	–	–	–	0.62

Table 4.1 : Table of effective masses of silicon, germanium and gallium-arsenide used in the framework of full ballistic transport modeling and in the Monte Carlo simulation of this work. In the case of full ballistic transport, the silicon and germanium data are taken from [Ioffe.ru] and the GaAs one from [FiscTED91_1]. The data used in Monte Carlo for silicon and germanium are taken from [JacoRPM83] and the one for GaAs from [PozeSSE80]. It can be seen from this table that the effective mass slightly differ depending on the use. In addition, in the particular case of GaAs, the valleys are assumed spherical in the Monte Carlo approach, following [PozeSSE80][BrenSSE84][LundFund]

4.2.2.2.2 Scattering Rates

The scattering rates calculation is one of the essential steps of the Monte Carlo process, as it gives the frequency of the carrier scattering event and thus the strength of the momentum randomization. The origin, the calculation and the use of scattering rates are detailed in the following.

From a theoretical point of view, a scattering event is an interaction between a charge and a quickly varying potential which modifies the carrier momentum and in some case its energy. Each source of perturbing potential can be the origin of a scattering event. Therefore, many different types of scattering events are possible in a crystal or in a device. The most common ones are:

- Ionized impurities: they arise from a perturbing potential caused by localized charge like dopant in the crystal lattice.
- Phonons: the atoms vibrations in the crystal results in small range electric potential variation from the bandstructure deformation which can interact with carrier. The different of phonon scatterings are :
  - Elastic phonons scattering, which modifies the carrier momentum without changing its energy.
  - Inelastic phonons scattering, which modifies both carrier energy and momentum. They can in addition modify the carrier valleys. There are 3 types of inelastic phonon (see Figure 4.3) :
    - g-type intervalley, which change the carrier valley to the opposite one of the same group of valley.
    - f-type intervalley which change the carrier valley to the non-opposite one of the same group of valleys.
    - The intergroup which move the carrier to another group of valley (e.g. from Δ to Λ).

  In general, the phonon scattering rate is proportional to the density of states, so that valleys with large effective masses feature large phonon scattering rates and *vice versa*.
  Other type of phonons are possible if the crystal lattice is not composed by only one element like in the Si or Ge crystals, but of two, like in the III-V compounds case. Due to the different polarization between the two atoms, the dipole induced by the lattice vibration consequently results in additional perturbing potential inducing scatterings. These modes are called Polar Optical Phonon.
- The surface roughness: In MOS devices, at the semiconductor/insulator interface, the imperfections of planarity induce local potential variation also causing scattering.

Many other carrier scattering mechanisms are possible, remote Soft Optical phonons due to the use of strongly dipolar high-κ dielectrics, neutral defects in channel etc.

The calculation of the scattering rate is derived from the application of the Fermi Golden Rule. To calculate the scattering rates, i.e. the number of scattering per second at a given energy, the carrier are treated as waves. Before scattering, the carriers wave vector is $\mathbf{k_i}$. After scattering, i.e. after the interaction with the perturbation potential, the carrier wave vector is $\mathbf{k_f}$. In quantum mechanics, the transition rates (or probability) between an initial state i (carrier with a $\mathbf{k_i}$ wave vector) and a finial state f (carrier with a $\mathbf{k_f}$ wave vector) caused by the perturbation dsescribed by the operator V is given by:

$$\mathrm{TR}(\mathbf{k_i},\mathbf{k_f}) = \frac{2\pi}{\hbar}\left|\langle f|V|i\rangle\right|^2 \delta(E_f - E_i \pm \Delta E) = \frac{2\pi}{\hbar}\left|\int_\Omega \Psi_f \; V \; \Psi_i dr\right|^2 \delta(E_f - E_i \pm \Delta E) \quad (1.8)$$

where < i | and < f | are respectively the initial and final state, with an energy E_i and E_f, described by the Ψ_i and Ψ_f wave function. The term $\delta(E_f - E_i \pm \Delta E)$ ensures the energy conservation between the initial and final state in case of a ΔE energy exchange process (the upper symbol denotes the phonon emission and the lower one the phonon absorption).

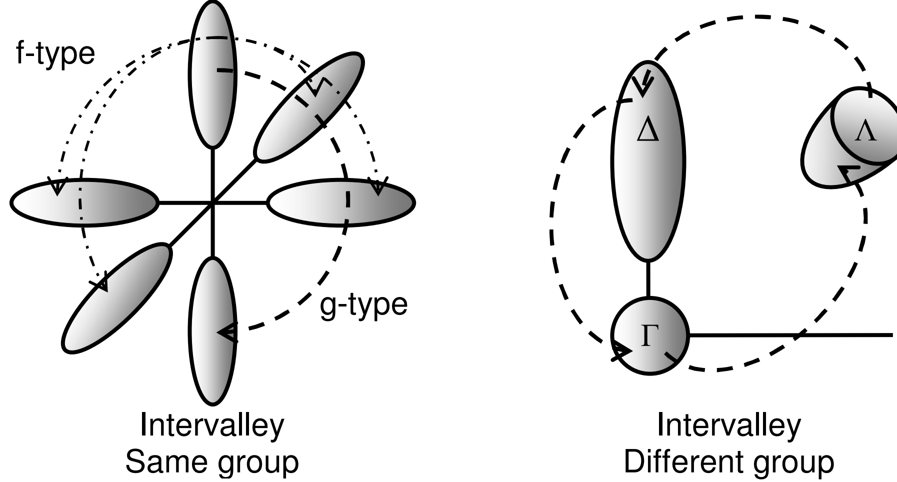

Figure 4.3 : Scheme of the intervalley optical phonons.

The total scattering rate from an initial state $\mathbf{k_i}$ is then obtained by summing the transition rate over all possible final state :

$$\mathrm{SR}(\mathbf{k_i}) = \sum_{k_f} \mathrm{TR}(\mathbf{k_i},\mathbf{k_f}) \quad (1.9)$$

Following this approach, the calculation of the scattering rates can possibly lead to simple analytical formulas. However, this is not possible in many cases and the different integrals and sums have to be carried out numerically. In the following, the Polar Optical Phonon will be used as an example of analytical scattering rate calculation.

In the 3D electron gas case, the POP perturbation potential resulting from the vibration of two different atoms link by ionic bounds is given by [LundFund]:

$$V_{POP} = \frac{q\sqrt{\hbar\omega_0}}{i\boldsymbol{\beta}\sqrt{\Omega}}\sqrt{\frac{1}{\varepsilon_\infty} - \frac{1}{\varepsilon_0}}\sqrt{N_0 + \frac{1}{2} \mp \frac{1}{2}}\, e^{\pm i\hbar\boldsymbol{\beta}\cdot\mathbf{r}} \quad (1.10)$$

where $\hbar\omega_0$ is the phonon energy, $\hbar\boldsymbol{\beta}$ the scattering wave vector, i.e. the difference between the final and initial wave vector ($\mathbf{k_f} - \mathbf{k_i} = \boldsymbol{\beta}$), ε_0 the low frequency dielectric constant of the material, and ε_∞ the one at optical frequency. N_0 the number of phonons given by the Bose-Einstein relation:

$$N_0 = \frac{1}{\exp\left(\frac{\hbar\omega_0}{k_b T}\right) - 1} \tag{1.11}$$

Thanks to the periodical properties of V_{POP} [LundFund] and assuming wave function as 3D plane waves when using equation (1.8), the POP transition rates between an initial and final state is given by:

$$\begin{aligned} TR(k_i, k_f) &= \frac{2\pi}{\hbar}\left|\int_\Omega \Psi_f^* \; V_{POP} \; \Psi_i dr\right|^2 \delta(E_f - E_i \pm \Delta E) \text{ with } \Psi_f^* = e^{-i\mathbf{k_f}\cdot\mathbf{r}} \text{ and } \Psi_i = e^{i\mathbf{k_i}\cdot\mathbf{r}} \\ &= \frac{\pi q^2 \omega_0}{\Omega \boldsymbol{\beta}^2}\left(\frac{1}{\varepsilon_\infty} - \frac{1}{\varepsilon_0}\right)\left(N_0 + \frac{1}{2} \mp \frac{1}{2}\right)\left|\int_\Omega e^{i(\mathbf{k_i} - \mathbf{k_f} \pm \boldsymbol{\beta})\cdot\mathbf{r}} dr\right|^2 \delta(E_f - E_i \pm \Delta E) \\ &= \frac{\pi q^2 \omega_0}{\Omega \boldsymbol{\beta}^2}\left(\frac{1}{\varepsilon_\infty} - \frac{1}{\varepsilon_0}\right)\left(N_0 + \frac{1}{2} \mp \frac{1}{2}\right)\delta(\mathbf{k_f} - \mathbf{k_i} \mp \boldsymbol{\beta})\delta(E_f - E_i \mp \hbar\omega_0) \end{aligned} \tag{1.12}$$

where Ω is the volume.

In equation (1.12), the $\delta(\mathbf{k_f} - \mathbf{k_i} \mp \hbar\boldsymbol{\beta})$ term refers to the momentum conservation between initial and final state, including the momentum exchange of the scattering.

The POP scattering rate is then obtained using equation (1.9):

$$SR(\mathbf{k_i}) = \pi q^2 \omega_0 \sqrt{\frac{1}{\varepsilon_\infty} - \frac{1}{\varepsilon_0}}\left(N_0 + \frac{1}{2} \mp \frac{1}{2}\right)\sum_{k_f} \frac{1}{\beta^2} \; \delta(\mathbf{k_f} - \mathbf{k_i} \mp \boldsymbol{\beta})\delta(E_f - E_i \mp \hbar\omega_0) \tag{1.13}$$

The two δ functions can be combined in a single one expressing both energy and momentum conservation as follow:

$$\delta(\mathbf{k_f} - \mathbf{k_i} \mp \boldsymbol{\beta})\delta(E_f - E_i \mp \hbar\omega_0) = \delta\left(\frac{\hbar^2\beta^2}{2m^*} \pm \frac{\hbar^2 \mathbf{k_i} \beta \cos\theta}{m^*} \mp \hbar\omega_0\right) \tag{1.14}$$

where m* is the effective mass. β and θ are define as in Figure 4.4.

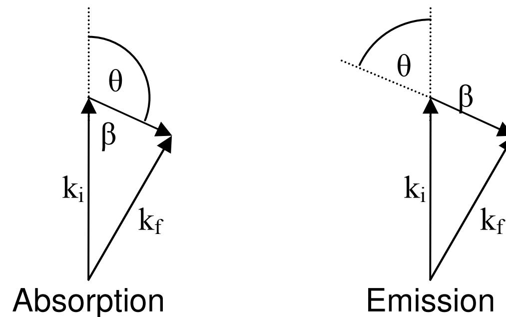

Figure 4.4 : Scheme of the initial and finial wave vector with the corresponding wave vector of scattering. θ is the angle between the initial and scattering wave vector.

The discrete sum in (1.13) is then transformed into an integral over k_f according to:

$$\sum_{\mathbf{k}_f} f(k_f) \Rightarrow \frac{\Omega}{(2\pi)^3} \int_{\Omega} f(k_f) dk \tag{1.15}$$

From (1.14) and (1.15) [LundFund],[TomiNum], the POP scattering rate can be written analytically as :

$$\mathrm{SR}(\mathbf{k_i}) = \frac{q^2 \omega_0}{4\pi\hbar\sqrt{2E(\mathbf{k_i})/m^*}} \sqrt{\frac{1}{\varepsilon_\infty} - \frac{1}{\varepsilon_0}} \left(N_0 + \frac{1}{2} \mp \frac{1}{2} \right) \ln\left(\frac{\beta_{max}}{\beta_{min}} \right)$$

$$\text{with} \tag{1.16}$$

$$\beta_{max} = \frac{\mathbf{k_i}}{\hbar} \left(1 + \sqrt{1 \pm \frac{\hbar\omega_0}{E(\mathbf{k_i})}} \right) \text{ and } \beta_{max} = \frac{\mathbf{k_i}}{\hbar} \left(\mp 1 \pm \sqrt{1 \pm \frac{\hbar\omega_0}{E(\mathbf{k_i})}} \right)$$

The next section will gives more details about the Multi Subband Monte Carlo code, which is an improvement of the common MC simulator, developed to account for quantum effect on carrier transport.

4.3 Specificities of the Multi Subbands Monte Carlo

The Multi Subbands Monte Carlo (MSMC) is the main code used in this work. It has been designed to rigorously account for quantum confinement effect on carrier transport instead of using possible correction to the 3D electron gas, as in [FerrIEDM00], [TsucIEDM00] [WinsTED03]. This section briefly details the specificities of the code.

At first, the Monte Carlo sequence is modified in the case of a MSMC code [SangESSDERC07]. The mode space approach is assumed in the transport direction, which consists in slicing the device in N sections, as shown in Figure 4.5 a). The Schrödinger equation is then solved in each of these sections, thus giving the subband leved as a function of the position along the channel. The gradient of the subbands provides the field applied (equ. (1.18)). In addition, the corresponding wave functions obtained from the Schrödinger equation solution are used to compute all scattering in each of the N sections. The electron concentration in the channel is deduced from MC sequences and wave functions, and used to calculate the potential profile using the non-linear Poisson equation. The self-consistency is obtained by looping this procedure until convergence is reached, as shown in Figure 4.5 b).

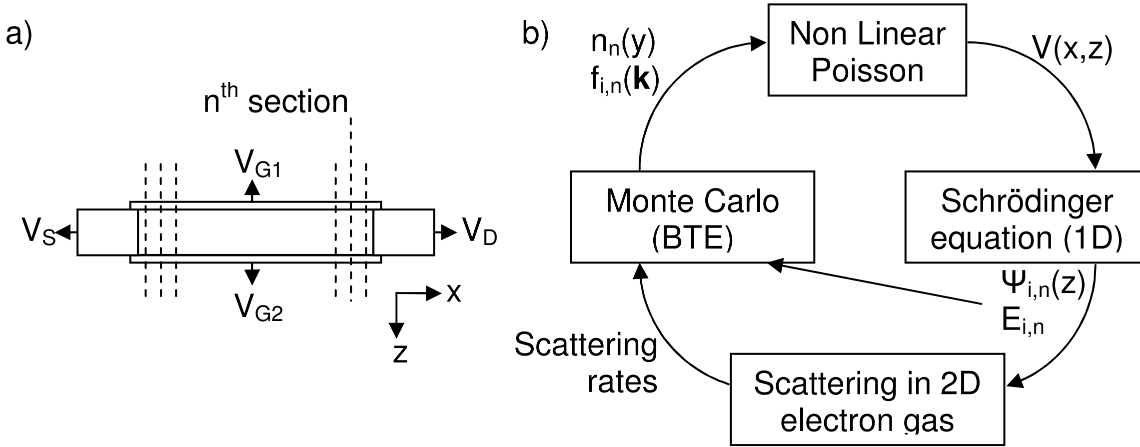

Figure 4.5 : a) Illustration of the mode space approach in the case of a DGFETs and b) flowchart of the MSMC simulator.

In the presence of quantization, the carrier momentum looses one degree of freedom and is thus described by a 2D vector in the in-plane direction (transport direction x and width direction y). The carrier vector in real space also looses one degree of freedom in the z direction, as the position is given by the presence probability of the particle related to the carrier wave function in the confinement direction. In addition, for symmetry reasons, the information on the carrier position in the width direction (y) is not relevant. Therefore, the phase space dimensions reduce to : 1 quantized dimension (z), 1 real space dimension, 2 momentum space dimensions (($\mathbf{k_x}$,$\mathbf{k_y}$), plus a subband index).

The BTE is consequently modified in presence of quantization, and becomes a set of couple BTEs describing transport in the subbands [FiscTED93],[SangESSDERC07] :

$$\begin{aligned}&\frac{\partial f_i}{\partial t}+\mathbf{v}_i\cdot\nabla_{\vec{r}}f_i+\frac{q}{\hbar}F_i\cdot\nabla_{\vec{k}}f_i=\\&\sum_{i',\vec{k}'}f_{i'}(\mathbf{r},\mathbf{k}',t)\left[1-f_i(\mathbf{r},\mathbf{k},t)\right]S_{i'i}(\mathbf{k}',\mathbf{k})-f_i(\mathbf{r},\mathbf{k},t)\sum_{i',\vec{k}'}\left[1-f_{i'}(\mathbf{r},\mathbf{k}',t)\right]S_{i\,i'}(\mathbf{k},\mathbf{k}')\end{aligned} \tag{1.17}$$

where $f_i(\mathbf{r},\mathbf{k},t)$ is the distribution function of the $(\mathbf{r},\mathbf{k})$ state in the ith subband. Rigorously, the index i should be also described as a function of the valley considered, as each valley degeneracy induces different set of subbands. It is however kept as a single index in this chapter for the sake of simplicity. In (1.17), the driving field also $\mathbf{F}_i$ differs from the 3D case and is now dependent of the gradient of the subband in the transport direction:

$$F_i = \frac{1}{q}\frac{dE_i}{dx} \quad (1.18)$$

The scattering rates calculations are also modified, as the carrier wave function cannot be considered as plane in all directions because of the quantization, but only in the two in-plane ones. In the following, the Polar Optical Phonons are used to illustrate an example of scattering rate calculation in the 2D electron gas.

The expression of the POP perturbing potential (1.10) is still valid in the 2D electron gas. The Fermi Golden rule in 2D is however used as followed.

$$\begin{aligned} &TR\left(\mathbf{k_i^{/\!/}},\mathbf{k_f^{/\!/}}\right) = \frac{2\pi}{\hbar}\left|\int_\Omega \Psi_f \; V_{POP} \; \Psi_i dr\right|^2 \delta\left(E_f - E_i \pm \Delta E\right) \\ &\text{with } \Psi_f = \frac{1}{\Omega}\psi_f(z)e^{-i\mathbf{k}_f^{/\!/}\cdot\mathbf{r}^{/\!/}} \text{ and } \Psi_i = \frac{1}{\Omega}\psi_i(z)e^{i\mathbf{k}_i^{/\!/}\cdot\mathbf{r}_{/\!/}} \end{aligned} \quad (1.19)$$

where ψ_i and ψ_f are the initial and final wave function components in the quantization direction.

Using equations (1.10) and (1.19), and noticing that in the case of a 2D electron gas, ($\boldsymbol{\beta}^2 = \boldsymbol{\beta}_{/\!/}^2 + \boldsymbol{\beta}_z^2$), with $\boldsymbol{\beta}_{/\!/}$ the in-plane scattering wave vector and $\boldsymbol{\beta}_z$ the one in the quantized direction, the transition rate becomes [PricPRB84] (note that in this case, the phonons are not quantized) :

$$\begin{aligned} TR\left(k_i,k_f\right) = &\frac{\pi q^2\omega_0}{\Omega}\left(\frac{1}{\varepsilon_\infty}-\frac{1}{\varepsilon_0}\right)\left(N_0+\frac{1}{2}\mp\frac{1}{2}\right)\times\int\left|\int\frac{1}{\left(\beta_z^{\,2}+\boldsymbol{\beta}_{/\!/}^{\,2}\right)}\psi_f(z)\psi_i(z)e^{i\beta_z\cdot z}dz\right|^2 d\beta_z\times \\ &\left|\int e^{i\left(\mathbf{k}_i^{/\!/}-\mathbf{k}_f^{/\!/}+\boldsymbol{\beta}_{/\!/}\right)\cdot\mathbf{r}_{/\!/}}d\mathbf{r}_{/\!/}\right|^2\times\delta\left(E_f-E_i\pm\Delta E\right) \end{aligned} \quad (1.20)$$

The squared integral is then parted in two integrals, following :

$$\begin{aligned} TR\left(k_i,k_f\right) = &\frac{\pi q^2\omega_0}{\Omega}\left(\frac{1}{\varepsilon_\infty}-\frac{1}{\varepsilon_0}\right)\left(N_0+\frac{1}{2}\mp\frac{1}{2}\right)\times \\ &\int\left|\int\frac{1}{\left(\beta_z^{\,2}+\boldsymbol{\beta}_{/\!/}^{\,2}\right)}\psi_f(z)\psi_i(z)e^{i\beta_z\cdot z}dz\int\frac{1}{\left(\beta_z^{\,2}+\boldsymbol{\beta}_{/\!/}^{\,2}\right)}\psi_f(z')\psi_i(z')e^{i\beta_z\cdot z'}dz\right| d\beta_z\times \\ &\delta\left(\mathbf{k}_f^{/\!/}-\mathbf{k}_i^{/\!/}\mp\boldsymbol{\beta}_{/\!/}\right)\times\delta\left(E_f-E_i\pm\Delta E\right) \end{aligned} \quad (1.21)$$

The integral over β_z is then moved inside of the double integral over space :

$$\begin{aligned} TR\left(k_i,k_f\right) = & \frac{\pi q^2 \omega_0}{\Omega}\left(\frac{1}{\varepsilon_\infty}-\frac{1}{\varepsilon_0}\right)\left(N_0+\frac{1}{2}\mp\frac{1}{2}\right)\times \\ & \left|\iint\left(\int\frac{1}{\left(\beta_z{}^2+\boldsymbol{\beta}_{//}{}^2\right)}e^{i\beta_z\cdot(z-z')}d\beta_z\right)\psi_f(z)\psi_i(z)\psi_f(z')\psi_i(z')dzdz'\right|\times \\ & \delta\left(\mathbf{k}_f^{//}-\mathbf{k}_i^{//}\mp\boldsymbol{\beta}_{//}\right)\times\delta\left(E_f-E_i\pm\Delta E\right) \end{aligned} \quad (1.22)$$

The integral over β_z is a noticeable Fourrier transform given by :

$$\int\frac{1}{\left(\beta_z{}^2+\boldsymbol{\beta}_{//}{}^2\right)}e^{i\beta_z\cdot(z-z')}d\beta_z = \frac{1}{\boldsymbol{\beta}_{//}}e^{i\beta_{//}\cdot(z-z')} \quad (1.23)$$

Consequently :

$$\begin{aligned} TR\left(k_i,k_f\right) = & \frac{\pi q^2 \omega_0}{\Omega}\left(\frac{1}{\varepsilon_\infty}-\frac{1}{\varepsilon_0}\right)\left(N_0+\frac{1}{2}\mp\frac{1}{2}\right)\times \\ & \frac{1}{\boldsymbol{\beta}_{//}}\iint\psi_f(z)\psi_i(z)\psi_f(z')\psi_i(z')e^{i\boldsymbol{\beta}_{//}\cdot|z-z'|}dzdz'\times \\ & \delta\left(\mathbf{k}_f^{//}-\mathbf{k}_i^{//}\mp\boldsymbol{\beta}_{//}\right)\times\delta\left(E_f-E_i\mp\hbar\omega_0\right) \end{aligned} \quad (1.24)$$

The ψ_i and ψ_f wave functions are obtained from 1D Schrödinger solution and cannot be expressed generally by analytical equations. To obtain the scattering rates, it consequently implies numerical calculations of the double integral in equation (1.20) (called form factor) and of the integral over all final states.

In the following sections, the MSMC code will be used to investigate the inversion layer mobility and the backscattering in germanium channel.

4.4 Germanium and gallium-arsenide bulk mobility

The preliminary step before simulating inversion layer mobility and backscattering coefficient is the calibration of the bandstructure and of the scattering rates parameters of the MSMC model. This calibration is carried out in order to reproduce experimental data of carrier average velocity as a function of the electric field in bulk material. In general, the parameters for the bandstructure are chosen to be close to the experimental value. But the scattering rates parameter must be adjusted one by one. This heavy work had already been done for many semiconductors in the 70s and 80s, so that most of the scattering parameters for these materials can be found in the literature. However, slight re-adjustments with respect to the literature are sometimes required, as the published scattering parameters apply to simulators slightly different from the one used here.

4.4.1.1 Bulk crystal mobility solver

To reproduce experimental data, a bulk crystal mobility solver is used ahead of the MSMC code. This much simpler code solves the BTE considering 0 dimensions in real space, and 3 in momentum space, as in the case of bulk crystal mobility calculation, the information on the carrier position is not relevant (infinite crystal with uniform electric field). The only useful information for the average velocity calculation is indeed carried by the momentums vectors.

Figure 4.6 and Figure 4.7 present the average carrier velocity versus electric field in germanium and gallium-arsenide, respectively, comparing the experimental and simulated data. Table 4.2 summarize the germanium and gallium-arsenide scattering rates used in this work.

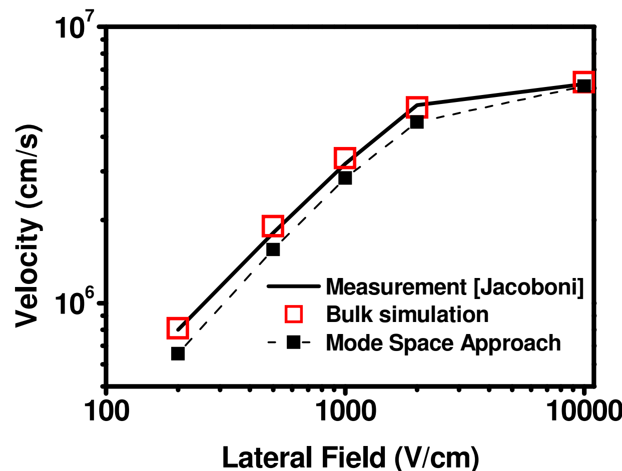

Figure 4.6 : Measured and simulated average carrier velocity as a function of the lateral electric field in Ge. The measurements are taken from [JacoRPM83]. Simulation results from the bulk mobility solver and the MSMC code where obtained using the parameters from [JacoRPM83], summed up in Table 4.1

It can be seen from Figure 4.6 that the simulation results obtained with the bulk mobility solver using the parameter in [JacoRPM83] fairly reproduce the experimental data of germanium. It also shows that Ge features a saturation velocity around 10kV/cm, lower than

in the case of silicon (7.10^6 cm/s for Ge vs. 1.10^7 cm/s for Si). The dataset of the "mode space approach" will be discussed later.

Figure 4.7 presents a different picture for GaAs. Indeed, the carrier velocity is maximum between 4 and 5kV/cm, with a large decrease for higher fields, which is responsible in some devices for negative differential resistance. This phenomenon is explained by the progressive filling of the low mobility Δ valleys (large effective mass and large DOS) in GaAs due to the increase of the electric field [BlackJAP82]. Figure 4.7 also shows that it is difficult to fit the experimental data of GaAs the bulk mobility solver than in the Ge case. Indeed, the simulations using the bandstructure and scattering parameters from [LundFund], [PozeSSE80] or [BrenSSE84] do not reproduce well enough the velocity decrease in the high field regime. Therefore, these parameters have been slightly adjusted to improve the agreement between the simulation and the measurements. The fact that slight parameters adjustments are required in the case of GaAs and not in the case of Ge can be explained by the greater complexity of intergroup phonon scatterings which govern the valleys repopulation in the high field region.

Table 4.3 compares the bandstructure and scattering parameters of GaAs found in the literature and the adjusted ones used in this work. The resulting parameter set is actually quite similar to that of [PozeSSE80]

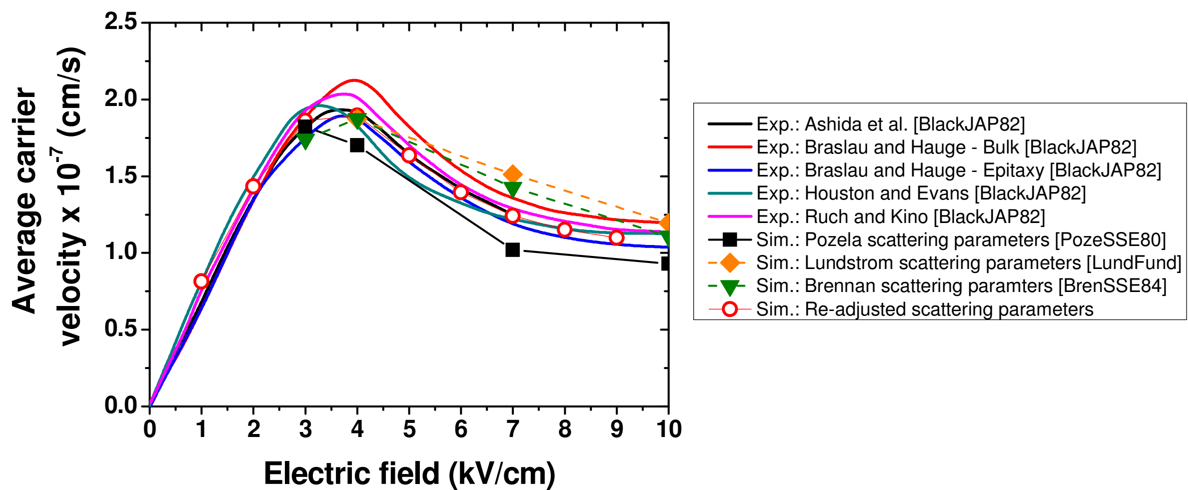

Figure 4.7 : Measured and simulated average carrier velocity as a function of the lateral electric field in GaAs. The lines correspond to measurement reviewed in [BlackJAP82], and the symbols one to simulations. It can be seen that the experimental results can not be reproduced using directly the parameters from either [LundFund] or [PozeSSE80] or [BrenSSE84]. The scattering parameters therefore need to be slightly re-adjusted to obtain a good fit on the experimental results.

<table>
<tr><td rowspan="3"></td><td colspan="3" rowspan="2">Acoustic Phonon
D_{acc} (eV)</td><td colspan="11">Optical Phonon</td><td>POP</td></tr>
<tr><td colspan="8">Intervalley
D_{op} (eV/m)
E_0 (K)</td><td colspan="3">Intergroup
D_{op} (eV/m)
E_0 (K)</td><td rowspan="2">E_0 (K)
All
valleys</td></tr>
<tr><td colspan="3"></td><td colspan="4">f-type</td><td colspan="4">g-type</td><td>Δ – Λ</td><td>Λ – Γ</td><td>Δ – Γ</td></tr>
<tr><td rowspan="2">Ge</td><td>Δ</td><td>Λ</td><td>Γ</td><td colspan="2">Δ</td><td colspan="2">Λ</td><td colspan="3">Δ</td><td>Λ</td><td rowspan="2">4.10^{10}
320</td><td rowspan="2">2.10^{10}
320</td><td rowspan="2">1.10^{11}
320</td><td rowspan="2">–</td></tr>
<tr><td>9.0</td><td>11</td><td>5</td><td colspan="2">$3.15.10^{10}$
430</td><td>$5.5.10^{10}$
430</td><td>3.10^{10}
320</td><td>$7.9.10^{9}$
100</td><td colspan="2">$9.46.10^{10}$
430</td><td>$5.5.10^{10}$
430</td></tr>
<tr><td rowspan="2">GaAs</td><td>Δ</td><td>Λ</td><td>Γ</td><td colspan="2">Δ</td><td colspan="2">Λ</td><td colspan="2">Δ</td><td colspan="2">Λ</td><td rowspan="2">1.10^{10}
347.7</td><td rowspan="2">3.10^{10}
347.7</td><td rowspan="2">1.10^{11}
347.7</td><td rowspan="2">403</td></tr>
<tr><td>7.0</td><td>7.0</td><td>7.0</td><td colspan="2">5.10^{10}
345</td><td colspan="2">5.10^{10}
345</td><td colspan="2">5.10^{10}
345</td><td colspan="2">5.10^{10}
345</td></tr>
</table>

Table 4.2 : Table of the phonon parameters, germanium and gallium-arsenide

Authors :		Lundstrom	Pozela et al.	Brennan et al.	This work
Bandstructure					
Effective mass (m_0)	Γ	0.067	0.063	0.063	0.063
	Λ	0.22	0.17	0.23	0.17
	Δ	0.58	0.58	0.43	0.58
Non parabolicity [eV^{-1}]	Γ	0.61	0.62	0.69	0.65
	Λ	0.46	0.5	0.65	0.46
	Δ	0.204	0.3	0.35	0.35
Gap 1.424 eV	Γ	+ 0	+ 0	+ 0	+ 0
	Λ	+ 0.29	+ 0.33	+ 0.33	+ 0.33
	Δ	–	+0.52	+0.52	+0.52
Scattering					
Accoustic phonon D_{acc} (eV)	Γ	7.01	7	8	7
	Λ	9.2	7	8	7
	Δ	9	7	8	7
Optical phonon D_{op} (eV/m) - $\hbar\omega_0$ (eV)	Γ	–	–	–	–
	Λ	3.10^{10} - 0.0343 1.10^{11} - 0.0290	5.10^{10} - 0.0299	1.10^{11} - 0.026	5.10^{10} - 0.0299
	Δ	7.10^{10} - 0.0299	1.10^{10} - 0.0299	9.10^{10} - 0.026	5.10^{10} - 0.0299
	Γ-Λ	1.10^{10} - 0.0278	$1.8.10^{10}$ – 0.0299	1.10^{11} – 0.026	3.10^{10} – 0.0299
	Γ-Δ	1.10^{10} - 0.0293	1.10^{11} – 0.0299	1.10^{11} – 0.026	1.10^{11} – 0.0299
	Λ-Δ	5.10^{10} - 0.0299	1.10^{11} – 0.0299	9.10^{10} – 0.026	1.10^{10} – 0.0299
Polar Optical Phonon - $\hbar\omega_0$ (eV)	Γ	0.03536	0.0362	0.0362	0.0362
	Λ			0.0343	
	Δ			0.0343	

Table 4.3 : Comparison of the bandstructure and scattering rates parameters of bulk GaAs from [LundFund], [PozeSSE80], [BrenSSE84] and this work.

4.4.1.2 Mobility calculation using a Multi Subbands Monte Carlo code

Since the bandstructure and scattering rate parameters are at first defined to reproduce crystal properties with the bulk mobility solver, and then used a different model for inversion layer (MSMC code), this latter solver reproduces the experimental data in the limit of a large quantum well with essentially negligible quantization. To do so, the velocity versus electric field is simulated in a large quantum well (thicker than 50nm). In this case, the numerous

subband levels are extremely close, so that the 2D electron gas tends to behave like a 3D electron gas.

Figure 4.6 and Figure 4.8 show the average velocity versus electric field obtained using the MSMC in the case of germanium and gallium-arsenide, respectively, using the parameters of Table 4.3. In each case, it can be seen that the MSMC simulation for a quantum well of 50 nm are in good agreement with the experimental data and the results obtained from the bulk mobility solver. However, some slight differences between the two models are noticeable. These differences can be explained by an intrinsic limitation of the mode space formalism used in the MSMC : at high electric field, and in materials whose valleys are misaligned with the transport direction (e.g. the Λ valleys of Ge and GaAs), the mode space approach impedes some transitions between the subbands which are made possible by the field. Therefore, the MSMC results (2D) fail to reproduce exactly results of the bulk mobility solver (2D). In the case of GaAs, this disagreement could be also partially due to the significant role of non-parabolicity, which is not implemented for in the subband level calculation in the MSMC model , but is accounted only in transport) [LucciTED07].

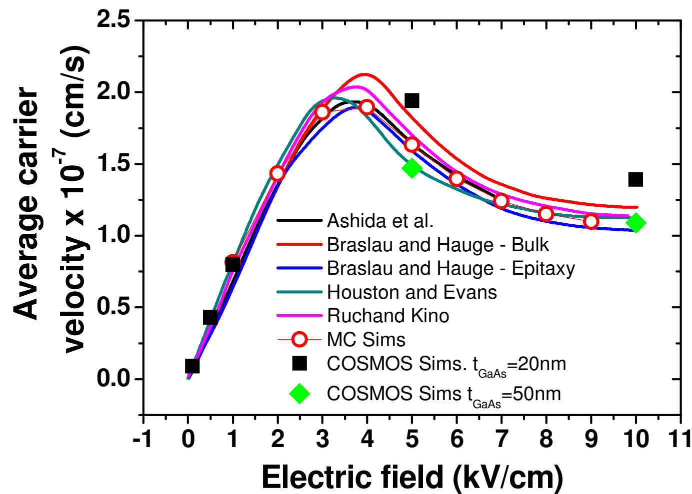

Figure 4.8 : Average carrier velocity versus electric field from experiments and simulations. The straight lines are experimental results and the scattered curves are Monte Carlo simulation. The open symbols refers to the bulk mobility MC solver, and the full symbols to the MSMC simulations obtained with COSMOS.

The effect of carrier confinement on transport is also shown in Figure 4.8 as the average carrier velocity increases significantly at high field when the width of the quantum well is reduced from 50 to 20 nm. Due to the larger splitting of the subbands in the case of a 20 nm well, the occupancy of the Γ and Λ valleys is higher than in the 50 nm one. As these valleys have higher mobility (because of small effective masses, small DOS and thus weaker phonon scattering), the overall average carrier velocity is higher. On the contrary, in the 50 nm case the subbands are close enough for the low mobility Δ valley (large DOS) to be significantly filled at the high electric field (above 5kV/cm). The carrier velocity is thus lower.

Once the scattering parameters employed by the MSMC code are checked to fairly reproduce the experimental data, the inversion layer mobility can be studied a as function of the perpendicular electric field. The next section presents the results obtained from germanium inversion layer.

4.5 Germanium inversion layer mobility

The fabrication of alternative channel material MOSFETshas always been problematic since the native oxide grown out of most semiconductor are unstable and not suitable in technology processes : for example, GeO_2 is soluble in water, and chemical degradation transform it into GeO, which is a volatile element. Therefore, the introduction of high quality dielectric deposition in CMOS steps to employ high-K material as an alternative to SiO_2, also made possible to use other channel material. The first material used to replace silicon in the channel was germanium, principally because of its high bulk electron and hole mobilities.

Even if the first germanium MOSFETs has been demonstrated in the late 80s [RansTED91], the real increase of interest for this promising technology occurred in 2001 [SaraECS01] and many references then described the fabrication of such devices. Good results have already been obtained with long channel pMOS, with hole mobility generally twice that of silicon. The fabrication of nMOS devices however seem to be an issue as the literature has not presented major performance increase with respect to silicon yet.

This fact reveals a complex question: is the Ge nMOS transport degradation due to technological reasons or to intrinsic physical limitation?

In this section, which present the results published in [RafhaySSDM07], the inversion layer mobility in n-type Ge is studied. The nMOS inversion layer mobility issue is presented in the first subsection. MSMC simulation results are then presented in the second subsection to investigate the Ge nMOSFET mobility degradation. The impact of quantization in Ge On Insulator (GeOI) on the mobility is finally described in the last subsection.

4.5.1 The nMOS mobility issue

Even though the germanium bulk crystal mobility is around 2.7 times higher than the one in silicon for electrons ($3900cm^2/m/s$ for Ge versus $1400cm^2/m/s$ for Si), no germanium channel nMOSFET has an effective mobility (i.e. an inversion layer mobility) higher than conventional silicon devices.

Figure 4.9 gather the effective mobility curves from many experimental contributions on Ge nMOSFET. To our knowledge, no recent publication presented any higher mobilities. It can be seen that all the mobility data obtained on germanium nMOSFET are below the universal Si(100) mobility curve [TakaTED94], which illustrates the transport properties degradation in these devices. This degradation has been at first attributed to higher interface state supposedly resulting from non optimized high-κ deposition on germanium. However, this assumption has been questioned, as more adequate extractions of interface state density in germanium showed more reasonable results, thus infirming the previous hypothesis [BatuINFOS06].

Consequently, there is actually no rigorous explanation of the poor effective mobility results in the case of Ge nMOSFETs. The following subsection studies the possibility of an

intrinsic physical limitation of the germanium mobility in inversion layer by mean of MSMC simulations.

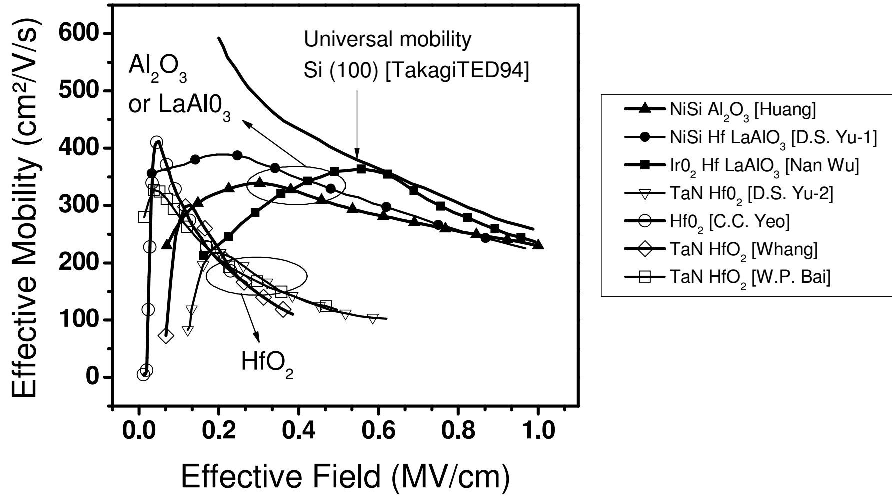

Figure 4.9 : Effective mobility as a function of the effective field (perpendicular field) of Ge n-MOSFETs. As a comparison, the universal Si(100) mobility curve is shown.

4.5.2 Monte Carlo simulation study

The inversion layer mobility can be simulated with the MSMC code using the germanium bandstructure and scattering mechanisms obtained from the calibration on experimental data (Table 4.3). Additional or modified scattering mechanisms inherent to the MOS structure are also required.

A bulk MOSFET structure is at first considered, consisting of a simple stack of a metal gate, a dielectric layer of 0.7nm equivalent SiO_2 thickness and a bulk germanium substrate. The voltage applied on the gate induces a potential well that confines the electrons at the semiconductor/insulator interface, as shown in Figure 4.10a). The effective field is defined as the average field applied to the carriers in the direction perpendicular to transport as :

$$E_{eff} = \frac{\int_0^\infty n(z)F_z(z)dz}{\int_0^\infty n(z)dz} \cong \frac{q}{\varepsilon_{si}}\left(N_{dep} + \frac{1}{2}N_{inv}\right) \tag{1.25}$$

The transport in the lateral direction results from a constant field of 1kV/cm, which prevents carriers to enter the velocity saturation regime of germanium (see Figure 4.6). The structure is sliced in 4 sections in the channel direction, whose boundaries are looped to reproduce an infinitely long device (Figure 4.10 b)).

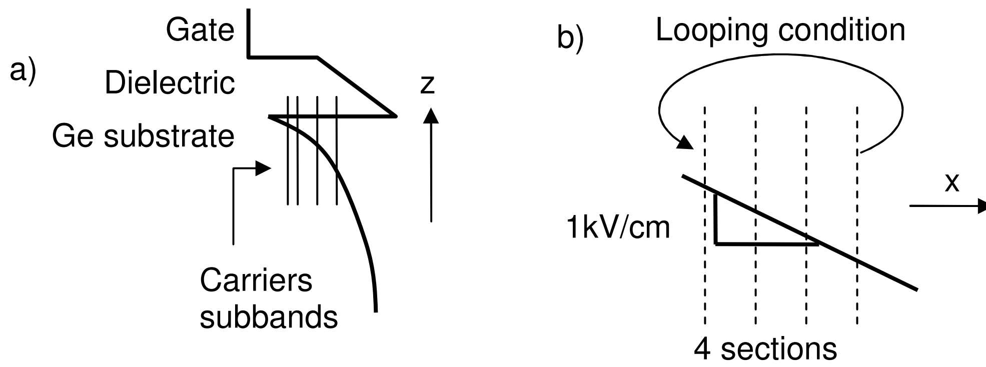

Figure 4.10 : a) Scheme of the band diagram and subbands structure in a bulk MOSFETs. b) Scheme of the looping and field condition in the "infinite" carrier transport along the semiconductor.

Figure 4.11 presents effective mobilities as function of the effective field simulated in this structure for different limiting scattering mechanisms.

The first group of results are phonon limited mobilities, accounting for all valleys or for Δ or Λ valleys only (Γ valleys plays only a negligible role in Ge). It can be seen on Figure 4.11 that the phonon limited effective mobility is significantly reduced in each case compared to the bulk mobility: from 3900cm²/V/s in bulk crystal toward 2200-2400cm²/V/s in inversion layer, and progressively decrease when the effective field is increased. If only Λ valleys are simulated, the low field inversion layer mobility is also equal to 2200-2400cm²/V/s, but the decease with the effective field is weaker. This confirms the high mobility of these valleys resulting from to their small effective mass and hence small density of states. In comparison, the decrease with the effective field when all valleys are accounted for, originates from the extremely low mobility of the Δ valleys, which are progressively filled when the effective field is increased, as shown in Figure 4.12. This low mobility is explained by the larger effective masses and DOS of these valleys (see Table 4.1).

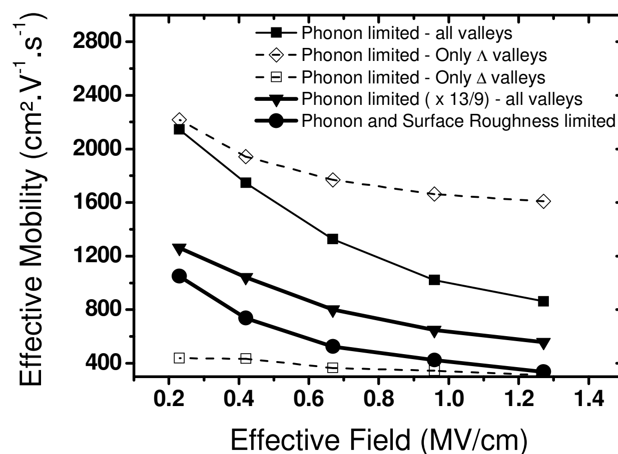

Figure 4.11 : Effective mobility as a function of the effective field for a lateral field of 1kV/cm and for different limiting scattering mechanisms.

The fact that the low field phonon limited mobilities are in each case lower than the bulk mobility, while accounting for the same phonon mechanisms, necessarily implies that this degradation is induced by carrier confinement at the semiconductor/dielectric interface. This fact therefore demonstrates the importance of a rigorous treatment of electron quantization as carried out in the MSMC in order to evaluate device transport properties.

Physical effects inherent to the MOS structure are then progressively added to the bulk germanium phonon scattering.

As a first step, we consider the issue of deformation potential for phonon scattering in inversion layer. In the case of silicon, to reproduce experimental data of effective mobility in bulk MOSFET with Monte Carlo simulation, such as the universal mobility curve [TakaTED94], it has been proved and commonly admitted by the community that the acoustic phonon deformation potentials have to be increased with respect to the value used for bulk material (around 13eV in inversion layer against 9eV in bulk) [JungSSE93]. The origin of this increase is still not fully understood. However, the same procedure has been arbitrary applied to the case of germanium inversion layer with the same factor 13/9, that is D_{acc} = 15.88 instead of 11 eV for the Λ valleys and D_{acc} = 13 instead of 9 eV for the Δ. The determination of the actual deformation potential to be used in the simulations would require an universal mobility curve in germanium nMOSFET, which is not presently available.

The new phonon limited mobility obtained is also plotted in Figure 4.11 and shows an additional degradation over the whole effective field range.

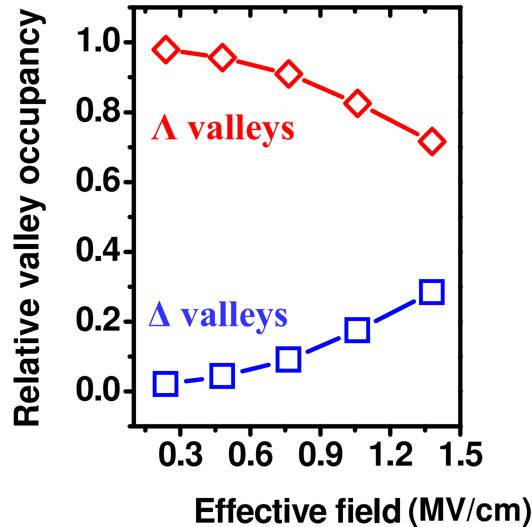

Figure 4.12 : Relative occupancy of the Λ and Δ valleys as a function of the effective field. At low field, the Λ valleys carry most of the charge, while at high field almost 30% of the charge is located in the Δ valley. This repopulation effect, already seen in chapter 2, is a consequence of the subband structure of germanium.

An important scattering mechanism inherent to the MOSFET structure is due to the surface roughness at the channel/dielectric interface. In this work, the surface roughness scattering is modelled according to [EsseTED04] in which the interface irregularities are dispersed statistically according to a Gaussian function. The parameters of this model are essentially the roots mean square value Δ_m and the correlation length L_c of the Gaussian curve, respectively set in silicon to 6.2 nm and 1.0 nm, respectively. The same parameters are kept in the case of germanium, which therefore assumes a very good interface with the dielectric layer, unlikely

in the case of high-κ deposition. The corresponding results are shown in Figure 4.11, showing a further mobility reduction with respect to the bulk value.

Although obtained with very optimistic assumptions (same increase of phonon deformation potential as in Si and very good interface as in the Si/SiO_2 case), the phonon and surface roughness limited mobility shown in Figure 4.11 corresponds to an upper physical limit of the germanium electron effective mobility. In a germanium device, it seems at first order reasonable to x 2.7 increase of the mobility with respect to silicon, because of the 2.7 ratio of the germanium and silicon bulk mobilities ($\mu_{bulkGe}/\mu_{bulkSi}$ = 2.7). Figure 4.13 compares the simulated phonon and surface roughness limited germanium mobility with the universal one in Si (100) [TakaTED94] and the "expected" germanium mobility. It can be seen that the simulation including surface roughness and quantization effects gives a mobility way below the expectation, but still higher than the silicon universal one. This mobility degradation compared to the expectation clearly results from the filling of the Δ valleys and to surface roughness.

It has to be noticed that in these simulations, ionized impurities scattering has been neglected, which therefore prevent us from observing the effective mobility decrease at low effective field.

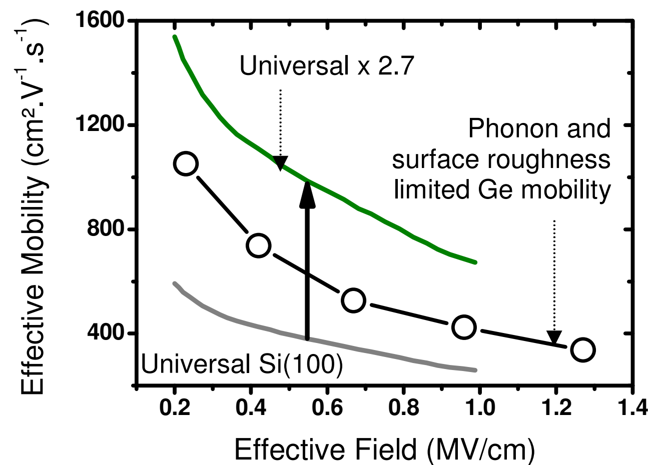

Figure 4.13 : Phonon and surface roughness germanium mobility in inversion layer as a function of the effective field, compared to the universal mobility curve in Si (100) and to the effective mobility expectation in Ge nMOS devices (universal mobility curve multiplied by $\mu_{bulkGe}/\mu_{bulkSi}$ = 2.7)

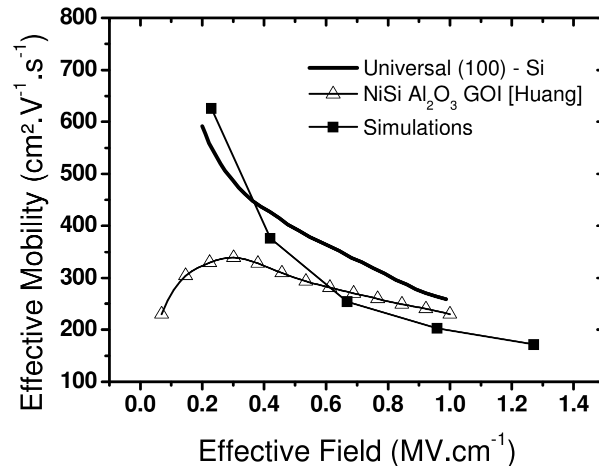

Figure 4.14 : Effective mobility as a function of the effective field for and increased surface roughness. Simulation results are close to the experimental ones, but the increase in surface roughness seems to large to be physically realistic.

In a last attempt to reproduce experimental data of effective mobility in Ge nMOSFET, the surface roughness scattering impact has been artificially increased to lower the simulation results. Figure 4.14 presents the results obtained with the increased surface roughness scattering, whose parameters have been set to Δ_m=1.1 nm and L_c=1.2nm. The results show a decreased mobility close to the measurements values, which suggest that a poor quality of the Ge/dielectric layer could be an explanation of the transport degradation in these devices. But the increase of Δ_m is significant enough to question the validity of the approach, since a 1.1nm value appears to be unphysical.

In conclusion, intrinsic physical limitations seem to play a partial role in the Ge nMOSFET mobility degradation, mainly because of the Δ valleys filling induced by quantization. However, this degradation is not significant enough to fully explain the low mobility observed experimentally, which is always lower than the silicon universal mobility curve. Therefore, it seems that technological considerations are required to explain the poor mobilities of Ge nMOSFETs. The possibility of an increased surface roughness due to a poor interface quality has been investigated, but it required unphysical parameter modification, thus questioning the validly of the approach.

A source of possible mobility degradation, not investigated in this work, could arise from the presence of a thin silicon capping layer (less than 2nm), used to improve the quality of the semiconductor/dielectric interface. Indeed, if part of the carrier are located in this layer, the resulting mobility should be lowered toward the silicon value.

Interface states and scattering modes related to charge in high-K could also be possible origins of this degradation could also degrade the mobility severely enough to explain the degradation observed experimentally.

Finally, the mobility degradation in germanium nMOSFET therefore appears to be still an open issue.

4.5.3 Inversion layer mobility in Germanium On Insulator (GeOI) nMOSFET

As mentioned in the previous chapters, the thin film architecture is a promising solutions to reduce the short channel effect in ultra-scaled devices. This architecture has also been investigated for germanium pMOSFET for example in [LeRoEDL08], showing hole mobility two times larger than in the silicon case. In this brief subsection, the mobility in thin film Ge nMOSFET is studied.

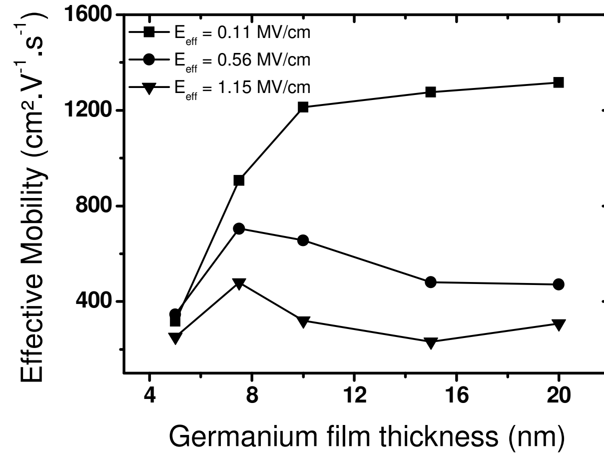

Figure 4.15 : Effective mobility as a function of the germanium film thickness for three effective fields. The lateral field used it 1kV/cm.

Figure 4.15 presents the effective mobility as a function of the thickness of the germanium layer, for three effective fields, of a GeOI structure operating in the double gate mode, whose equivalent oxide thickness is 0.7nm. The scattering mechanisms included in this simulation are the same as in the bulk case, i.e. phonon scattering (with the increased value of acoustic deformation potential) and surface roughness (on both interfaces, using the parameters of Si/SiO_2) It can be seen that the film thickness decrease induces a severe mobility degradation below 8nm. For the 0.56 MV/cm and 1.15 MV/cm effective field, the mobility features in addition a maximum around 8nm.

The mobility degradation shown in this figure has two origins :

- The phonon scattering rates are significantly increased when the film thickness reaches 5nm. This is a complex consequence of the form factor increase in the scattering rate calculation [EsseSSE04]..
- Due to confinement, the carriers progressively populate the Δ valleys as the germanium film is thinned, which has already been obtained in chapter 2 regarding germanium full ballistic DGFET. As the mobility of these valleys is low, the overall mobility is decreased with the thinning of the semiconductor film.

The maximum of mobility observed at high effective field (t_{Ge} = 8nm) is, on the contrary, a beneficial effect of the film thinning. The larger subband splitting in thinner Ge layer tends to reduce the density of states, which therefore decreases the phonon scattering rates.

These phenomena have already been measured in Silicon On Insulator devices [EsseTED04]. But in that case the mobility degradation occurs for film thickness below 5nm.

According to the present simulations, this degradation should start at around 8 nm in Ge, due to the non negligible filling of the Δ valleys. In addition, since the minimum channel length for UTB SOI or GOI is expected to be in the order of 2 or 3 time the semiconductor film thickness, this results may imply a reduced scalability of Ge UTB MOSFETs compared to Si ones.

In conclusion, even though the thin film architecture may be required to control the short channel effects, mobility degradation more severe than in the silicon case could significantly reduce the germanium device performances.

4.6 Quasi Ballistic transport in Ge DGFETs

The previous subsection has pointed out physical limitations of the germanium inversion layer mobility in both bulk and GeOI MOSFETs. It can be nevertheless objected that the mobility is not the right metric to evaluate carrier transport in germanium devices, since these formers are likely to feature sub-10nm channels length. Quasi-ballistic regime, namely a transport regime in which only few scattering events occur, is indeed more likely to occur in these ultra-scaled channels.

However, as already mentioned, a correlation between the low field mobility and the carrier mean free path has been demonstrated in silicon channels [PaleIEDM06], which implies that a low mobility leads to a low quasi-ballistic current (higher backscattering coefficient) and vice versa. Consequently, this relation has to be re-investigated in the case of germanium channels to evaluate its QB transport properties.

To this purpose, a first subsection will describe the quasi-ballistic transport in the framework of the Lundstrom model. Then, a second subsection will detail the approach used to simulate quasi-ballistic transport with the MSMC code, and in particular the backscattering coefficient and carrier mean free path calculations. The simulation results will be finally presented in the third subsection.

4.6.1 The Lundstrom model of quasi-ballistic transport

In chapter 2, the full ballistic transport regime has been treated following the Natori model as the difference of carrier fluxes in a 2D electron gas. Quasi-ballistic transport can be also described as flux differences, except that the few scatterings events contribute to the positive and negative currents in adding backscattered fluxes [LundEDL97] [LundTED02] [ClerTED06], as shown in Figure 4.16.

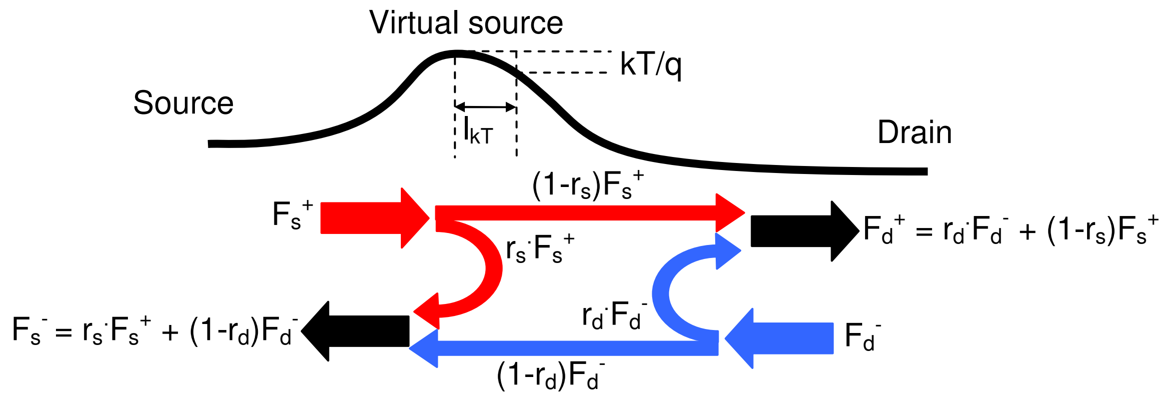

Figure 4.16 : Scheme of the electron fluxes in a MOS transistor in the quasi-ballistic regime. Contrary to the full-ballistic regime, backscattering near the source and near the drain contribute respectively to the negative and positive current. r_s and r_d are the backscattering coefficients at the source and drain respectively.

On the source side, a positive carrier flux F_s^+ is injected in the channel. Part of that flux is transmitted toward the drain ($(1\text{-}r_s) \cdot F_s^+$), while the other part is scattered back to the source ($r_s \cdot Fs^+$). The same flux repartition is found on the drain side, where a fraction of the initial

negative drain flux F_d^- is transmitted to the source ($(1-r_d)\cdot F_d^-$) and the other one backscattered to the drain ($r_d\cdot F_d^-$) – in this case, F_d is the drain flux consisting of electrons whose energy is higher than the barrier at the virtual source. In the end, the total positive flux reaching the drain and the total negative flux reaching the source are functions of the initial source and drain fluxes injected in the channel and of the backscattering coefficients ($F_d^+ = r_d\cdot F_d^- + (1-r_s)F_s^+$ and $F_s^- = r_s\cdot F_s^+ + (1-r_d)F_d^-$).

To obtain a simple analytical model of the drain current in the quasi-ballistic regime from the complex interdependence of these fluxes, some simple assumptions are made. The backscattering coefficient r_s and r_d are considered as equal. In addition, we assumes that the gate perfectly controls the charge at the top of the virtual source, i.e. $\frac{F_s^+ + F_s^-}{v_{th}} = C_{ox}(V_g - V_t)$, where v_{th} is the thermal non-degenerate velocity of an electron gas :

$$v_{th} = \sqrt{\frac{2k_b T}{\pi m^*}} \tag{1.26}$$

Assuming $F_d^- = F_s^+ e^{\frac{qV_d}{k_b T}}$ for V_d << kT/q, The following drain current equation is obtained [RenSupMicr00] [FerrThesis] :

$$I_d = W(1-r)v_{th}C_{ox}^{eff}(V_g - V_t)\frac{qV_d}{k_b T} \tag{1.27}$$

In high lateral field conditions, the contribution from the drain is neglected and the drain current in the quasi-ballistic regime can be written as [LundEDL97]:

$$I_d = W\frac{1-r_s}{1+r_s}v_{th}C_{ox}^{eff}(V_g - V_t) \tag{1.28}$$

Notice that the backscattering coefficients at high and low field are essentially different and they are in general a function of the applied bias. In addition, equations (1.27) and (1.28) assume that the backscattered flux toward the source does not modify significantly the shape of the source-drain barrier through the self-consistent potential, which should be theoretically the case. Finally, these equations also assume non-degenerate electron gas (Boltzmann distribution). If the electron gas is degenerated (Fermi-Dirac distribution), the thermal velocity v_{th} has to be replaced by the injection velocity, presented in chapter 2.

The main unknown of (1.27) and (1.28) is therefore the backscattering coefficient. In, [LundEDL97], Lundstrom gave simple expressions of the backscattering coefficient. In low field, it can be demonstrated [DattEleTran] that :

$$r_{LF} = \frac{L}{L + \lambda_{LF}} \text{ with } \lambda_{LF} = \frac{2\mu_0}{v_{th}}\frac{k_b T}{q} \tag{1.29}$$

where λ_{LF} is the carrier mean free path in low field, μ_0 the low field mobility, and L the channel length.

In the case of high field, Lundstrom intuited the following equation from Monte Carlo data and from results obtained in the framework of thermionic emission theory (Bethe Condition) :

$$r_{HF} = \frac{l_{kT}}{l_{kT} + \lambda_{HF}} \text{ with } \lambda_{LF} = \frac{2\mu_0}{v_{th}} \frac{k_b T}{q} \quad (1.30)$$

In this equation, l_{kT} is a critical length defined as the distance over which the channel potential drops by kT/q with respect to the potential at the virtual source, as shown in Figure 4.16. After this length, the scatterings in the channel do not contribute to the backscattered flux. This argument, originally applied from thermionic current, has been validated for MOSFET devices with Monte Carlo simulation, which have shown that scattering impacting the on state current indeed occur close to the virtual source [PaleTED05].

However, there is an apparent contradiction in (1.30), since μ_0 is a long distance/low field figure of merit, while λ_{HF} is a short range/high field one. In [ClercTED06], the authors attempted to give a stronger theoretical basis to the high field equations of the Lunstrom model. A more general formulation of the backscattering coefficient has been obtained in this work, unifying (1.29) and (1.30). But this unification has been carried out considering strong assumptions on the carrier distribution, and some additional work is required to fully demonstrate the correlation between λ_{HF} and μ_0.

Although not rigorously demonstrated, this correlation has been validated in silicon channels using Monte Carlo simulation in [PaleIEDM06]. The next subsection describes the procedure required to calculate the backscattering coefficient and the mean free path in low and high field with the MSMC code, in the case of germanium DGFETs.

4.6.2 Monte Carlo simulations of backscattering in Ge DGFETs

The backscattering coefficient simulations use the same bandstructure and scattering parameters as in the simulation of the inversion layer mobility (phonon and surface roughness limited mobility). As transport from source to drain needs to be accounted for in this case, the BTE solution is 1D in real space (x direction) and 2D in momentum space (k_x, k_y directions). The quantization direction (z direction) is modelled by the Schrödinger equation.

The structure simulated in this study is a symmetric germanium DGFETs, sliced by 6 sections in the transport direction, on which a constant lateral field is applied. The boundary conditions of the structure obey the rules schematized on Figure 4.17:

a) The source must behave as an electron reservoir at equilibrium. Each carrier emitted toward the channel at the source/channel contact is replaced by a carrier with the same momentum at the other side of the source.
b) If a carrier tries to enter the source from the channel, it is suppressed.
c) If a carrier reaches the left side of the source, it is re-injected on the right side with the same momentum.
d) If a carrier reaches the drain, it is suppressed (absorbing boundary).

These boundary conditions are chosen so that the drain does not emit current toward the source, neither in low nor in high field. In absence of the drain contribution, the backscattering coefficient calculation simply reduces to the ratio of the backscattered current on the total current transmitted in the channel from the source, as shown in Figure 4.17.

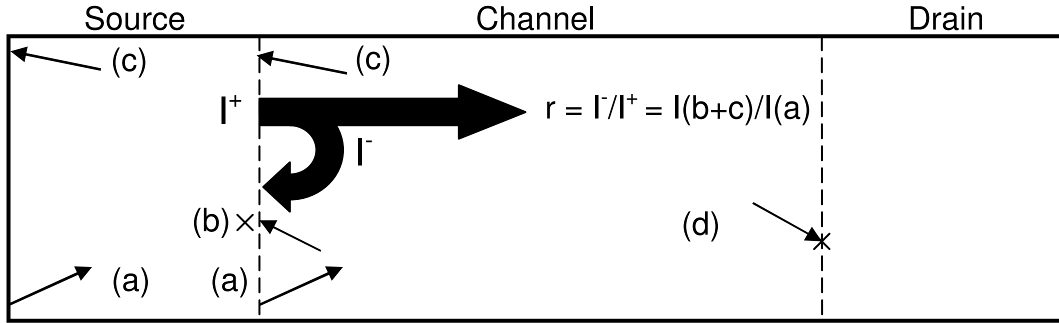

Figure 4.17 : Scheme of the boundary condition used in the simulation of the backscattering coefficient using the MSMC code. The arrows represent the carrier in-plane momentum in 2D space, and not the trajectories as transport is only 1D in this case. The plain arrows represent the current flux coming from the source. I^+ is the total current emitted from the source transmitted to the channel. I^- is the current emitted from the source and backscattered. The backscattering coefficient is then simply given by $r = I^-/I^+$.

To calculate the mean free path, the backscattering coefficient is simulated for varying gate length in the low field case or varying l_{kT} in high field. Equation (1.29) and (1.30) are then used to fit the results and to extract the mean free path in, respectively, low and high field condition.

The results obtained for Ge DGFETs following this procedure are presented in the next subsection.

4.6.3 Results and discussion

The low field backscattering coefficient has been at first simulated in Ge DGFETs, considering a null field in the lateral direction. Figure 4.18 shows the results of these simulations as a function of the device channel length, for different germanium film thickness and different effective field.

The non monotonic dependence of the backscattering coefficient with the semiconductor film thickness observed on Figure 4.18 is fully explained by the fact that the low field mobility is not monotonic with the t_{sc}, as shown in Figure 4.15. This result is a first sign of the correlation between the backscattering coefficient since the higher is the mobility for a given t_{sc}, the higher is the backscattering coefficient.

Consequently, each curve in Figure 4.18 is fitted with equation (1.29) to extract the low field carrier mean free path. The inversion layer mobilities of the DGFETs are as well simulated for the same effective field and same germanium film thickness, considering an infinite transport in the lateral direction, as carried out for the bulk and GeOI device in section 4.4. The correlation between the short channel mean free path and the long channel (considered infinite due to the looping boundaries) is shown in Figure 4.19.

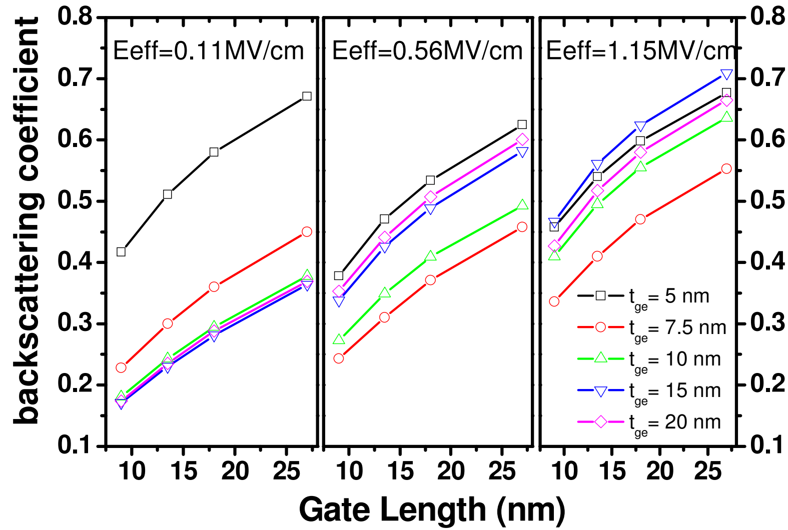

Figure 4.18 : Low field backscattering coefficient as a function of the DGFET gate length for three effective fields and five germanium film thicknesses.

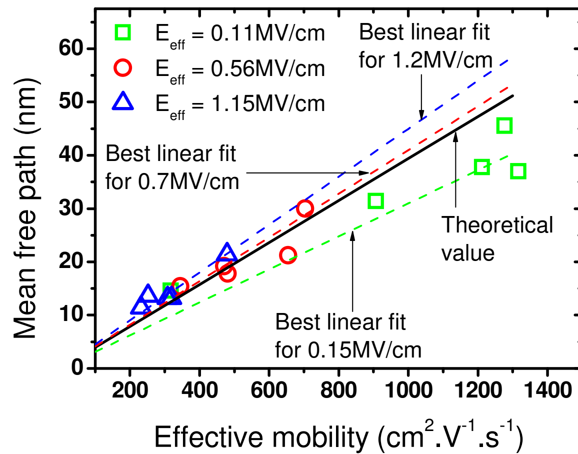

Figure 4.19 : Low field mean free path in function the effective mobility for three effective fields. For a given effective field, each point corresponds to one of the five simulated germanium film thicknesses, and hence to different effective mobility and mean free path.

It can be seen that the mean free path appears to be linearly related to the effective field. These results are also compared to the theoretical value of the mean free path given by equation (1.29). A good agreement is obtained between the MSMC simulation and the Lundstrom model. The slight difference between the simulation and the theory can be explained by the dependence of the mean free path with the level of degeneracy of the electron gas, which is not accounted for in equation (1.29).

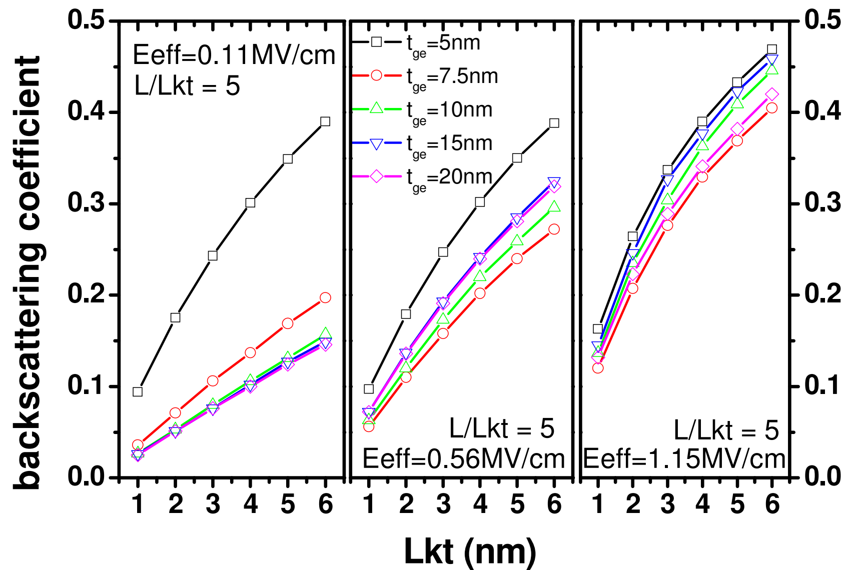

Figure 4.20 : High field backscattering coefficient as a function of kT layer length in Ge nDGFETs, for three effective fields and five germanium film thicknesses.

The same simulations have been carried out in high field conditions. In this case, the backscattering coefficient is not plotted as a function of the gate length, but as a function of the kT layer length. However, the ratio between the gate length and l_{kT} is kept constant and equal to 5 by increasing proportionally the lateral field. As in the low field case, the DGFETs are simulated at three effective fields, for five germanium film thicknesses. The results are summed up in Figure 4.20.

The mean free paths are extracted from the results presented in Figure 4.20, and correlated with the low field inversion layer mobility in Figure 4.21.

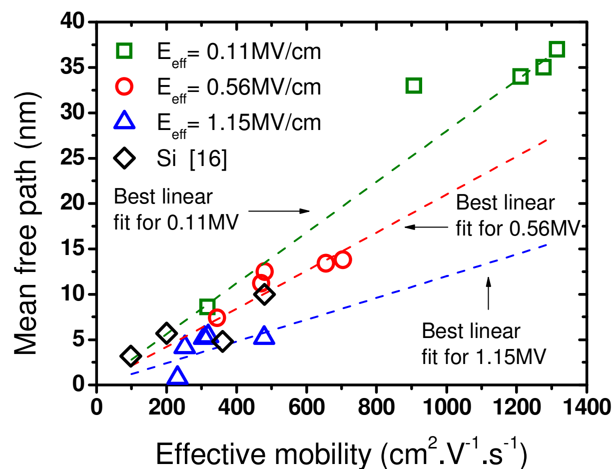

Figure 4.21 : High field mean free path in function the effective mobility for three effective fields.

Figure 4.21 demonstrates that the high field mean free path is an almost linear function of the low field effective mobility also in germanium, as in Si [PaleIEDEM06], which implies that high quasi-ballistic current could be attained only if high mobility value are obtained in n-type germanium devices.

4.7 Conclusions

This chapter has presented a study of transport in long and short channel germanium n-type (bulk, GeOI or double gate) MOSFETs. In this framework, the powerful Monte Carlo method has been used, and in particular a multi subband code which rigorously account for the effect of quantum confinement on carrier transport.

At first, the germanium nMOSFET effective mobility issue has been investigated. The results obtained with the MSMC code showed that the experimental mobility degradation in these devices cannot be explained totally by theoretical limitations. However, the filling of the low mobility Δ valleys of Ge due to the carrier quantization has been found to contribute to the mobility reduction. The ideal phonon and surface roughness limited mobilities thus obtained are lower than what could have been expected from the properties of bulk germanium.

The quasi-ballistic transport in germanium channel has also been studied, as this regime is likely to occur in ultra scaled devices. The high field carrier mean free path linearly depends with the effective mobility. This implies that high quasi-ballistic transport will only be attainable if high long channel mobilities are reached.

Chapter 5 : Conclusion

5.1 Conclusions

Alternative channel material MOSFETs have raised a large interest in the semiconductor device research community in the last five years. The replacement of silicon for high mobility material like germanium or III-V compounds, enabled by the better control of high-K dielectric deposition, have indeed been foreseen as a source of major device performance enhancement.

In the meantime, several technological realizations have been presented. Promising performances have been obtained in the case of germanium pMOSFET, GaAs nMOSFET and InGaAs nMOSFET. But up to now, these devices still feature relatively long channel length compared to the state of the art silicon technology.

However, these devices will not feature long channel dimension, as this technology will not be introduce before the 22 or even the 16nm node of the ITRS, which are likely to feature gate length below 15nm. The aim of the work presented in this thesis has thus been focused on the theoretical estimation of the performance expected by the introduction of alternative material for ultra-scaled channel.

Although this topic has been intensively explored during the last 5 years, no consensus has been reached yet, and the most promising alternative channel material has not yet been identified. This lack of consensus is partially due to the great formal difference between the approaches which have been employed to predict the device performance. As an example, the NEGF formalism is well designed to account for source-to-drain tunnelling, but it does not completely model the impact of scattering or the influence of the band-to-band tunnelling. On the contrary, the Monte Carlo approach models rigorously the scatterings in the semi-classical approximation, and can simulate band-to-band tunnelling [FiscTED07], but the inclusion of source-to-drain tunnelling is *a priori* a rather difficult task. In this work, the use of semi-analytical models enabled to account for most of the significant mechanisms impacting the alternative channel material devices: tunnelling leakage mechanisms (SDT, BBT), Short Channel Effect, Quantum capacitance degradation, injection velocity degradation, carrier degeneracy, arbitrary transport orientation.

Using these models, the full ballistic on current enhancement resulting from the replacement of silicon for Ge or other III-V materials have been investigated in chapter 2. Using a generalized semi-analytical Natori model of the full ballistic current, valid for any channel material in any orientation, it has been demonstrated that the ballistic drain current is isotropic on the (100) and (111) surface, and that it is anisotropic on the (110) surface. In addition, it has been shown that the on state current could be enhanced if the substrate and transport orientation were optimized. In this framework, the [110]/(110) have been found to be the best orientation for Ge, GaAs, InAs and InSb, whose second gap was located in the Λ valleys (the first gap being generally the Γ one). This result has been obtained previously for Ge in [LowIEDM03] and has been generalized for the first time in this work to the III-V compounds.

Moreover, , it has been shown in chapter 2, in [DeMiTED07] and in [PethIEDM05], that the increase of performances is weaker than expected at first in these devices even if the on state current has been calculated in the full ballistic limit, i.e. the upper limit of MOSFETs performances [LundEDL97]. Indeed, the injection velocity, which is the main metric of

carrier transport in the full ballistic transport regime, is degraded when subbands and valleys with high density of states are progressively filled due to the lateral field or the quantization. It appears that the higher DOS satellite valleys of Ge or III-V compounds could induce this kind of injection velocity lowering. In addition, the low DOS of the first subband could induce an increase of the quantum capacitance, which may also weaken the potentiality of such devices.

It has to be noticed that these conclusions have been obtained using the effective mass approximation and the bulk value of the effective mass of the semiconductor considered. However, due to quantization, it has been proved in the literature that the bandstructure may be strongly modified for ultra-thin semiconductor film, like the one considered in this study. Even if the conclusion on the isotropy of current on the (100) and the (111) surface are not expected to be invalidated, the anisotropy of the (110) surface could is expected to be reduced in very thin film as well as its best ballistic current value.

As underlined by the literature ([LowIEDM03], [PethIEDM05], [CantIEDM07], [FiscTED07] etc.), leakage tunnelling current constitutes an issue for the performances of alternative channel material devices. In particular, source-to-drain tunnelling and band-to-band tunnelling have been identified as the two major mechanisms contributing to the off state current. The impact of degraded subthreshold current on the overall device Ion-Ioff trade off has been investigated in chapter 3, using also semi-analytical models of the short channel effects, source-to-drain and band-to-band tunnelling current, benchmarked on more accurate simulations. Two approaches have then been proposed in this scope to 1/ compare rigorously alternative channel materials and 2/ give a deeper understanding of the results obtained.

The first approach involved the simulation of DGFETs with different semiconductors as channel material, as carried out in the literature. From this approach, it appears that the significant increase of source-to-drain tunnelling in the case of alternative channel material could induce a strong performance degradation (at constant I_{off}, taken equal to the ITRS specifications), if channel shorter than 10nm were considered. On the contrary, the Si and strained-Si channel devices have been found to be rather immune to this scalability issue. This results confirmed that obtained in [CantIEDM07], by mean of NEFG simulations (NanoMOS).

The second approach has then been dedicated to better understand the performance degradation of alternative channel material devices. For this purpose, a less rigorous but still accurate model of the off and on state current in the full ballistic regime has been developed and used to investigate the impact of the transport effective masses and bandgaps on the device performance. The performances of a DGFET have been studied as a function of the effective mass and the energy bandgap of a generic channel material, since these two material parameters have been found to impact respectively the source-to-drain and the band-to-band tunnelling leakage.

This study has shown that, if large bandgaps were considered, a trade off in the channel material effective mass was required to reach an optimized on state current (still considering a constant off current). This conclusion results from the competition of two antagonist mechanisms which are both sensitive functions of the effective mass in the transport direction. When the effective mass of the channel material is reduced, the injection velocity increases. However, a too low effective mass induces a severe increase of the source-to-drain tunnelling which degrades the off state performances, thus the overall device performance. This explains

the performance degradation observed in the case of alternative channel material with very short length, as these semiconductors generally feature small effective mass (0.08m0 for Ge, 0.067 for GaAs, 0.023 for InAs etc.).

When lower energy bandgaps have been considered, the band-to-band tunnelling leakage has been found to limit the off current to a maximum value, which could possibly exceed the ITRS requirements (no threshold voltage tuning is possible in this last case to adjust leakages).

In addition the originality of this second approach has enabled to compare the impact of source-to-drain and band-to-band tunnelling. This study has shown that in ultra-scaled devices with gate length shorter than 10nm, source-to-drain tunnelling appeared to be the dominating leakage source, overcoming band-to-band tunnelling in all case, except for small effective mass and small bandgap indirect semiconductors.

Although most of the contributions appearing in the literature have been carried out in the framework of the full ballistic transport regime, the impact of scattering in ultra-short channel is still expected to be significant, even for high mobility material. Previous studies have shown that in the case of Si that a large effective mobility should induce a short mean free path, and hence a larger quasi-ballistic current [PaleIEDM06]. This point has been re-investigated for alternative channel materials in chapter 4.

To this purpose, carrier transport in germanium inversion layer, for long and short channel devices, has been studied by means of multi subband Monte Carlo simulations. As a preliminary work, an existing Multi-Subband Monte Carlo code, required to account rigorously for carrier scattering and for the impact of quantization on transport, has been generalized to germanium and GaAs. The elastic and inelastic phonons scattering of such material have been added, and more importantly, the Polar Optical Phonon of GaAs has been re-derived (base on the work of [PricPRB84]) for the 2D electron gas.

The results obtained from these simulations in the case of germanium demonstrated at first that phonon limited mobility in inversion layer is notably degraded compared to the bulk crystal properties, mainly because of the filling of low mobility Δ valleys. Moreover, further mobility degradation has then been obtained in the case of Germanium On Insulator structure, a particular architecture expected to reduce short channel effect. In addition, it has been proven that, as in the silicon case, the carrier mean free path in ultra-scaled germanium devices is almost a linear function of the low field mobility. Consequently, high quasi-ballistic transport performances are attainable only if high mobility value are achieve in germanium, which appears demanding with respect to the state of the art technology for nMOSFET.

In conclusion, the different results presented in this thesis draw a more complex picture of the performance enhancement expected from the replacement of silicon for a high mobility semiconductor. The off state leakages are extremely penalizing in alternative channel device, which degrades significantly their I_{on}-I_{off} performance. In addition, the good transport properties (such as mobility) of alternative channel material in bulk crystal have not been found necessarily correlated with transport properties in inversion layer. In both full and quasi-ballistic transport regimes, this degradation is partially due to the filling of valleys featuring poor transport properties.

Based on these theoretical results, we may therefore think that the remarkable performance enhancement obtained experimentally for long channel nMOSFETs is unlikely to be maintained at ultra-short dimensions.

5.2 Outlook

This work has tried to be as comprehensive as possible with respect to the different mechanisms impacting the alternative channel material devices performances. However, two relevant points have still to be accounted for:

1. The impact of the band modification in presence of strong quantum confinement should be included in the simulation. This effect has been shown in Ge and InSb to reduce the ballistic drain current compared to the results obtained with the bulk effective mass value.

2. The impact of the backscattering should also be included to the simulation, as it has been proved in this work that high mobility material might provide larger quasi-ballistic current.

However, these improvement are not expected to change the overall conclusion, which is that source-to-drain tunnelling, more than band-to-band tunnelling, strongly penalize the I_{on}-I_{off} trade of in alternative channel material device featuring gate length smaller than 15 nm. For this reason, it may be relevant to propose an alternative roadmap for these devices, assuming gate length larger than 15 nm. En if this solution will of course not further improve the integrated circuit density, alternative channel material devices may in this case offer improved I_{on}-I_{off} performances compared to the silicon technology.

Publication of the author

Articles in international journals

- **Quentin Rafhay**, Raphaël Clerc, George Pananakakis and Gérard Ghibaudo, *“Impact of Source-to-Drain and Band-to-Band Tunneling on the performances of Alternative Channel Material Balistic MOSFETs”*, IEEE Transactions On Electron Devices. **Submitted**

- **Quentin Rafhay**, Raphaël Clerc, Gérard Ghibaudo and Georges Pananakakis*,"Effect of Source to Drain Tunnelling on the Scalability of Arbitrary Oriented Alternative Channel Material nMOSFETs"*, Solid State Electronics, Volume 52, Issue 10, Pages 1474-1481, October 2008

- **Quentin Rafhay**, Raphaël Clerc, Marlène Ferrier, Georges Pananakakis and Gérard Ghibaudo, *“Impact of Channel Orientation on Ballistic Current of nDGFETs with Alternative Channel Materials”*, Solid State Electronics, Volume 52, Issue 4, Pages 540-547, April 2008

- M. Ferrier, R. Clerc, L. Lucci, **Q. Rafhay**, G. Pananakakis, G. Ghibaudo, F. Boeuf, and T. Skotnicki, *"Conventional Technological Boosters for Injection Velocity in Ultra Thin Body MOSFETs"*, IEEE Transactions on Nanotechnology, Volume 6, Issue 6, Page(s):613 – 621, Nov. 2007

- Andreas Tsormpatzoglou, Charalabos A. Dimitriadis, Raphaël Clerc, **Quentin Rafhay**, G. Pananakakis, and Gérard Ghibaudo, *"Semi-Analytical Modeling of Short-Channel Effects in Si and Ge Symmetrical Double-Gate MOSFETs",* IEEE Transactions On Electron Devices, Vol. 54, No. 8, August 2007

Presentations in international conferences

- **Quentin Rafhay**, Raphaël Clerc, George Pananakakis and Gérard Ghibaudo, *“Source-to-Drain Vs. Band-to-Band Tunneling in Ultra-Scaled nDGFETs ,* Solid State Devices and Materials, 23-25 September 2008 Ibaraki, Japan

- **Quentin Rafhay**, Raphaël Clerc, George Pananakakis and Gérard Ghibaudo, *“Estimations of the Ion-Ioff Performances of Nano nMOSFETs with Alternative Channels Materials*”, EuroSOI International Workshop, 23-35 janvier 2008, Cork, Ireland.

- **Quentin Rafhay**, Raphaël Clerc, Gérard Ghibaudo and Georges Pananakakis, *“Impact of Source to Drain Tunneling on the Ion/Ioff trade-off of Alternative Channel Material MOSFETs”*, International Semiconductor Device Research Symposium, 12-14 décembre 2007, College Park, MD, USA

- R. Clerc, P. Palestri, **Q. Rafhay**, M. Ferrier, G. Pananakakis, G. Ghibaudo & L. Selmi, *“Quasi Ballistic Transport In Advanced Mosfet Devices",* CAS 2007 15 – 17 octobre 2007, Sinaia, Roumania, p. 35

- **Q. Rafhay**, P. Palestri, D. Esseni, R. Clerc and L. Selmi*, “Mobility and Backscattering in Germanium n-type Inversion Layers”, ,* Solid State Devices and Materials, 18-21 septembre 2007, Ibaraki, Japan

- R. Clerc, **Q. Rafhay**, M. Ferrier, P. Palestri, G. Ghibaudo, L. Selmi, *"Technology Oriented Analytical Models of MOSFETs in the Quasi Ballistic Regime*", Solid State Devices and Materials, 18-21 septembre 2007, Ibaraki, Japan

- M Ferrier, R. Clerc, **Q. Rafhay**, F. Daugé, G. Ghibaudo, F. Boeuf, T. Skotnicki, *“Injection Velocity Optimization in Quasi-Ballistic Si-nMOSFETs”*, SNW 2006 Silicon Nanoelectronics Workshop, Honolulu, USA, Juin 2006

- **Quentin Rafhay**, Raphaël Clerc, Marlène Ferrier and Gérard Ghibaudo, *“Further Investigations of the Impact of Channel Orientation on Ballistic Current of nDGFETs with Alternative Channel Materials”*, International Conference on Ultimate Integration on Silicon, 15-16 mars 2007, Leuven, Belgium

Bibliography

[AssaTED00] F. Assad, Z. B. Ren, D. Vasileska, S. Datta, and M. Lundstrom, "On the performance limits for Si MOSFET's: A theoretical study," *IEEE Transactions on Electron Devices,* vol. 47, pp. 232-240, 2000.

[BaccTED82] G. Baccarani, M. R. Wordeman, and R. H. Dennard, "GENERALIZED SCALING THEORY AND ITS APPLICATION TO A 1/4 MICRON MOSFET DESIGN," *Ieee Transactions on Electron Devices,* vol. 29, pp. 1660-1661, 1982.

[Berkeley] Berkeley Device group [Online] Available at www.device.eecs.berkeley.edu/qmcv/html

[BuflTED00] F. M. Bufler, A. Schenk, and W. Fichtner, "Efficient Monte Carlo device modeling," *Ieee Transactions on Electron Devices,* vol. 47, pp. 1891-1897, 2000.

[BaiEDL06] W. P. Bai, N. Lu, A. Ritenour, M. L. Lee, D. A. Antoniadis, and D. L. Kwong, "Ge n-MOSFETs on lightly doped substrates with high-kappa dielectric and TaN gate," *Ieee Electron Device Letters,* vol. 27, pp. 175-178, 2006.

[BatuJAP07] P. Batude, X. Garros, L. Clavelier, C. Le Royer, J. M. Hartmann, V. Loup, P. Besson, L. Vandroux, Y. Campidelli, S. Deleonibus, and F. Boulanger, "Insights on fundamental mechanisms impacting Ge metal oxide semiconductor capacitors with high-k/metal gate stacks," *Journal of Applied Physics,* vol. 102, 2007.

[BlackJAP82] J. S. Blackmore, "Semiconductor and other major properties of Gallium Arsenide", *Journal of Applied Physics*, vol 53, pp 123-181, 1982

[BrenSSE84] K Brennan, K. Hess, "High field transport in GaAs, InP and InAs", *Solid-State Electronics* Volume 27, Issue 4, , April 1984, Pages 347-357.

[CantIEDM06] K.D. Cantley , Y. Liu, H. S. Pal, T. Low, S.S. Ahmed, M.S. Lundstrom, "Performance Analysis of Ill-V Materials in a Double-Gate nano-MOSFET", *IEDM Tech. Dig.*, pp. 113-116, 2007

[ClerJAP02] R. Clerc, A. Spinelli, G. Ghibaudo, and G. Pananakakis, "Theory of direct tunneling current in metal-oxide-semiconductor structures," *Journal of Applied Physics,* vol. 91, pp. 1400-1409, 2002.

[ClerTED06] R. Clerc, P. Palestri, and L. Selmi, "On the physical understanding of the kT-layer concept in quasi-ballistic regime of transport in nanoscale devices," *IEEE Transactions on Electron Devices,* vol. 53, pp. 1634-1640, 2006.

[CuraSSE04] Curatola G, Fiori G and Iannaccone "G. Modelling and simulation challenges for nanoscale MOSFETs in the ballistic limit", *Solid State Elec*; vol 48(4), pp581-5872004

[DattEleTran] Supriyo Datta, "Electronic Transport in Mesoscopic Systems", Cambridge University Press, 1997

[DeMiESSDERC05] M. De Michielis, D. Esseni, and F. Driussi, "Trade-off between electron velocity and density of states in ballistic nano-MOSFETs," *Proceedings of Essderc 2005: 35th European Solid-State Device Research Conference,* pp. 165-168, 2005.

[DeMiTED07] M. De Michielis, D. Esseni, and F. Driussi, "Analytical models for the insight into the use of alternative channel materials in ballistic nano-MOSFETs," *IEEE Transactions on Electron Devices,* vol. 54, pp. 115-123, 2007.

[DeMiULIS07] M. De Michielis, D. Esseni, P. Palestri, and L. Selmi, "A new multi subband Monte Carlo simulator for nano p-MOSFETs," *Ulis 2008: Proceedings of the 9th International Conference on Ultimate Integration on Silicon,* pp. 67-70, 2008.

[DollJAP97] P. Dollfus, "Si/Si1-xGex heterostructures: Electron transport and field-effect transistor operation using Monte Carlo simulation," *Journal of Applied Physics,* vol. 82, pp. 3911-3916, 1997.

[EsseTED04] D. Esseni, "On the modeling of surface roughness limited mobility in SOI MOSFETs and its correlation to the transistor effective field," *IEEE Transactions on Electron Devices,* vol. 51, pp. 394-401, 2004.

[EsseSSE04] D. Esseni and E. Sangiorgi, "Low field electron mobility in ultra-thin SOI MOSFETs: experimental characterization and theoretical investigation," *Solid-State Electronics,* vol. 48, pp. 927-936, Jun 2004.

[FerrTNANO07] M. Ferrier, R. Clerc, L. Lucci, Q. Rafhay, G. Pananakakis, G. Ghibaudo, F. Boeuf, and T. Skotnicki, "Conventional technological boosters for injection velocity in ultrathin-body MOSFETs," *IEEE Transactions on Nanotechnology,* vol. 6, pp. 613-621, 2007.

[FerrJJAP06] M. Ferrier, R. Clerc, G. Pananakakis, G. Ghibaudo, F. Boeuf, and T. Skotnicki, "Analytical compact model for quantization in undoped double-gate metal oxide semiconductor field effect transistors and its impact on quasi-ballistic current," *Japanese Journal of Applied Physics Part 1-Regular Papers Brief Communications & Review Papers,* vol. 45, pp. 3088-3096, 2006.

[FerrThesis] M. Ferrier, "Modélisation analytique du transport balistique etquasi-balistique dans les MOSFETs avancés" Thesis.

[FerrIEDM07] D. K. Ferry, R. Akis, and D. Vasileska, "Quantum effects in MOSFETs: Use of an effective potential in 3D Monte Carlo simulation of ultra-short channel devices," *International Electron Devices Meeting 2000, Technical Digest,* pp. 287-290, 2000.

[Ferry] D. K. Ferry, S. M. Goodnick, "Transport in Nanostructures" Cambridge University Press, 1997

[FerrIEDM00] D. K. Ferry, R. Akis, and D. Vasileska, "Quantum effects in MOSFETs: Use of an effective potential in 3D Monte Carlo simulation of ultra-short channel devices," *International Electron Devices Meeting 2000, Technical Digest,* pp. 287-290, 2000.

[FiscTED91_1] M. V. Fischetti, "MONTE-CARLO SIMULATION OF TRANSPORT IN TECHNOLOGICALLY SIGNIFICANT SEMICONDUCTORS OF THE DIAMOND AND ZINCBLENDE STRUCTURES .1. HOMOGENEOUS TRANSPORT," *IEEE Transactions on Electron Devices,* vol. 38, pp. 634-649, 1991.

[FiscTED91_2] M. V. Fischetti and S. E. Laux, "MONTE-CARLO SIMULATION OF TRANSPORT IN TECHNOLOGICALLY SIGNIFICANT SEMICONDUCTORS OF THE DIAMOND AND ZINCBLENDE STRUCTURES .2. SUBMICROMETER MOSFETS," *IEEE Transactions on Electron Devices,* vol. 38, pp. 650-660, 1991.

[FiscPhysRev93] M. V. Fischetti and S. E. Laux "Monte Carlo study of electron transport in silicon inversion layers", Physical Review B, vol. 48, pp. 2244-2274, 1993

[FiscTED07] M. V. Fischetti, T. P. O'Regan, S. Narayanan, C. Sachs, S. Jin, J. Kim, and Y. Zhang, "Theoretical study of some physical aspects of electronic transport in nMOSFETs at the 10-nm gate-length," *IEEE Transactions on Electron Devices,* vol. 54, pp. 2116-2136, 2007.

[GeTED02] L. X. Ge and J. G. Fossum, "Analytical modeling of quantization and volume inversion in thin Si-film DG MOSFETs," *IEEE Transactions on Electron Devices,* vol. 49, pp. 287-294, 2002.

[GuseMicEng01] E. P. Gusev, E. Cartier, D. A. Buchanan, M. Gribelyuk, M. Copel, H. Okorn-Schmidt, and C. D'Emic, "Ultrathin high-K metal oxides on silicon: processing, characterization and integration issues," *Microelectronic Engineering,* vol. 59, pp. 341-349, 2001.

[HillEDL07] R. J. W. Hill, D. A. J. Moran, X. Li, H. Zhou, D. Macintyre, S. Thoms, A. Asenov, P. Zurcher, K. Rajagopalan, J. Abrokwah, R. Droopad, M. Passlack, and L. G. Thayne, "Enhancement-mode GaAs MOSFETs with an In0.3Ga0.7As channel, a mobility of over 5000 cm(2)/V center dot s, and transconductance of over 475 mu S/mu m," *Ieee Electron Device Letters,* vol. 28, pp. 1080-1082, 2007.

[HuanIEDM03] C. H. Huang, D. S. Yu, A. Chin, C. H. Wu, W. J. Chen, C. X. Zhu, M. F. Li, B. J. Cho, and D. L. Kwong, "Fully silicided NiSi and germanided NiGe dual gates on SiO2/Si and Al2O3/Ge-on-insulator MOSFETs," *2003 Ieee International Electron Devices Meeting, Technical Digest,* pp. 319-322, 2003.

[HurkTED92] G.A.M. Hurkx, D.B.M. Klaassen, M.P.G Knuvers, "A new recombination model for device simulation including tunneling". *IEEE Trans. Electron Device*, vol. 39, no. 2., pp 331-338, Fev. 1992.

[Ioffe.ru] Electronic archive : New Semiconductor Materials. Characteristics and Properties [Online]. Available at http://www.ioffe.ru/SVA/NSM/

[ITRS2007] International Technology Roadmap for Semiconductor - Process Integration, Devices & Structures [Online] Available at : http://www.itrs.net/Links/2007ITRS/Home2007.htm

[IwaiMicEng02] H. Iwai, T. Ohguro, and S. Ohmi, "NiSi salicide technology for scaled CMOS," *Microelectronic Engineering,* vol. 60, pp. 157-169, 2002.

[JacoRMP83] C. Jacoboni and L. Reggiani, "THE MONTE-CARLO METHOD FOR THE SOLUTION OF CHARGE TRANSPORT IN SEMICONDUCTORS WITH APPLICATIONS TO COVALENT MATERIALS," *Reviews of Modern Physics,* vol. 55, pp. 645-705, 1983.

[JungSSE93] C. Jungemann, A. Emunds, and W. L. Engl, "SIMULATION OF LINEAR AND NONLINEAR ELECTRON-TRANSPORT IN HOMOGENEOUS SILICON INVERSION-LAYERS," *Solid-State Electronics,* vol. 36, pp. 1529-1540, 1993.

[KaneJAP61] E.O. Kane, "Theory of tunneling", J. App. Phys., Vol. 32, no. 1, pp 83-91, Jan 1961

[KeldJEPT58] L. V. Keldysh, “Behavior of non-metallic crystals in strong electric fields”, *Soviet Phyic.—JEPT*, vol. 6, no. 4, pp. 763–770, Apr. 1958.

[KrisTED06] T. Krishnamohan, D. Kim, C. D. Nguyen, C. Jungemann, Y. Nishi, and K. C. Saraswat, "High-mobility low band-to-band-tunneling strained-germanium double-gate heterostructure FETs: Simulations," *IEEE Transactions on Electron Devices,* vol. 53, pp. 1000-1009, 2006.

[KuroJPSJ66] T. Kurosawa, Journal of the Physic Society Japan, Vol 21, pp 141, 1966

[LauxIEDM04] S. E. Laux, "Simulation study of Ge n-channel 7.5 nm DGFETs of arbitrary crystallographic alignment," *IEEE International Electron Devices Meeting 2004, Technical Digest,* pp. 135-138, 2004.

[LauxTED07] S. E. Laux, "A simulation study of the switching times of 22-and 17-nm gate-length SOI nFETs on high mobility substrates and Si," *IEEE Transactions on Electron Devices,* vol. 54, pp. 2304-2320, 2007.

[LeRoEDL08] C. Le Royer, B. Vincent, L. Clavelier, J. F. Damlencourt, C. Tabone, P. Batude, D. Blachier, R. Truche, Y. Campidelli, Q. T. Nguyen, S. Cristoloveanu, S. Soliveres, G. Le Carval, F. Boulanger, T. Billon, D. Bensahel, and S. Deleonibus, "High-kappa and metal-gate pMOSFETs on GeOI obtained by Ge enrichment: Analysis of ON and OFF performances," *IEEE Electron Device Letters,* vol. 29, pp. 635-637, 2008.

[LiuTED08] Y. Liu, N. Neophytou, G. Klimeck, and M. S. Lundstrom, "Band-structure effects on the performance of III-V ultrathin-body SOI MOSFETs," *IEEE Transactions on Electron Devices,* vol. 55, pp. 1116-1122, 2008.

[LiuTED93] Z. H. Liu, C. M. Hu, J. H. Huang, T. Y. Chan, M. C. Jeng, P. K. Ko, and Y. C. Cheng, "THRESHOLD VOLTAGE MODEL FOR DEEP-SUBMICROMETER MOSFETS," *IEEE Transactions on Electron Devices,* vol. 40, pp. 86-95, 1993.

[LoliSOI05] J. Lolivier, X. Jehl, Q. Rafhay, T. Poiroux, M. Vinet, B. Previtali, M. Sanquer, F. Balestra, and S. Deleonibus, "Experimental characterization of source-to-drain tunneling in 10nm SOI devices," *2005 IEEE International Soi Conference, Proceedings,* pp. 34-35, 2005.

[LowIEDM03] T. Low, Y. T. Hou, M. F. Li, C. X. Zhu, A. Chin, G. Samudra, L. Chan, and D. L. Kwong, "Investigation of performance limits of germanium double-gated MOSFETs," *2003 IEEE International Electron Devices Meeting, Technical Digest,* pp. 691-694, 2003.

[LucciTED07] L. Lucci, P. Palestri, D. Esseni, L. Bergagnini, and L. Selmi, "Multisubband Monte Carlo study of transport, quantization, and electron-gas degeneration in ultrathin SOI n-MOSFETs," *IEEE Transactions on Electron Devices,* vol. 54, pp. 1156-1164, 2007.

[LundEDL97] M. Lundstrom, "Elementary scattering theory of the Si MOSFET," *IEEE Electron Device Letters,* vol. 18, pp. 361-363, 1997.

[LundTED02] M. Lundstrom and Z. B. Ren, "Essential physics of carrier transport in nanoscale MOSFETs," *IEEE Transactions on Electron Devices,* vol. 49, pp. 133-141, 2002.

[LundNano] M. Lundstrom, Fundamentals of Carrier Transport, Second Edition, Cambridge University Press, 2000

[LuryJAP94] S. Luryi and A. Zaslavsky, "Nonclassical devices in SOI: Genuine or copyright from III-V," *Solid-State Electronics,* vol. 51, pp. 212-218, 2007.

[OgurTED80] S. Ogura, P. J. Tsang, W. W. Walker, D. L. Critchlow, and J. F. Shepard, "DESIGN AND CHARACTERISTICS OF THE LIGHTLY DOPED DRAIN-SOURCE (LDD) INSULATED GATE FIELD-EFFECT TRANSISTOR," *Ieee Transactions on Electron Devices,* vol. 27, pp. 1359-1367, 1980.

[OkIEDM06] I. Ok, H. Kim, M. Zhang, T. Lee, F. Zhu, L. Yu, S. Koveshnikov, W. Tsai, V. Tokranov, M. Yakimov, S. Oktyabrsky, and J. C. Lee, "Self-aligned n- and p-channel GaAs MOSFETs on undoped and p-type substrates using HfO2 and silicon interface passivation layer," *2006 International Electron Devices Meeting, Vols 1 and 2,* pp. 579-582, 2006.

[NanoHub] NanoMOS Non Equilibrium Green Function device simulator [Online]. Available at www.nanohub.org

[NatoJAP94] K. Natori, "BALLISTIC METAL-OXIDE-SEMICONDUCTOR FIELD-EFFECT TRANSISTOR," *Journal of Applied Physics,* vol. 76, pp. 4879-4890, 1994.

[PalTED08] H. S. Pal, K. D. Cantley, S. S. Ahmed, and M. S. Lundstrom, "Influence of bandstructure and channel structure on the inversion layer capacitance of silicon and GaAs MOSFETs," *IEEE Transactions on Electron Devices,* vol. 55, pp. 904-908, 2008.

[PaleIEDM06] P. Palestri, R. Clerc, D. Esseni, L. Lucci, and L. Selmi, "Multi-Subband-Monte-Carlo investigation of the mean free path and of the kT layer in degenerated quasi ballistic nanoMOSFETs," *2006 International Electron Devices Meeting, Vols 1 and 2,* pp. 689-692, 2006.

[PaleTED05] P. Palestri, D. Esseni, S. Eminente, C. Fiegna, E. Sangiorgi, and L. Selmi, "Understanding quasi-ballistic transport in nano-MOSFETs: Part I - Scattering in the channel, and in the drain," *IEEE Transactions on Electron Devices,* vol. 52, pp. 2727-2735, 2005.

[PethIEDM06] A. Pethe, T. Krishnamohan, D. Kim, S. Oh, H. S. P. Wong, and K. Saraswat, "Investigation of the performance limits of III-V double-gate n-MOSFETs," *2006 International Electron Devices Meeting, Vols 1 and 2,* pp. 47-50, 2006.

[PethSISPAD04] A. Pethe, T. Krishnamohan, K. Uchida, and K. C. Saraswat, "Analytical modeling of Ge and Si double-gate(DG) NFETs and the effect of process induced variations (PIV) on device performance," *Simulation of Semiconductor Processes and Devices 2004,* pp. 359-362, 2004.

[PozeSSE80] J. Pozela and A. Reklaitis, "ELECTRON-TRANSPORT PROPERTIES IN GAAS AT HIGH ELECTRIC-FIELDS," *Solid-State Electronics,* vol. 23, pp. 927-933, 1980.

[PricPRB84] P. J. Price, "POLAR-OPTICAL-MODE SCATTERING FOR AN IDEAL QUANTUM-WELL HETEROSTRUCTURE," *Physical Review B,* vol. 30, pp. 2234-2235, 1984.

[QuerIEDM06] D. Querlioz, J. Saint-Martin, V. N. Do, A. Bournel, and P. Dollfus, "Fully quantum self-consistent study of ultimate DG-MOSFETs including realistic scattering using a Wigner Monte-Carlo approach," *2006 International Electron Devices Meeting, Vols 1 and 2,* pp. 685-688, 2006.

[RafhSSE08] Q. Rafhay, R. Clerc, M. Ferrier, G. Pananakakis and G. Ghibaudo, “Impact of Channel Orientation on Ballistic Current of nDGFETs with Alternative Channel Materials”, *Solid State Electronics*, Volume 52, pp 540-547, April 2008

[RafhSSE08_2] Q. Rafhay, R. Clerc, G. Ghibaudo and G. Pananakakis,"Effect of Source to Drain Tunnelling on the Scalability of Arbitrary Oriented Alternative Channel Material nMOSFETs", *Solid State Electronics*, Volume 52, pp 1474-1481, October 2008

[RafhSSDM08] Q. Rafhay, R. Clerc, G. Pananakakis and G. Ghibaudo, “Source-to-Drain Vs. Band-to-Band Tunneling in Ultra-Scaled nDGFETs*”, Solid State Devices and Materials*, 23-25 September 2008 Ibaraki, Japan

[RafhESoi08] Q. Rafhay, R. Clerc, G. Pananakakis and G. Ghibaudo, “Estimations of the Ion-Ioff Performances of Nano nMOSFETs with Alternative Channels Materials”, *EuroSOI International Workshop*, 23-35 January 2008, Cork, Ireland.

[RafhSSDM07] Q. Rafhay, P. Palestri, D. Esseni, R. Clerc and L. Selmi, “Mobility and Backscattering in Germanium n-type Inversion Layers”, *, Solid State Devices and Materials*, 18-21 septembre 2007, Ibaraki, Japan

[RahmIEDM03] A. Rahman, A. Ghosh, and M. Lundstrom, "Assessment of Ge n-MOSFETs by quantum simulation," *2003 IEEE International Electron Devices Meeting, Technical Digest,* pp. 471-474, 2003.

[RahmTED03] A. Rahman, J. Guo, S. Datta, and M. S. Lundstrom, "Theory of ballistic nanotransistors," *IEEE Transactions on Electron Devices,* vol. 50, pp. 1853-1864, 2003.

[RahmIEDM04] A. Rahman, G. Klimeck, T. B. Boykin, and M. Lundstrom, "Bandstructure effects in ballistic nanoscale MOSFETs," *IEEE International Electron Devices Meeting 2004, Technical Digest,* pp. 139-142, 2004.

[RahmIEDM05] A. Rahman, G. Klimeck, and M. Lundstrom, "Novel channel materials for ballistic nanoscale MOSFETs-bandstructure effects," *IEEE International Electron Devices Meeting 2005, Technical Digest,* pp. 615-618, 2005.

[RahmTED02] A. Rahman and M. S. Lundstrom, "A compact scattering model for the nanoscale double-gate MOSFET," *IEEE Transactions on Electron Devices,* vol. 49, pp. 481-489, 2002.

[RahmJAP05] A. Rahman, M. S. Lundstrom, and A. W. Ghosh, "Generalized effective-mass approach for n-type metal-oxide-semiconductor field-effect transistors on arbitrarily oriented wafers," *Journal of Applied Physics,* vol. 97, 2005.

[RajaEDL07] K. Rajagopalan, R. Droopad, J. Abrokwah, P. Zurcher, P. Fejes, and M. Passlack, "1-mu m enhancement mode GaAsN-channel MOSFETs with transconductance exceeding 250 mS/mm," *Ieee Electron Device Letters,* vol. 28, pp. 100-102, 2007.

[RansTED91] C. M. Ransom, T. N. Jackson, and J. F. Degelormo, "IIB-4 GATE-SELF-ALIGNED N-CHANNEL AND P-CHANNEL GERMANIUM MOSFETS," *IEEE Transactions on Electron Devices,* vol. 38, pp. 2695-2695, 1991.

[SangESSDERC07] E. Sangiorgi, P. Palestri, D. Esseni, C. Fiegna, and L. Selmi, "The Monte Carlo approach to transport modeling in deca-nanometer MOSFETs," *Essderc 2007: Proceedings of the 37th European Solid-State Device Research Conference,* pp. 48-57, 2007.

[SangTCADIC88] E. Sangiorgi, B. Ricco, and F. Venturi, "MOS2 - AN EFFICIENT MONTE-CARLO SIMULATOR FOR MOS DEVICES," *IEEE Transactions on Computer-Aided Design of Integrated Circuits and Systems,* vol. 7, pp. 259-271, 1988.

[SentMan] Sentaurus user guide, pp. 249

[ScheSSE93] A. Schenk, "Rigorous theory and simplified model of the band-to-band tunneling in silicon", *Solid State Electronics*, Vol. 36, no. 1, pp. 19-34, Jan 1993.

[ShahEDL08] D. Shahrjerdi, T. Rotter, G. Balakrishnan, D. Huffaker, E. Tutuc, and S. K. Banerjee, "Fabrication of self-aligned enhancement-mode In0.53Ga0.47As MOSFETs with TaN/HfO2/AlN gate stack," *Ieee Electron Device Letters,* vol. 29, pp. 557-560, 2008.

[ShanEDL04] H. L. Shang, K. L. Lee, P. Kozlowski, C. D'Emic, I. Babich, E. Sikorski, M. K. Ieong, H. S. P. Wong, K. Guarini, and N. Haensch, "Self-aligned n-channel germanium MOSFETs with a thin Ge oxynitride gate dielectric and tungsten gate," *Ieee Electron Device Letters,* vol. 25, pp. 135-137, 2004.

[SkotTED08] T. Skotnicki, C. Fenouillet-Beranger, C. Gallon, F. Baeuf, S. Monfray, F. Payet, A. Pouydebasque, M. Szczap, A. Farcy, F. Arnaud, S. Clerc, M. Sellier, A. Cathignol, J. P. Schoellkopf, E. Perea, R. Ferrant, and H. Mingam, "Innovative materials, devices, and CMOS technologies for low-power mobile multimedia," *IEEE Transactions on Electron Devices,* vol. 55, pp. 96-130, 2008.

[SterPhyRev67] F. Stern and W.E. Howard, “Properties of semiconductor surface inversion layer in the electric quantum limit”, *Physical Review B*, vol. 163, no 3, pp 816, 1967

[SterJCP70] F. Stern., Journal of Computationnal Physic, vol 56, 1970

[SunEDL07] Y. N. Sun, E. W. Kiewra, S. J. Koester, N. Ruiz, A. Callegari, K. E. Fogel, D. K. Sadana, J. Fompeyrine, D. J. Webb, J. P. Locquet, M. Sousa, R. Germann, K. T. Shiu, and S. R. Forrest, "Enhancement-mode buried-channel In0.7Ga0.3As/In0.52Al0.48As MOSFETs with high-kappa gate dielectrics," *Ieee Electron Device Letters,* vol. 28, pp. 473-475,

[TakaSSE05] S. Takagi, T. Mizuno, T. Tezuka, N. Sugiyama, S. Nakaharai, T. Numata, J. Koga, and K. Uchida, "Sub-band structure engineering for advanced CMOS channels," *Solid-State Electronics,* vol. 49, pp. 684-694, 2005.

[TakaTED94] S. Takagi, A. Toriumi, M. Iwase, and H. Tango, "ON THE UNIVERSALITY OF INVERSION LAYER MOBILITY IN SI MOSFETS .1. EFFECTS OF SUBSTRATE IMPURITY CONCENTRATION," *IEEE Transactions on Electron Devices,* vol. 41, pp. 2357-2362, 1994.

[TakaVLSI03] Takagi S. Re-examination of subband structure engineering in ultra-short channel MOSFETs under ballistic carrier transport. VLSI Technol Dig 2003

[TomiNum] Kazutaka Tomizawa "Numerical Simulation of Submicron Semiconductor Devices" The Artech House Materials Science Library, 1993.

[TsucIEDM00] H. Tsuchiya, B. Fischer, and K. Hess, "A full-band Monte Carlo model for silicon nanoscale devices with a quantum mechanical correction of the potential," *International Electron Devices Meeting 2000, Technical Digest,* pp. 283-286, 2000.

[SteeTED07] J. van der Steen, D. Esseni, P. Palestri, L. Selmi, and R. J. E. Hueting, "Validity of the parabolic effective mass approximation in silicon and germanium n-MOSFETs with different crystal orientations," *IEEE Transactions on Electron Devices,* vol. 54, pp. 1843-1851, 2007.

[SzePhySC] S. M. Sze, "Physics of semiconductor devices", Wiley Interscience, second edition, 1981.

[WangIEDM02] J. Wang and M. Lundstrom, "Does source-to-drain tunneling limit the ultimate scaling of MOSFETs?," *International Electron Devices 2002 Meeting, Technical Digest,* pp. 707-710, 2002.

[WannTED96] C. H. Wann, K. Noda, T. Tanaka, M. Yoshida, and C. M. Hu, "A comparative study of advanced MOSFET concepts," *Ieee Transactions on Electron Devices,* vol. 43, pp. 1742-1753, 1996.

[WhanIEDM04] S. J. Whang, S. J. Lee, F. Gao, N. Wu, C. X. Zhu, J. S. Pan, L. J. Tang, and D. L. Kwong, "Germanium p- & n-MOSFETs fabricated with novel surface passivation (plasma-PH3 and thin AIN) and TaN/HfO2 Gate stack," *Ieee International Electron Devices Meeting 2004, Technical Digest,* pp. 307-310, 2004.

[WinsTED03] B. Winstead and U. Ravaioli, "A quantum correction based on Schrödinger equation applied to Monte Carlo device simulation," *IEEE Transactions on Electron Devices,* vol. 50, pp. 440-446, 2003.

[WuEDL07] N. Wu, Q. C. Zhang, D. S. H. Chan, N. Balasubramanian, and C. X. Zhu, "Gate-first germanium nMOSFET with CVD HfO2 gate dielectric and silicon surface passivation," *Ieee Electron Device Letters,* vol. 27, pp. 479-481, 2006.

[XuanEDL07] Y. Xuan, Y. Q. Wu, H. C. Lin, T. Shen, and P. D. Ye, "Submicrometer inversion-type enhancement-mode InGaAs MOSFET with atomic-layer-deposited Al2O3 as gate dielectric," *Ieee Electron Device Letters,* vol. 28, pp. 935-938, 2007.

[WuanEDL08] Y. Xuan, Y. Q. Wu, and P. D. Ye, "High-performance inversion-type enhancement-mode InGaAs MOSFET with maximum drain current exceeding 1 A/mm," *Ieee Electron Device Letters,* vol. 29, pp. 294-296, 2008.

[YeEDL03] P. D. Ye, G. D. Wilk, J. Kwo, B. Yang, H. J. L. Gossmann, M. Frei, S. N. G. Chu, J. P. Mannaerts, M. Sergent, M. Hong, K. K. Ng, and J. Bude, "GaAs MOSFET with oxide gate dielectric grown by atomic layer deposition," *Ieee Electron Device Letters,* vol. 24, pp. 209-211, 2003.

[YeoEDL05] C. C. Yeo, B. J. Cho, E. Gao, S. J. Lee, A. H. Lee, C. Y. Yu, C. W. Liu, L. J. Tang, and T. W. Lee, "Electron mobility enhancement using ultrathin pure Ge on Si substrate," *Ieee Electron Device Letters,* vol. 26, pp. 761-763, 2005.

[YuEDL04] D. S. Yu, K. C. Chiang, C. F. Cheng, A. Chin, C. X. Zhu, and M. F. Li, "Fully silicided NiSi : Hf-LaAlO3/SG-GOI n-MOSFETs with high electron mobility," *Ieee Electron Device Letters,* vol. 25, pp. 559-561, 2004.

[YuEDL05] D. S. Yu, A. Chin, C. C. Liao, C. F. Lee, C. F. Cheng, M. F. Li, W. J. Yoo, and S. P. McAlister, "Three-dimensional metal gate-high-kappa-GOI CMOSFETs on 1-poly-6-metal 0.18-mu m Si devices," *Ieee Electron Device Letters,* vol. 26, pp. 118-120, 2005.

[YuEDL04_2] D. S. Yu, C. H. Huang, A. Chin, C. X. Zhu, M. F. Li, B. J. Cho, and D. L. Kwong, "Al2O3-Ge-On-insulator n- and p-MOSFETs with fully NiSi and NiGe dual gates," *Ieee Electron Device Letters,* vol. 25, pp. 138-140, 2004.

[YuEDL03] D. S. Yu, C. H. Wu, C. H. Huang, A. Chin, W. J. Chen, C. X. Zhu, M. F. Li, and D. L. Kwong, "Fully silicided NiSi and germanided NiGe dual gates on SiO2 n- and p-MOSFETs," *Ieee Electron Device Letters,* vol. 24, pp. 739-741, 2003.

[ZhanEDL06] Q. C. Zhang, J. D. Huang, N. Wu, G. X. Chen, M. H. Hong, L. K. Bera, and C. X. Zhu, "Drive-current enhancement in Ge n-channel MOSFET using laser annealing for source/drain activation," *Ieee Electron Device Letters,* vol. 27, pp. 728-730, 2006.

[ZhuIEDM06] Z. G. Zhu, T. Low, M. F. Li, W. J. Fan, P. Bai, D. L. Kwong, and G. Samudra, "Modeling study of InSb thin film for advanced III-V MOSFET applications," *2006 International Electron Devices Meeting, Vols 1 and 2,* pp. 559-562, 2006.

Appendix 1

Brief history of the microelectronic industry

Birth of the microelectronic industry[7]

It is considered that the beginning of the semiconductor era coincide with the invention of the transistor by John Bardeen, Walter Brattain and William Shockley in December 1947. This revolutionary invention, which gave them the Nobel price in 1956, has been obtained, on purpose, after nearly 10 years of intense and successful research on solid-state physics at the Bell Telephone Laboratory.

The idea of a solid-state amplifier, opposed to the bulky and unreliable vacuum tube, first appears in 1930 when Julius E. Lilienfeld, a polish physicist emigrated in US, patented the concept of later-called field effect transistor. However, no realization followed this patent. In the beginning of the 30s, Marvin Kelly, then head of the vacuum tube department in the Bell Labs, became convinced that vacuum tubes could be replaced by solid-state electronic devices thanks to the progress made in the understanding of solid state physics. He understood that handling properly quantum mechanical theory was the key point to enable the invention of such devices. As most of the engineers and researchers in Bell Labs were having trouble with the details of this new theory, he decided to hire PhDs with strong background in solid-state physic and quantum mechanics. In 1936, after the Great Depression and the end of the hiring freeze in Bell Labs, Kelly became research director at Bell and hired William Shockley to lead study on vacuum tubes.

In 1938, after a reorganization of the Bell's physical research department, Marvin Kelly created a very independent three-man group, including William Shockley, dedicated to "fundamental research work on solid-state" and aiming for the development of useful method and material for the telephone business. The men of this group had a great freedom to choose their research field, provided that it corresponds to the company interests. Shockley, influenced by the ideas of Kelly about solid-state amplifier, quickly began to collaborate with Walter Brattain, an experimentalist, who had worked for the past two years on copper-oxide rectifiers. During 1938 and 1939, Shockley and Brattain multiplied the attempts to build a semiconductor amplifier. Despite many failures, Shockley became also convinced that the conception of a semiconductor solid-state amplifier was possible.

After a four year break due to the war, in 1943, the project restarted when Shockley enlarge the team and hired John Bardeen to bring a new theoretical expertise in the area of quantum mechanic. The following years, Bardeen worked with Brattain to understand the influence of surface state. In the meantime, large progresses were obtained in the Bell Labs on the purification, the crystalline formation and the doping of semiconductors like Ge or Si.

In December 1947, following several successful experiments on the study of the surface state using gold contact on germanium to form diodes, Bardeen had the idea to add a third gold contact to check if it could modulate a signal. Brattain conceived this experiment, but it was not conclusive. The current from the third contact was simply flowing through the germanium slab without affecting the current of the other contact. After calculations, Bardeen figured out that the two contacts on top of the slab had to be extremely close, i.e below few tenths of micrometers (a distance exceeding the width of most gold wire).

[7] Information given in this subsection are taken from [CristalFire]

On the December 15, Brattain by passed this problem by slicing a gold film on a triangular polystyrene piece with a razor edge to separate two gold contacts within the conditions Bardeen found. He used a small spring to contact this triangular piece on a slab of germanium and obtained the well-known device shown on
Figure 1.1 a).

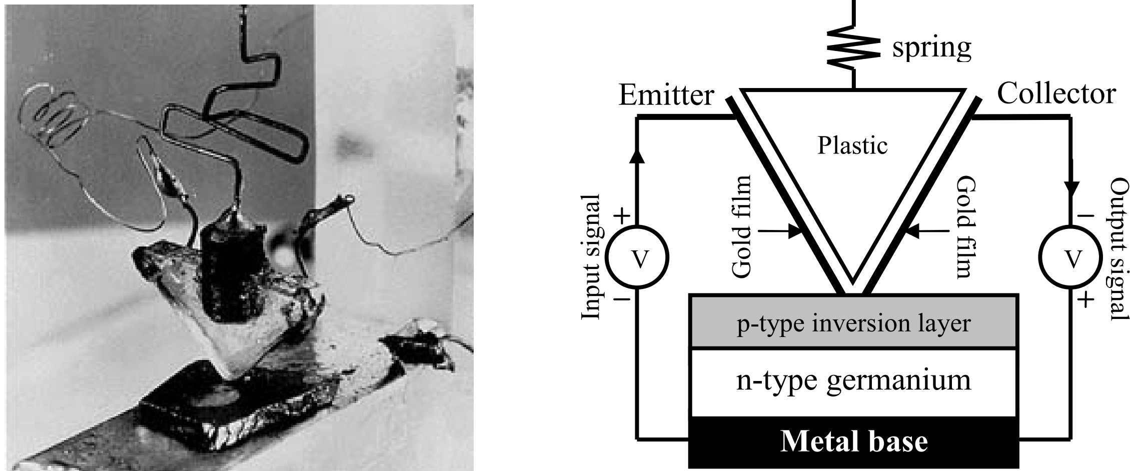

Figure 0.1 : a) Picture of the first point contact transistor fabricated at Bell Labs by Walter Brattain. b) Scheme of a point contact transistor

Brattain checked at first that the two gold contacts were both rectifying and then biased positively the first contact, later-called emitter, and negatively the second, later called collector. When he modulated the voltage on the emitter side, he observed the first solid-state amplification of a signal on the collector side. Indeed, when the collector is biased as shown in
Figure 1.1 b), it forms a diode, whose current can be significantly modulated by holes injected from the emitter.

On December 23, Bardeen and Brattain presented their results to the group, and few days afterward, to the Bell Labs executive. This breakthrough, expected by Marvin Kelly for many years was quickly patented and later presented to the public.

Shockley, who was not mentioned on the patent, used the results obtained from of the first point contact transistor to invent the bipolar transistor, clearly willing to have his own transistor patent (he preliminary tried to patent the field effect transistor, but the Lilienfeld one in 1930 avoid him to do so). The atmosphere in the group became tense. Bardeen and Brattain were put aside, mostly involved in the writing and protection of their own patent, while Shockley was strongly driving his group to work on his ideas. In summer 1951, Bardeen, who already started studying superconductivity, accepted a professorship position in the University of Illinois (he received a second Nobel price in 1972 for his theory of superconductivity).

Many further developments were made the following years. In particular, point contact transistors were replaced by the bipolar one, due to their better reliability, and silicon replaced germanium, due to better thermal properties. The activities concerning the transistor intensified in the Bell Labs and the industrial success soon became a reality when several companies started producing large amount of this devices.

Despite this success, Shockley also felt blocked in Bell Labs. The executive kept him in an expert position, while he was looking for a more important management role inside the lab. He finally managed to create his own company in 1956, with the help of Californian investors: the Shockley Semiconductor Laboratory. He formed his team recruiting among the best PhD in solid-state physic in North America and in Europe, including Gordon Moore, a 27 year old chemist from Cal Tech. However, Shockley did not succeed in producing any working transistors in two years. Instead, he insisted in developing his idea about N-P-N-P junctions. Finally, in September 1957, due to increasing management problems, the core of the team accepted a proposition from Fairchild Camera and Instrument, to create Fairchild Semiconductor.

Fairchild rapidly produced transistors and managed to win a hard battle against Texas Instrument for patenting the first integrated circuit in 1961. In the meantime, Bell Labs fabricated the first Metal-Oxide-Semiconductor Field Effect Transistor (MOSFET). These two winning strategies would enable the success of the semiconductor industry. In 1968, Gordon Moore and Robert Noyce left Fairchild to form Intel, which had overcome all other semiconductor companies in less than one decade.

The semiconductor industry was thus born thanks to the convergence of the clear vision of Marvin Kelly about technological challenges, the theoretical skills of Shockley and Bardeen and the experimental talent of Brattain. These multidisciplinary researches and the following technological progress enable a significant and fast growth of this industry.

Growth of the microelectronic industry

Increasing the ICs complexity

In 1965, Gordon Moore, then head of Fairchild Semiconductor, wrote a prophetic article [Moore65] about the future of integrated circuit in the fifth-anniversary edition of *Electronics* magazine. In this paper entitled "Cramming more components onto integrated circuits", he noted that the total number of component per integrated circuit had been doubling every year since 1962. Seeing no major limitation for this exponential increase in the forthcoming decade, he extrapolated his results and foreseen that in 1975, integrated circuits could contained 65000 transistors, as shown in Figure 0.2.

Thanks to this extrapolation, Moore predicted massive technological revolution, including the feasibility of personal computer, or "at least terminals connected to a central computer" [Moore65]. In a paper of the *Scientific American* about the electronic revolution which was a reality in 1977, Robert Noyce revisited Moore's article and showed that no significant deviation from the "Moore's law" had occurred.

This exponential increase of the integrated circuit complexity enabled a fast growth of the semiconductor industry. Most of the companies had exceptional growth rate around 15% per year during several decades.

As the growth of these company was, and is still, driven by the increased complexity of ICs, the increase of transistor density on a chip, i.e. their scaling, has quickly been identified as the key innovative point by the semiconductor industry. A consortium of American

semiconductor company, the Semiconductor Industry Association (SIA), regularly starts to meet to plan future trends of scaling.

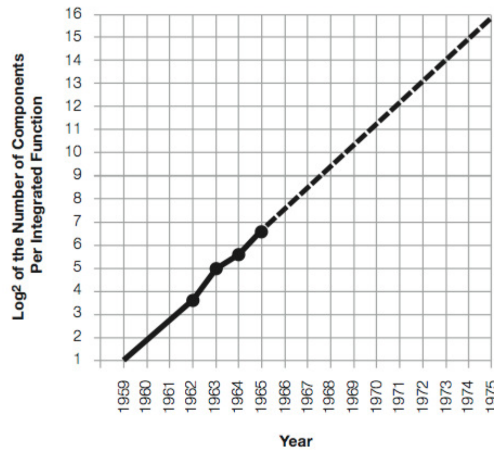

Figure 0.2 Original graph from [Moore65] of the log based 2 of the number of components per integrated circuit as a function of the year. The dots represents the data Moore had in 1965 and the dash line his extrapolation until 1975 ($2^{16} = 65536$).

Today, these meetings also include the European, the Japanese, the Korean and the Taiwanese equivalent of the SIA (respectively the European Semiconductor Industry Association (ESIA), the Japan Electronics and Information Technology Industries Association (JEITA), the Korean Semiconductor Industry Association (KSIA), the Taiwan Semiconductor Industry Association (TSIA)). Every two years, this enlarged consortium sponsors the publication of complete report of The International Technology Roadmap for Semiconductors (ITRS). Figure 0.3 presents a sum up of the ITRS specification between 1999 and 2005 regarding the on and off current specification of high performances CMOS technology [SkotTED2008]. The last edition of the ITRS report in 2007 [ITRS2007] published the description of the CMOS technology until 2022, i.e. the 11nm[8] technological node.

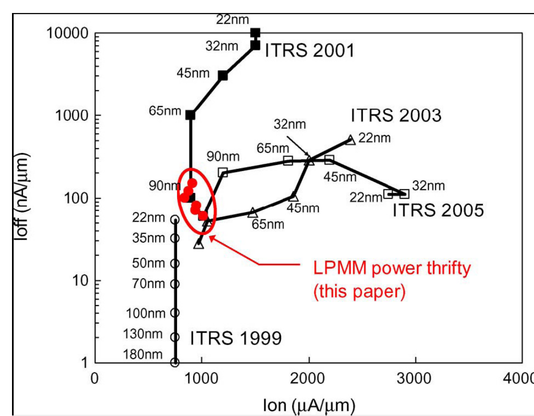

Figure 0.3 Off current vs On current specification of high performance MOSFETs according to the 1999, 2001, 2003 and 2005 ITRS reports. The red dots represent a roadmap for Low Power Mobile Multimedia Technology presented by Skonicki et al. in [SkotTED2008].

[8] Pitch between the source and drain metal contact.

Appendix 2

Literature review of the modelling of expected performance of alternative channel material

To our knowledge, the first theoretical investigation of the impact of alternative channel material in MOSFET has been proposed in 1991 by Fischetti and Laux [FiscTED91_1,FiscTED91_2], before the introduction of high-κ material has made possible to deposit reliable gate dielectric on alternative channel material. In a preliminary work [FiscTED91_1], using full band structure calculation for numerous semiconductors (Si, Ge, GaAs, InGaAs, InP), the author calibrated Monte Carlo simulations on measurements of the average carrier velocity vs. electric field in the crystalline state of these materials. From this procedure, they obtained a set of relevant parameters used to simulate with the Monte Carlo approach MOSFETs with gate length between 250 and 50nm [FiscTED91_2]. The results showed that, apart from In based material, the devices present performances. In addition, the authors emphasized the significant impact of the low density of states of these materials on the increase of quantum capacitance, which degrades the drivability of alternative channel material MOSFETs. Although this contribution is among the more detailed ones, the channel length considered are however too large to correspond to the present requirement of the ITRS and do not include tunneling leakage current.

In 2003, S. Takagi [TakaVLSI03] presented a paper comparing the performance of silicon and germanium devices in full ballistic transport regime. In this work, the author also introduce the problematic of best crystalline surface orientation for alternative channel material, as changing the channel material also requires to re-optimize the MOSFET channel orientation. Using the Natori full ballistic transport model in the quantum limit (one single fully degenerated subband), he showed that UTB Germanium On Insulator (GOI) MOSFETs on (111) surface has higher on current than bulk MOSFETs with channel in Si on (100) surface, or channel in Ge on (111) surface. Nevertheless, the authors only considered a single subband of parabolic L valleys of germanium, and did not treat systematically all possible channel orientation. In addition, no leakage mechanisms were considered.

Finally two contributions have been presented in the 2003 edition of the IEDM comparing silicon and germanium channel n-type Double Gate MOSFETs ballistic performances ([RahIEDM03] ,[LowIEDM03]). Both studies used the Non Equilibrium Green Function (NEGF – an efficient numeric technique to model ballistic transport accounting for all quantum effect) formalism and a generalized version of the NanoMOS software [NanoMOS] developed by Purdue University. It includes direct Source-to-Drain Tunneling (SDT) leakage mechanisms but neglect band-to-band tunneling and scattering. In both papers, band structures are treated in the effective mass approximation.

In [RahIEDM03], the results showed that Ge nDGFETs on (100) surface have better output performances than Ge devices on (111), due to lower density of states and larger Source-to-Drain Tunneling in Ge (111). Ge (100) devices were also found to outperform the Si (100). A study on the off condition demonstrated that SDT is highly sensitive to the gate length and the semiconductor film thickness. However, in this work, germanium have been simulated only considering the L valleys, neglecting the Δ ones (see subsection XXX) and the Ge (110) surface have not been studied.

Ge devices is more systematic in [LowIEDM03]. In addition to SDT and SCE naturally included in the NEGF formalism, Band-to-Band Tunneling (BBT) have been also added to

the source-drain leakages. Any possible channel orientation on the (100), (110) and (111) Ge surfaces has been also considered. Taking into account the Δ valleys as well as the L ones, the results obtained differ from [RahIEDM03]. This work has shown that, thanks to better relative occupancy of the L valleys over the Δ ones, the Ge device on a (110) surface have better performances than the Ge (111), Ge (100) and Si(100) one. The (111) poor performances have been attributed to high BBT leakage current and low quantum capacitance resulting from the low density of sate (DOS) which reduce the output current. For the (100) Ge device, the decreased current resulted to the larger filling of Δ the valleys which features larger effective mass (lower injection velocity). In addition, the current on the (110) substrate, although giving the best current, was found to be anisotropic, with a best channel orientation aligned in the [110] crystalline direction. This work has shown the significant role of higher satellite valleys in the alternative channel material simulation, and the importance of the introduction of source-drain leakage mechanisms as SDT and BBT. Still, only germanium has been considered in this work and not other III-V material, in relatively long channel (above 20nm), where the tunneling leakage current are not predominant (especially SDT). In addition, the used effective masses are questionable, the BBT models have been not detailed, and no clear explanation of the current anisotropy on (110) surface has been given.

Using the Natori model and considering all satellite valleys of Ge in the effective mass approximation, A. Pethe et al. [PetheSISPAD04] has re-obtained most of the results presented in [LowIEDM03], in particular the superiority of the germanium (110) surface over the other surfaces. It has also demonstrated that results obtained using the semi-analytic Natori model were in qualitative good agreement with numerical NEFG results.

S.E. Laux re-investigated the work done in [LowIEDM03], in the 2004 edition of the IEDM [LauxIEDM04] focusing on the crystalline orientation optimization. Using QDAME software (a full quantum ballistic tool), which account for quantum effects and SDT, and using the intrinsic switching time as a metric, all possible channel orientation were simulated for Si and Ge channel, with no restriction to the conventional (100), (110) or (111) crystalline wafer surface. Ge DGFETs with channel oriented in the [110] direction under a (-4 4 21) surface gave the best performances. This work gives in addition a better explanation of the current anisotropy on the (110) surface obtained in [LowIEDM03], which involve the selective feeling of L valleys whose best injection are in the [110] direction. Nevertheless, no comparison with other III-V material was made in this paper and the BBT contribution to the off current was not accounted.

In 2004, A. Rahman et al. [RahIEDM04] focused on the impact of the bandstructure modification due to quantum confinement in germanium DGFETs. Comparing the effective mass approximation with bulk masses and a full band approach using tight-binding calculation of the bandstructure, the authors demonstrated that the bulk effective mass can lead to major overestimation of the ballistic current for extremely thin film (below 4nm).

The following year, at the 2005 edition of IEDM [RahIEDM05], the same team used the same full band approach to compare Si(100), Ge(100), GaAs(100) and InAs(100) DGFETs. Depending on the equivalent oxide thickness (EOT), Ge or III-V devices have been found to outperform Si one. It also confirmed what has been obtained in [FiscTED91_2], i.e. the strong current degradation for low DOS material like III-V. This work also has highlighted the injection velocity degradation in alternative channel material due to the progressive filling of valleys with larger DOS, which could cause severe current degradation. Even thought short devices have been studied in this work (corresponding to the 32nm node of the ITRS), no

tunneling leakages current have been considered and no device orientation optimization has been carried out.

The Stanford group also published a contribution at this IEDM [PetheIEDM05], using the same approach as in [PetheSISPAD04], but considering GaAs(100), InAs(100) and InSb(100) devices in addition to Si(100) and Ge(110) devices and including Short Channel Effects (SCE) and BBT leakages. The authors showed that InAs and InSb devices exhibit strong BBT current and significant SCE, thus decreasing their performances. In addition, this paper showed that, in the effective mass approximation, due to quantum confinement and to the very small effective mass of the Γ valleys (first gap), a significant part of the inversion charge of InAs and InSb devices was also present in the L valleys (second gap), which lower the injection velocity (low DOS). Si and Ge based devices featured also quite large off current and poor on current due from the feeling of low injection velocity valleys (low DOS valleys). Finally, GaAs device showed better off and on state characteristics. Despite the numerous channel material and effects taken into account, this work only considered 15nm gate lengths, neglecting the impact of SDT leakages and the possible channel orientation optimization of III-V base devices.

In 2007, M. De Michielis et al [DeMiTED2007] investigated the performances of Si(100) and (110), Ge(110) and GaAs(100) DGFETs, using a single subband derivation of the Natori model. Using this model, the authors explained the current anisotropy of the drain current found on Ge and Si devices on (110) surface [LowIEDM03,LauxEDL05], and justified the respective best channel direction. In this work, Ge(110) devices showed larger ballistic current than its Si and GaAs counterparts. The detrimental impact of the small valleys masses (low DOS and hence high quantum capacitance) on the drain current has also been underlined. However, no leakages currents have been considered in this study.

16 year after the publication of [FiscTED91_1,FiscTED91_2], in 2007, M.V. Fischetti and S.E. Laux re-visited their work, accounting this time for SDT and BBT that have been found to be predominant in ultra short channel. In [FiscTED2007], the authors present several transport issue, including the simulation of Band-to-Band Tunneling. These aspects have then been exploited in [LauxTED2007] to simulate 22 and 17nm gate length UTB devices with Si, Ge, GaAs, InGaAs and InP. This work also included the impact of scattering in quasi-ballistic transport in these alternative channel materials. Using the intrinsic and extrinsic switching time as a metric, the author shows that InGaAs devices has shown the best performance, and also the weaker backscattering coefficient. This very detailed paper considered all significant leakage mechanisms, and more importantly, the effect of scatterings was rigorously treated thanks to the Monte Carlo approach. However, the device gate lengths studied were to long compared to the supposed length of future alternative channel material devices (22 an 17nm compared to the 4.5nm proposed as last technological node in the 2007 ITRS).

In the 2007 edition of the IEDM, Cantley et al [CanIEDM2007] studied the performances of Si, Ge and GaAs devices, using the NEGF formalism and NanoMOS. The bandstructure is treated in the effective mass approximation, but the effective mass have been extracted for ultra thin film thanks to tight binding simulations, which reproduce quite well the full band approach. The devices are scaled according to the last node specified in the ITRS, featuring gate length of 4.5nm. At this scale, SDT contribution, included in the NEGF formalism, are extremely strong, particularly in small effective mass material like Ge or GaAs. This work showed that for ultra scaled devices, Si channel could give better performances than Ge or

GaAs ones. However, BBT was not included, which could be of course also detrimental for these devices.

RESUME

La réduction des dimensions des transistors MOS, brique de base des circuits intégrés, ne permet plus d'augmenter efficacement leurs performances. Une des solutions envisagées actuellement consiste à remplacer le silicium par d'autres semi-conducteurs à haute mobilité (Ge, III-V) comme matériau de canal.
A partir de modèles analytiques originaux, calibrés sur des simulations avancées (quantique, Monte Carlo), cette thèse démontre que, à des dimensions nanométriques, les performances attendues de ces nouvelles technologies sont en fait inférieures à celles des composants silicium conventionnels. En effet, les phénomènes quantiques (confinement, fuites tunnel) pénaliseraient davantage les dispositifs à matériaux de canal alternatifs.

ABSTRACT

MOSFET scaling, building block of integrated circuits, do not allow to improve significantly the device performance anymore. One presently studied solution consists in substituting silicon for high mobility semiconductors (Ge or III-Vs) as channel material.
Based on original analytical models, calibrated on advanced simulations (quantum, Monte Carlo), this thesis demonstrate that at nanometric scale, the performances expected from this new technologies are in fact lower than the one of conventional silicon devices. Quantum effects (confinement, tunnelling leakage) have been indeed found to be more penalizing in the case of alternative channel material transistors.

SPECIALITE : Micro et Nano électronique

MOTS CLES

Transistor MOS, matériaux de canal alternatifs, modélisation analytique, méthode Monte Carlo, transport balistique, courant tunnel de la source au drain, courant tunnel bande à bande, nanoélectronique.